

Intermolecular Electronic Decay in Aqueous Solutions:  
A Liquid-Phase Photoelectron Spectroscopy Study

VON

MARVIN NICOLAS POHL

IM FACHBEREICH PHYSIK DER FREIEN UNIVERSITÄT BERLIN  
EINGEREICHTE DISSERTATION

BERLIN, 2018



Erstgutachter: PROF. DR. GERARD J. M. MEIJER

Zweitgutachter: PRIV.-DOZ. DR. UWE HERGENHAHN

Tag der Disputation: 21.11.2018



## ABSTRACT

This thesis reports on ground state and excited state electronic-structure studies from water and aqueous salt solutions by means of liquid-jet soft-X-ray photoemission (PE) spectroscopy. Novel PE spectroscopy methods and detection schemes are utilized in order to investigate changes in electronic structure, ion-solvation and nuclear dynamics upon soft-X-ray irradiation.

The first part of the thesis addresses the influence of atomic ions on the electronic structure of water. Hydrated ions have a profound effect on the geometric structure of liquid water and changes in the electronic structure are intuitively expected. However, using direct photoelectron spectroscopy, it will be shown that even very high salt concentrations have a negligible effect on the liquid water electronic structure. An almost unchanged PE spectrum is observed when going from neat water to 8 molar NaI concentration, which is argued here to be a result of the highly efficient screening of the ionic charges by the polarizable water molecules.

Besides the direct photoelectron experiments, novel spectroscopy methods are presented, exploiting non-local autoionization processes upon core-ionization. These electronic decay pathways involve energy- and electron transfer between neighboring molecules. Two types of non-local decay mechanisms are presented, intermolecular Coulombic decay (ICD) and electron-transfer mediated decay (ETMD), which are shown to be general phenomena in weakly interacting systems, such as hydrogen-bonded networks. The characteristics of these two decay channels can be used to infer information about solvation structure and dynamical processes in aqueous solution upon core-level ionization.

In particular, I report on proton nuclear dynamics triggered by soft-X-ray irradiation of the aqueous ammonium cation,  $\text{NH}_4^+$  (aq). The probability for ICD between N 1s ionized ammonium and surrounding water molecules scales with hydrogen-bond strength. PE spectral changes when comparing normal ammonium and its deuterated form,  $\text{ND}_4^+$  (aq), are related to altering nuclear dynamics along the N–H/D coordinate. Most notably, it is observed that a complete proton transfer between ammonium and a coordinated water molecule proceeds within the ultra-short lifetime of the N 1s vacancy ( $\sim 7$  fs). This complete chemical reaction is even accompanied by a second, although incomplete proton transfer to a second water molecule.

Very highly concentrated aqueous solutions have usually a high abundance of associated ion pairs, which possibly enables non-local autoionization pathways solely involving ions while neglecting the solvent water. I show that ETMD spectroscopy is very sensitive to local molecular arrangement due to its extreme short-range dependence. It is possible to directly extract ion-pairing character – be it separated, solvent-shared or contact pairing – from ETMD spectral analysis. However, experimental detection of low-energy ETMD electrons is very challenging when using standard PE spectroscopy. For the first time, the electron–electron coincidence detection scheme was applied to a liquid jet. This allowed to record Li 1s ETMD spectra from lithium aqueous solution,  $\text{Li}^+$  (aq), with enhanced collection efficiency compared to conventional detection schemes. ETMD spectroscopy’s unique ion-pair sensitivity is proven by changes in the PE spectral shapes corresponding to ETMD when comparing  $\text{LiCl}$  *versus*  $\text{LiCOOCH}_3$ .



## ZUSAMMENFASSUNG

Die vorliegende Dissertation behandelt die Untersuchung von Dynamiken der elektronischen Struktur von flüssigem Wasser und wässrigen Lösungen mittels Röntgen-Photoelektronen-(PE)-Spektroskopie unter Zuhilfenahme eines Flüssigkeitsstrahls. Neuartige PE-Detektiermethoden werden genutzt, um Änderungen von elektronischer Struktur, Ionensolvatisierung und nuklearer Dynamiken, die in Flüssigkeiten aufgrund von Röntgenbestrahlung auftreten, zu beobachten.

Im ersten Teil dieser Arbeit beschäftige ich mich mit dem Einflusses von Ionen auf die elektronische Struktur von Wasser. Hydratisierte Ionen beeinflussen die geometrische Anordnung von Wassermolekülen beachtlich und Änderungen der elektronischen Struktur von Wasser sind somit intuitiv erwartbar. Mit Hilfe direkter Photoelektronen-Spektroskopie wird gezeigt, dass bei Zugabe sehr hoher Salzkonzentrationen nur einen vernachlässigbarer Effekt auf die elektronische Struktur von Wasser eintritt. Die Beobachtung eines nahezu unveränderten PE-Spektrums bei einer Konzentrationsänderungen des Salzgehaltes von 0 molar zu 8 molar NaI ist ein Hinweis auf die außerordentlich effizienten Schirmungseigenschaften polarisierbarer Wassermoleküle.

Neben direkten Photoelektronen-Experimenten werden auch neuartige Methoden der PE-Spektroskopie vorgestellt, welche nicht-lokale Autoionisations-Prozesse ausnutzen, die nach Kernniveau-Ionisation auftreten. Diese elektronischen Zerfallskanäle beziehen Energie- und Elektronentransfer-Mechanismen zwischen benachbarten Molekülen mit ein. Im speziellen werden zwei Arten nicht-lokaler Zerfallsmechanismen vorgestellt: Intermolekularer Coulomb-Zerfall (ICD) und elektronentransfer-vermittelter Zerfall (ETMD), welche beide generelle Phänomene in schwachgebundenen Systemen, beispielsweise wasserstoffbrücken-gebundenen Molekülen, darstellen. Es wird gezeigt, dass die Charakteristika dieser zwei Zerfallskanäle genutzt werden können, um Informationen über die Solvationsstruktur und dynamische Prozesse herauszufinden, welche in wässrigen Lösungen nach Kernniveau-Ionisation auftreten.

Konkret präsentiere ich Nachweise für Protonendynamiken zwischen Ammoniumkationen und umgebenem Wasser, welche nach Bestrahlung mit Röntgenlicht auftreten. Die Wahrscheinlichkeit von ICD zwischen N 1s ionisiertem Ammonium und umgebenen Wassermolekülen skaliert mit der Stärke der vorhandenen Wasserstoffbrückenbindung. Es wird gezeigt, dass Unterschiede im PE-Spektrum zwischen normalem Ammonium und dessen deuteriertem Analogon auf veränderte nukleare Dynamiken entlang der N-H/D Bindungsachse zurückzuführen sind. Es wird demonstriert, dass sich ein vollständiger Protonentransfer zwischen Ammonium und einem umgebenen Wassermolekül innerhalb der extrem kurzen Lebensdauer des N 1s Loches abspielt ( $\sim 7$  fs). Diese ultraschnelle chemische Reaktion wird sogar noch von einem zweiten, wenn auch unvollständigen, Protonentransfer begleitet.

Sind Ionenpaare in wässriger Lösung vorhanden, so werden nicht-lokale Zerfallsprozesse ermöglicht, die ausschließlich zwischen den Ionen stattfinden. Ich werde zeigen wie ETMD als empfindliches Instrument zur Bestimmung lokaler Molekülanordnung genutzt werden kann und dass die Art der Ionenpaarung – sei es getrennt, Lösemittel-geteilt, oder in Kontakt – aus den entsprechenden ETMD-Spektren abgeleitet werden kann. Da es mit Hilfe konventioneller PE-Spektroskopie-Methoden schwierig ist, Elektronen geringer kinetischer Energie zu messen, werde ich die Anwendung der Elektron-Elektron-Koinzidenzmethode auf den Flüssigkeitsstrahl präsentieren. Dies ermöglicht Li 1s ETMD-Spektren von Lithiumkationen in wässriger Lösung mit erhöhter Detektiereffizienz zu messen. Die Empfindlichkeit von ETMD für Ionenpaarung wird anhand eines Vergleiches zwischen LiCl und LiCOOCH<sub>3</sub> nachgewiesen.





# List of Abbreviations

as	Attoseconds
aq	Aqueous phase
BE	Binding energy
CCD	Charge-coupled device
DI	Double ionization
DNA	Deoxyribonucleic acid
eV	Electronvolts
EMFP	Elastic mean free path
ETMD	Electron-transfer mediated decay
ESCA	Electron spectroscopy for chemical analysis
FRET	Förster resonant energy transfer
fs	Femtoseconds
HPLC	High-performance liquid chromatography
ICD	Interatomic/intermolecular Coulombic decay
IE	Ionization energy
IMFP	Inelastic mean free path
KE	Kinetic energy
M	Mol per liter
MCP	Micro-channel plate
MD	Molecular dynamics
PE	Photoemission
PES	Potential energy surface
ps	Picoseconds
PTM-CS	Proton-transfer mediated charge-separation
ROI	Region of interest
RPE	Resonant photoemission
TOF	Time-of-flight
UC	Universal curve
XUV	Extreme ultraviolet
XPS	X-ray photoemission spectroscopy



# Contents

0	Preface	1
1	Introduction	7
2	Photoemission Spectroscopy	11
2.1	Photoionization . . . . .	13
2.2	Autoionization . . . . .	15
2.2.1	Auger Decay . . . . .	16
2.2.2	Resonant Photoemission . . . . .	18
2.2.3	Intermolecular Coulombic Decay . . . . .	20
2.2.4	Electron-Transfer Mediated Decay . . . . .	23
2.3	Spectral Intensities . . . . .	25
3	Experimental Methods	29
3.1	Light Sources . . . . .	30
3.1.1	Synchrotron Radiation . . . . .	31
3.1.2	Undulator Device . . . . .	33
3.2	The Liquid Microjet . . . . .	34
3.3	SOL <sup>3</sup> . . . . .	37
3.4	Magnetic-Bottle Time-of-Flight Spectrometer . . . . .	40
3.5	Electron–Electron Coincidence . . . . .	43
4	Photoemission from Liquid Water	47
4.1	Water in the Presence of Salt . . . . .	50
4.2	NaI in Aqueous Solution: From Low to High Concentrations . . . . .	52
4.3	Dielectric Screening of Liquid Water . . . . .	61
4.4	Weakened Intermolecular Interactions . . . . .	68

5	Autoionization from Aqueous Systems	71
5.1	Core-Level ICD in Aqueous Solutions . . . . .	72
5.2	Proton Transfer in Water . . . . .	73
5.3	Proton Transfer in Other Aqueous Systems . . . . .	81
5.4	Proton Dynamics in Aqueous Ammonium . . . . .	83
6	ETMD in Aqueous Lithium Solutions	91
6.1	ETMD as a Probe for Local Solvation . . . . .	93
6.2	Experimental Evidence of ETMD . . . . .	97
6.3	Ion-Pairing: LiCl Versus LiOAc . . . . .	100
6.4	The Strong Hydration Shell of Aqueous Lithium . . . . .	105
7	Summary	109
8	Outlook	113
	Bibliography	119
	List of Publications	155
	Acknowledgments	157
	Curriculum Vitae	159
	Selbstständigkeitserklärung	161

# O

## Preface

Scientific advance always depends on societal and technical realities. However, the other way around, scientific needs catalyze societal and technical developments. In this simple formula lies everything I need to explain the immense importance of science for a modern society. Despite the common argument that the sheer act of acquiring knowledge about nature is a fundamental human behavior,<sup>1</sup> I believe this is not necessarily true. Of course, people strive for explanations of phenomena they do not understand, which is most easily observed for young children who lust for answers. However, this is not what scientific research is about. Recapturing the latter argument, most people are satisfied with whatever they get as an answer. They do not question or challenge an explanation as long as it is reasonable enough. Even more, given the person they ask for an answer is a well-known authority, people tend to believe even semi-reasonable ‘truths’, as shown in the famous Milgram experiment.<sup>2</sup> I believe in that regard people are much more a ‘social’ than a ‘scientific’ species. Scientists are different from that usual behaviour in a sense that they challenge not only well-established explanations, but also their own opinions.<sup>3</sup>

My personal answer to the question of why science is important is less romantic but more practical. I believe science is crucial for a modern society that relies on *trust* and sound decisions. In that regard we as scientists should always be aware that our work

relies deeply on the trust people give us and that we must continuously communicate the complex interplay between society and science.<sup>4</sup> For example, the medieval, a time in which science was considered a witchcraft, was dominated by social threats, plagues, wars and extreme poverty all over Europe.<sup>5-9</sup> On the other hand, the work of researchers can ‘by accident’ result in developments that revolutionize the communication of a whole planet as happened in the late nineties at CERN. When the physicist Tim Berners-Lee worked on a solution to simplify the communication between him and his colleagues, he finally created the hypertext markup language (HTML) and the hypertext transfer protocol (HTTP) which is the basis for what we know today as the ‘world wide web’.<sup>10,11</sup> Further positive examples of the interplay between science and society can be easily found when looking at the timeline of the Nobel prizes. For instance, Wilhelm Conrad Röntgen was the first person ever granted a Nobel prize in physics.<sup>12,13</sup> His remarkable discovery of high-energy radiation was enabled by at that time state-of-the-art gas discharge lamps.<sup>14</sup> Today we call this radiation ‘X-rays’. The impact of this discovery is wide-ranging, and X-rays were adapted very quickly in multiple fields. The modern medical diagnostic would not be possible without its imaging possibilities.<sup>15-18</sup> It also provides valuable applications in areas such as archeology and arts.<sup>19-22</sup> Our current understanding of matter on an atomic scale is largely acquired by means of X-ray spectroscopy.<sup>23,24</sup> Today, we are in the middle of a transition into a post-industrial century where many kinds of traditional work are about to be automatized.<sup>25,26</sup> As such our society as a whole evolves in a direction where knowledge will be fundamental part of our every-day lives. A big part of our job as scientists was always to differentiate facts from fakes and as such I cannot overstate the importance of science for our future society.

The present thesis tries to connect to these developments by using X-ray methods. The aim of my studies is to fundamentally understand basic mechanisms in radiation chemistry, e.g., processes that lead to biological radiation damage. I am particularly interested in intermolecular ultrafast energy transfer and charge migration processes that occur upon X-ray irradiation of aqueous solutions. I will present novel X-ray spectroscopy techniques, i.e., X-ray photoemission (PE) spectroscopy applied to liquid-phase water and aqueous solutions. With photoemission spectroscopy it is possible to map the measured kinetic energies (KE) of emitted electrons onto the electronic structure of

the system under observation.<sup>27</sup> Despite the requirement for high vacuum conditions in PE spectroscopy, the past decades engendered successful technological advances using micrometer-sized liquid jets providing the possibility to measure electron signal from liquid phase samples.<sup>28,29</sup> For almost 20 years the liquid jet was the only experimental technique to access volatile samples with PE spectroscopy. Only relatively recent, experimental approaches such as utilizing ambient-pressure electron analyzers, ultra-thin graphene membrane flow cells and the ‘dip-and-pull’ method, have become available.<sup>30–35</sup> Despite these new approaches, the liquid jet is still the most convenient technique due to its relatively simple applicability and for many scientific questions it is irreplaceable. The X-ray light characteristics are of particular importance for these types of experiments, calling for the continuous development of advanced light sources. All results presented in this thesis are measured at the synchrotron facility BESSY II at the Helmholtz-Zentrum Berlin (HZB), Germany.

This thesis presents an extract of the findings I made during my 3-year PhD work at the HZB and the Fritz-Haber-Institut of the Max Planck Society. It is structured into eight chapters. First, I introduce the general topic, motivate my work and present the theoretical background (Chapters 1–2). In Chapter 3 I give an overview of the techniques and experimental approaches that I used. I also describe the ‘SOL<sup>3</sup>’ liquid-jet photoelectron setup I used to acquire most of the data in this thesis, and which I planned and built from scratch during my PhD time together with Robert Seidel and Bernd Winter. In the results section I first address the influence of hydrated ions on the water electronic structure (Chapter 4). Solvent water is often considered a passive medium in which chemistry takes place, while neglecting the influence of a solute on the overall bulk water structure. This assumption may be intuitive for highly dilute aqueous samples but is questionable for high salt concentrations. I show that even for very highly concentrated 8 M NaI solutions the water electronic structure barely changes. The most important finding of this aspect of my work is that the lowest ionization energy of water, which is community-wide used as an energy reference, remains constant as well. In the next part of my thesis I present my studies on intermolecular electron and energy transfer processes upon X-ray ionization (Chapters 5–6). Chapter 5 addresses intermolecular Coulombic decay (ICD) which is a certain type of electronic decay that involves energy transfer between neighbor-

ing molecules. ICD rates strongly compete with its local analog the Auger decay.<sup>36</sup> It will be shown that the probability of ICD increases with hydrogen-bond strength and that a comparison between ICD signal from a molecule in its normal and deuterated form can be exploited to gain information about nuclear dynamics on an ultrafast timescale. In the last part of the results (Chapter 6), I will focus on electron-transfer mediated decay (ETMD). I will introduce my choice of the benchmark system  $\text{Li}^+$  in aqueous phase to probe ETMD without competition from other decay channels. Electrons ejected due to ETMD in lithium are relatively slow compared to electron emission from other decay channels. Slow electrons are challenging to measure by means of standard photoelectron spectroscopy, due to large background signal. I apply a novel, highly sensitive detection scheme in order to detect ETMD electrons and discriminate them from background electrons, thus achieving a large signal-to-noise ratio. Further on, I demonstrate the sensitivity of ETMD to local atomic environment (first hydration shell) and I show this method to be a powerful tool to detect ion pairing in electrolyte solutions. My thesis is closed by a summary (Chapter 7), and an outlook (Chapter 8).

In writing my thesis I was very careful to make sure that results are introduced in an understandable fashion. Therefore, my personal accomplishments are not ‘hard-cut’ from the fundamental results of my predecessors and it might be sometimes difficult to differentiate for the reader. The results are presented in Chapters 4–6. My own work focussed predominantly on experimental studies and theoretical findings in this thesis are mostly acquired by the group of Petr Slavíček. Chapter 4, presenting studies on aqueous NaI entirely covers work I did (the experimental parts). In Chapter 5 the experimental results on aqueous ammonium present work I did, while all results on pure water, ammonia and hydrogen peroxide review former work, yet they are necessary here to introduce and motivate the ammonium experiments. In Chapter 6 all experimental results of lithium chloride measured with the magnetic-bottle setup are done by me. I also contributed to the work measured with a hemispherical analyzer, however these results are already published in greater detail in a former thesis.<sup>37</sup>

The present work compiles the current status of ongoing research on ICD and ETMD in liquid phase. As such it is part of the Deutsche Forschungsgemeinschaft (DFG) Research Unit FOR 1789 on ‘Interatomic and Intermolecular Coulombic Decay’, which



is a collaborative cluster of scientists that aims to demonstrate the importance of ICD and ETMD in a broader context, bridging the gap between fundamental research on the correlated motion of electrons and nuclei, and applied research, e.g., on the role of low-energy electrons in radiation chemistry.



# 1

## Introduction

Water is by far the most important molecule for life on earth. In fact, it is considered the main prerequisite for life to appear on a planet.<sup>38</sup> At first glance, water – H<sub>2</sub>O – is a relatively simple three-atomic molecule.<sup>39</sup> However, the understanding of the intermolecular interactions between water molecules in the condensed phase is still incomplete. Until today over 70 anomalies at which water properties are different from those of other liquids, such as the density anomaly at 4 °C, have been identified.<sup>38-41</sup> Another example is that despite its small molecular weight, which is comparable to gaseous compounds like N<sub>2</sub>, CO<sub>2</sub>, SO<sub>2</sub> and H<sub>2</sub>S, water stays liquid under standard atmospheric conditions.<sup>42</sup> This is caused by the propensity of water molecules to form a tight network via hydrogen bonds, which raises the boiling point to 100 °C. Liquid water is the result of flexible hydrogen bonds which undergo quick structural rearrangements. It takes only picoseconds for a water molecule to break its hydrogen bond and reach out for a new partner to form a bond.<sup>43</sup> When put into water, many organic molecules form also hydrogen bonds with water, making it an ideal biological environment and furthermore enabling the organization of biopolymers in three-dimensional structures.<sup>44,45</sup> Indeed, water is the main medium accommodating biomolecules; e.g., the human body consists of approximately 60% water.<sup>46</sup> The transient hydrogen bonds can drive dynamic exchange pro-

cesses of charge or energy which is why water can also act as a reactant in many biochemical reaction pathways. Its large total molecular dipole moment of 2.95 Debye<sup>47,48</sup> (only 1.85 Debye for an isolated water molecule) supports the dissociation of polarizable organic groups such as NH<sub>2</sub>, OH and COOH, thus enabling further reactions.

Water is omnipresent in biological tissue, and as such its active role in biomolecular damage due to high-energy irradiation should not be underestimated.<sup>49</sup> As an example, it has been found that radiation damage of DNA strands by high-energy photons is not only caused by direct exposure, but also, to an even higher extent, mediated by the products formed upon irradiation of water.<sup>50,51</sup> Two main mechanisms are described in the literature. For the direct process, energy deposition by high-energy photons creates electron holes in the DNA, which then migrate to specific sites where subsequent reactions form ionic radicals and finally cause the risk of disease.<sup>52-55</sup> On the other hand, for the indirect process, photo-excited bulk water molecules dissociate into highly reactive radicals, e.g., ·OH and H<sup>+</sup>, or create slow electrons, which have been found to cause single and double strand breaks in DNA molecules.<sup>56,57</sup> Studies using low-energy electron irradiation on DNA-deposited surfaces have demonstrated that electrons with energies below the ionization threshold attach to the DNA, thus creating a transiently excited anionic species which subsequently decays via dissociation.<sup>58</sup> In complex systems, a third mechanism occurs in which energy is deposited in molecules bound to the DNA, including solvation water. The so called quasi-direct effect acts on the DNA base via hydrogen abstraction.<sup>59</sup>

Exploring the exact mechanisms driving the functional degeneration of biological compounds upon irradiation with high-energy light is necessary in order to anticipate consequences of radiation exposure and to design concepts for radiotherapy.<sup>60-62</sup> Intermolecular decay processes initiated by photoionization create large amounts of electrons with kinetic energies (KE) of 1–10 eV, an energy range which is known to effectively cause degradation of biomolecules.<sup>63</sup> For example, recent theoretical studies on hydrated metal ions revealed that, if sufficient energy is deposited into the system, intermolecular charge transfer processes combine into complex relaxation cascades.<sup>64</sup> The authors created an unstable trication by removing a core electron from micro-solvated Mg<sup>2+</sup>. They showed that the trication decays via a multitude of non-radiative channels while returning to bi-

valence after all. These cascades have been found to be a source of highly reactive radicals and slow electrons. Absorption of an X-ray photon by a metal ion predominantly releases a core electron, which in turn creates a positively charged species in an excited state. Typically, this state decays via emission of a second-order electron, which accumulates a further positive charge, either at the originally ionized atom, or at water molecules in the hydration shell. The doubly-ionized residual is very likely to undergo further chemical reactions, which, as a consequence, causes decomposing of biomolecules in the vicinity of X-ray exposure.<sup>65</sup>

The present work is motivated by the study of energy and charge transfer processes occurring in aqueous solution immediately after irradiation with X-ray light. I aim to understand the underlying decay mechanisms as well as their impact on charge delocalization. On the molecular level, charge and energy transfer processes in atoms or molecules can only be understood in combination with profound knowledge about the system's electronic structure, which is most directly accessed by photoemission spectroscopy.<sup>27,66</sup>



# 2

## Photoemission Spectroscopy

Photoemission spectroscopy\* is an experimental technique to access the electronic structure of atoms and molecules.<sup>27,29</sup> PE spectroscopy, as well as every other X-ray based spectroscopic technique, is an element specific technique, providing the ability to probe a defined atom at a defined orbital, while being sensitive to the chemical environment.<sup>68</sup> During the last decades electron-detection schemes proved to be particularly suitable for electronic structure analysis. As compared to other observables (e.g., measuring photons, atoms or ions) electrons offer a unique combination of several practical aspects, such as: surface sensitivity, easy tunability in energy and space by electric fields, easy countability and the fact that electrons disappear after they have been detected.<sup>27</sup> Also, photoemission is always symmetry allowed, whereas photon-absorption based detection is subject to more stringent selection rules.<sup>69</sup> The promotion of an initially bound electron into a higher energy state is always the starting point for PE spectroscopy and is usually (but not only) realized by either electron impact or high-energy irradiation. Nowadays, the latter is most common due to the development of tunable and high-intensity light sources.

---

\*The term photoemission might be confusing as it describes the detection of emitted electrons rather than photons.<sup>67</sup> However, photoemission spectroscopy is not synonymous with photoelectron spectroscopy. Photoemission is a generic term including photoelectron as well as second-order electron emission processes.

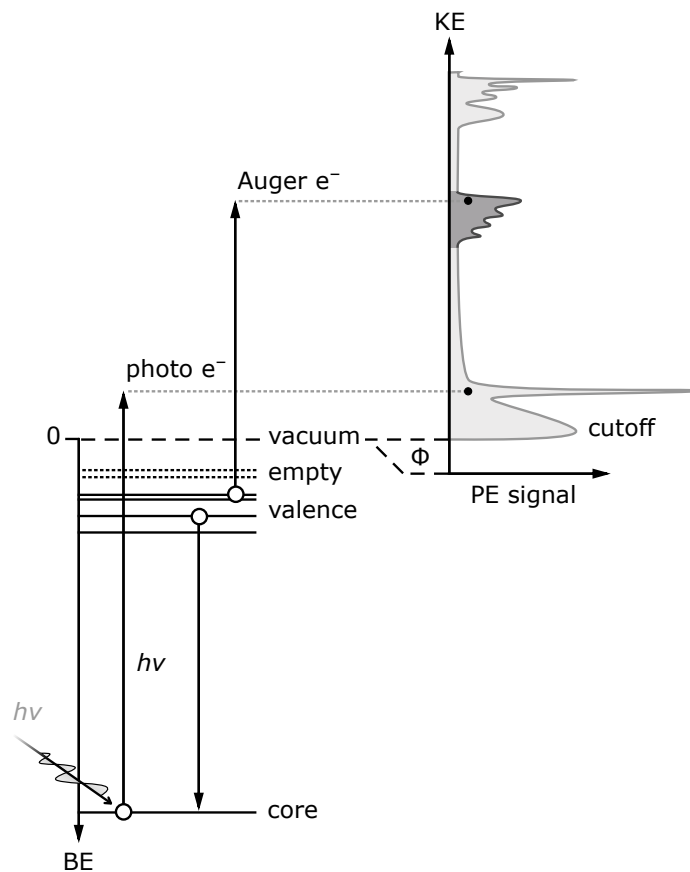


**Figure 2.1:** Diagram of the energy levels involved in a photoemission experiment. A (photo-) electron can be detached from the system (ionization) if the initial photon energy  $h\nu$  is high enough to exceed a given core or valence orbital binding energy (BE). The BEs are referred to the vacuum level beyond which the ejected electrons are free. The kinetic energies (KE) of all ejected electrons give rise to the PE spectrum. Inelastically scattered electrons contribute to the increased background signal at low KEs. The cutoff at which the electrons KEs are too small to exceed the ionization threshold (also referred to as work function  $\Phi$  for solid materials) depends on the system and also on the experimental conditions. After ionization, the remaining electron vacancy can recombine with a valence electron while ejecting another valence electron (Auger electron). The kinetic energy of the Auger electron depends on the energies of the orbitals involved, rather than the photon energy. After Auger decay the system remains in a two-hole state. Unfilled circles indicate electrons involved in the ionization/decay process.



Photoemission is a generic term referring to all kinds of electron ejection, independent of the particular mechanism. Dependent on whether the initially bound electron gets promoted into a continuum or a bound state, one refers to (photo-) ionization or resonant (photo-) excitation, respectively. After excitation (resonant or ionization) the system remains in a transient state which eventually decays. Different decay scenarios may occur upon excitation, which to a large extent depend on the initial photon energy. De-excitation pathways are classified into relaxation via photon emission (radiative) or second-order electron emission (non-radiative).<sup>70</sup> Note that non-radiative decay, also referred to as autoionization, usually occurs upon high-energy excitation. Low-energy inner-valence excitation often only heats up the system – by converting initial energy into vibrational energy – and does not initiate further autoionization.

In an experiment, the measured KEs of all liberated electrons give rise to the PE spectrum which can be directly related to the occupied orbitals in the target sample.<sup>27,66</sup> A prototypical PE spectrum is presented in Figure 2.1. The shown spectrum is artificially generated and not measured, however it serves well to demonstrate the key elements. It features valence band and core level peaks on top of a sloping background created by secondary inelastically scattered electrons with a sharp cutoff at zero KE. The next sections will explain all mentioned processes, i.e., photoionization, resonant photoexcitation and autoionization, in greater detail.

## 2.1 PHOTOIONIZATION

If sufficient initial photon energy is provided to exceed the sample-specific ionization threshold (commonly referred to as work function  $\Phi$  for solid materials, or ionization potential for free molecules) an initially bound (photo-) electron liberates. Note that sometimes the term ‘photodetachment’ is used, referring to electron ejection from an initially anionic system. Another common term is ‘direct PE’, as a contrast to second-order (indirect) autoionization. Photoionization is a direct measure of the occupied electronic structure, because the KE of the released electron is related to its initial orbital BE via the photoelectric law<sup>27,71</sup>

$$BE = h\nu - KE - \Phi \quad (2.1)$$

where the Planck constant  $h$  and the light frequency  $\nu$  determine the photon energy. Different chemical environments can alter a systems BEs considerably, leading to shifts in KE. This is one of the main reason why electron spectroscopy for chemical analysis (ESCA) has become a wide-spread technique.<sup>68,72–75</sup>

Photoionization is a photon-in–electron-out process. As such measured KEs reflect always a final state that is lacking one electron with respect to the initial ground state. On ultrafast timescales the orbital energies adapt to the missing electron, whereas on longer time scales the atoms and molecules surrounding the newly formed ion rearrange. In practice the situation can be more complex, and several approximations are often incorporated to interpret/understand the processes occurring.<sup>27</sup> The approximations relevant for a given process depend on both the molecule and the photon energy employed.

- First, the ‘independent-particle assumption’ excludes complex electron–electron interactions, assuming a photoelectron experiences an average electrostatic potential created by positive (nuclear) and negative (electronic) charges.<sup>76</sup> This assumption is reasonable for weakly interacting systems like hydrogen-bonded liquids.
- Removing charge from an initially ground-state system is also accompanied with changes in orbital energies. The ‘sudden approximation’ assumes that the passive orbitals, i.e., orbitals that keep their electrons, are the same in the final state as they were in the initial state.<sup>77,78</sup> This assumption is called ‘sudden’ since photoelectrons are fast enough to neglect the aforementioned changes in orbital energies. Under this assumption the binding energies measured in a PE experiment equal the ground-state orbital energies, known as Koopmans’ binding energies. For very low-KE photoelectrons, that linger in the proximity of the emission center, as well as second-order electrons that are born later in time the ‘sudden approximation’ is not fulfilled. As a rule of thumb, the ‘sudden approximation’ is justified for electron kinetic energies above tens of electronvolts (eV). In PE spectroscopy, typical photon energies range between extreme ultraviolet (XUV, 10-124 eV), soft-X-ray (124-12400 eV) and hard-X-ray (12.4-124 keV).<sup>79</sup> Extreme ultraviolet photoemission spectroscopy gives access to the valence band structure, whereas (soft-) X-ray photoemission spectroscopy (XPS) provides information on the localized core lev-

els and energetic shifts which relate to chemical bonding and many-electron effects.<sup>66</sup> Experiments reported in this thesis utilize photon energies within the soft-X-ray regime, ranging between 100 eV to 1600 eV.

- Finally, the ‘Born-Oppenheimer approximation’ assumes that the nuclear and electronic motion can be separated and that electrons will adapt to a given nuclear conformation as nuclear motion is very slow compared to electronic motion.<sup>80</sup> As photoionization occurs on much faster timescales (attoseconds (as)<sup>81,82</sup>) than any atomic movement (femtoseconds (fs)<sup>83,84</sup>), this approximation is relevant for molecules and strongly correlated systems. However, similar to the ‘sudden approximation’, the ‘Born-Oppenheimer approximation’ fails for low-KE electrons and electrons from second-order processes that take place on longer timescales and may entangle with nuclear motion, as will be detailed later in this thesis. The ‘Born-Oppenheimer approximation’ also fails when vibrational frequencies are comparable in energy to the energy difference between electronic states.

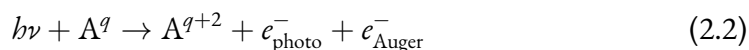
## 2.2 AUTOIONIZATION

Autoionization is a so-called second-order process that can follow photoionization or resonant photoexcitation upon X-ray irradiation. Both excitation mechanisms create an electron hole, leaving the system in an excited state, which will eventually relax via electronic decay. Different decay channels are possible, all of which result in different final states. Beside radiative decay, where the excess energy is released via emission of a photon (also referred to as fluorescence<sup>85</sup>), for non-radiative decay a second-order electron is being ejected (autoionization<sup>86,87</sup>). Thus, in general terms autoionization is characterized as a process in which a system ionizes itself autonomously, i.e., without further influence from outside. Note, that in this thesis autoionization is always referred to as self-ionization upon photoexcitation, while this term is used in a wider context in literature. For example, a randomly chosen, intact water molecule will dissociate (or autoionize) in liquid water without further influence, producing hydronium ( $\text{H}_3\text{O}^+$ ) and hydroxide ( $\text{OH}^-$ ) ions, within  $\sim 10$  hours.<sup>88</sup> In the simplest picture, a complete autoionization process involves three orbitals – the initially ionized/excited orbital, the electron donating

orbital and the electron emitting orbital. An atom or molecule that is neutral in its initial state ends up in a doubly charged final state following photoionization and subsequent autoionization. I will later show that different autoionization processes lead to altering locations of these two charges. I particularly differentiate between final states that have both charges localized at one site (2h) and those that have the two charges at separate sites (1h1h), on different molecules.

### 2.2.1 AUGER DECAY

The Auger decay – discovered by Lise Meitner<sup>89</sup> and named after Pierre Auger<sup>90</sup> – is an autoionization process in which all involved molecular orbitals are located on the same atom or molecule.<sup>91,92</sup> The final state is of 2h character. The Auger process for a given system, A, with initial charge  $q$  can be described as



Two free electrons are produced in the process. The KE of the photoelectron,  $e_{\text{photo}}$ , is determined by the initial photon energy, whereas the KE of the Auger electron,  $e_{\text{Auger}}$ , depends only on the orbitals involved, as shown in the energy diagram of Figure 2.1. For example, considering a core ionization followed by valence electron relaxation and valence electron ejection, the energy of an Auger electron can be estimated as

$$KE_{\text{Auger}} \approx BE_{\text{core}} - BE_{\text{valence 1}} - BE_{\text{valence 2}} \quad (2.3)$$

This is only a rough estimate and neglects contributions from screening and the Coulombic repulsion of the two resulting electron holes, but also nuclear rearrangement. Auger transitions are denoted according to the involved atomic shells, e.g., KLL for a K-shell vacancy and L-shell relaxation and emission. In the case of more complex systems as molecules, the orbital notation is often more appropriate, e.g., 1s-1b<sub>1</sub>1b<sub>1</sub> for oxygen 1s (K-shell) ionization and valence relaxation/ejection from the water 1b<sub>1</sub> valence orbital. If energetically feasible, each electron occupying a state above the core hole can serve as decay or emission partner. The combination of all possible Auger decay channels results in extended Auger spectral features in a PE experiment. Since the energy levels of an atom are

discrete, the resulting energy spectrum of the Auger electron is discrete and characteristic for each element. However, features are commonly overlapping, and disentanglement of individual transitions is experimentally rather complicated and only possible with computational support.

After a core vacancy is filled, a new vacancy in a higher-lying orbital is generated which will immediately be filled due to transitions from even higher orbitals and so on. This cascade continues until the system remains in a relaxed state. For high- $Z$  elements, a single vacancy in the K shell can result in hundreds of possible transitions; each transition results in the emission of X-rays or electrons. The case of electron emission (Auger decay) leads to continuous accumulation of positive charge and the electrostatic potential between the escape electron and the atomic core can reduce the electron emission yield.<sup>93</sup> Therefore, the Auger decay process is less probable for heavy atoms (higher than  $Z \approx 30$  for a K-shell vacancy), with X-ray emission being the dominant relaxation pathway.<sup>23</sup> However, for light elements Auger decay dominates by far (99%).<sup>94</sup> The lifetime of a core-ionized atom is on the fs timescale.<sup>95-97</sup> Accordingly, Auger decay is supposed to proceed within a narrow time window, while being sensitive to electronic or even nuclear dynamic processes happening in that time frame. In the ‘slow’ (but still ultrafast) fs time frame of the Auger process, the system may have already responded to the core vacancy. Photoionization proceeds on an ‘instantaneous’ as-timescale (i.e., 1000 times faster).<sup>81,82</sup> Both processes combined – ‘fast’ photoionization (start) and ‘slow’ Auger decay (end) – provide a time window which is exploited as so-called core-hole clock.<sup>98,99</sup> A typical O–H stretch frequency at  $\sim 3500 \text{ cm}^{-1}$  ( $\approx 10$  fs period of a full oscillation) falls into that time window.<sup>100</sup> The final Auger spectrum is, quite naturally, a composition of all Auger electrons emitted for individual decay channels while the dynamics of the core excited/ionized species evolve. The core-hole clock is therefore useful to provide an upper time limit for electronic and nuclear dynamics which can occur concurrently with core-hole relaxation.

Auger decay is typical for isolated gas-phase species, but for molecules in clusters or the condensed phase (e.g., aqueous species) the environment affects or decidedly engages in the relaxation processes.<sup>101</sup> Additional decay channels may open, and neighboring molecules engage in energy and/or electron exchange or nuclear motion within the core-

hole lifetime.<sup>102</sup> Note that electronic and nuclear motion is always coupled, but sometimes the coupling is small enough to neglect it. In the next section of my thesis I will introduce two intermolecular/interatomic (non-local) autoionization mechanisms.

### 2.2.2 RESONANT PHOTOEMISSION

If the incident photon energy is not sufficient to liberate a core electron, but large enough to promote that electron into an initially unoccupied orbital, the process is referred to as resonant excitation. The resonantly excited system remains in an excited but neutral state. Accordingly, emission upon resonant photoexcitation can occur via different radiative (resonant inelastic X-ray scattering (RIXS)<sup>103,104</sup>) and non-radiative (resonant photoemission (RPE)<sup>105</sup>) relaxation channels. I only focus on the non-radiative contribution, which can be divided into two main processes. First, for spectator Auger decay an electron from an occupied orbital recombines with the core-level vacancy. The excess energy is then used to emit an initially uninvolved valence electron. Compared to ‘normal’ Auger decay (2h), spectator Auger decay results in an one-hole state (1h). The additional negative charge screens the core hole which leads to an increased KE of the spectator Auger electron as compared to ‘normal’ Auger electrons. Second, if the initially excited electron participates in subsequent decay one refers to participator Auger decay. Figure 2.2 visualizes the process in an energy-level diagram. The energy gained by a participator decay equals the initial excitation energy. As a consequence, an Auger electron created via participator Auger decay carries the exact same kinetic energy as a photoelectron created by direct photoionization. Thus, RPE complements the photoionization process with a lifetime delay which adds up to enhanced signal intensity in an RPE experiment.<sup>106,107</sup> The intensity of the RPE spectrum is, however, not just a superposition of the individual processes (participator Auger decay plus direct photoionization). Instead, the electron wave function amplitudes of both processes add up coherently and the resulting intensity profile follows the Fano-formalism.<sup>108</sup> A typical example is the water O 1s  $\rightarrow$  4a<sub>1</sub> transition. The corresponding resonance energy is around 535 eV. At resonant photon energies 535 eV <  $h\nu$  < 538 eV participator Auger decay intensifies the water valence features in a PE spectrum. Above the O 1s ionization threshold (>538 eV photon energy) the participator Auger electrons vanish and extended Auger features dominate the PE spectrum.

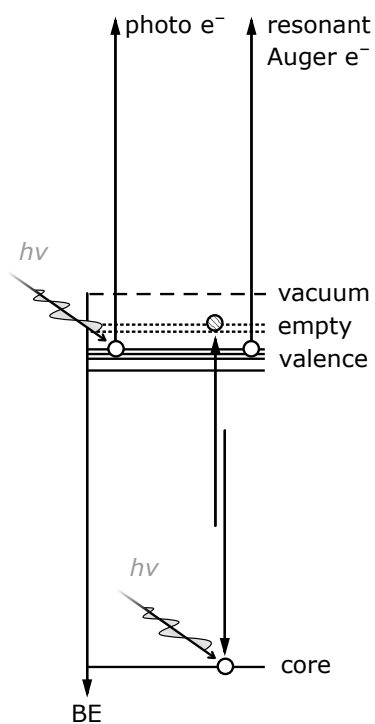
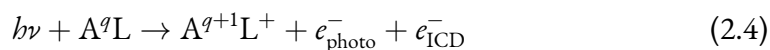


**Figure 2.2:** Diagram of the energy levels involved in a resonantly enhanced photoemission process. The core level electron is promoted to an unoccupied orbital and decays directly after in the vacancy it left behind (participator Auger decay). The excess energy can be used to eject an electron from a higher lying (valence) state. The resulting Auger electron has the exact same kinetic energy as a direct photoelectron from the same (valence) orbital. Unfilled circles indicate electrons involved in the ionization/decay process.

RPE spectroscopy can be a very powerful technique to measure photoemission signal from systems where regular PE spectroscopy is not sensitive enough. However, spectral comparability between RPE and direct photoionization is not always straightforward. A study that describes both, the basic concepts and capabilities of RPE for the detection of water dissociation at the hematite nanoparticle surface in aqueous solution can be found in Ref<sup>109</sup>.

### 2.2.3 INTERMOLECULAR COULOMBIC DECAY

If the decay pathway upon core-ionization involves neighboring sites, which is possible for weakly bound aggregates, such as van-der-Waals clusters and hydrogen-bonded systems, the process is a non-local autoionization process.<sup>110</sup> A non-local decay always causes charge separation between two separated molecules or atoms, which is mediated either by electron, nuclear or energy migration. One of these non-local processes is the interatomic/-molecular Coulombic decay (ICD).<sup>102</sup> ICD is always initiated by excitation/ionization. The excess energy gained upon subsequent electronic relaxation of a created vacancy transfers to a neighboring atom or molecule, which ionizes accordingly. ICD terminates in a doubly charged state with both positive charges located on separate entities (1h1h character), e.g., one charge sitting at a solute ion while the other charge is located at a hydration shell water molecule in an aqueous salt solution.<sup>36</sup> For a species, A, with charge,  $q$ , that decays via ICD to a neighbor, L, the whole process is described as



The second-order emitted electron is called ICD electron,  $e_{\text{ICD}}$ . The energy-level diagram of ICD is shown in Figure 2.3. The energy transfer between A and L proceeds by means of a virtual photon exchange. The virtual photon has no physical meaning and is only a rationalization of the matrix element resulting from Coulombic interactions.<sup>102</sup> This is chosen in analogy to the virtual photon exchange for dipole–dipole coupling in quantum electrodynamics.<sup>111,112</sup> The efficiency of energy transfer is inversely proportional to the sixth power of the distance between donor and acceptor. If an orbital overlap between the two constituents is given, the ICD probability shows an exponential dependency to the



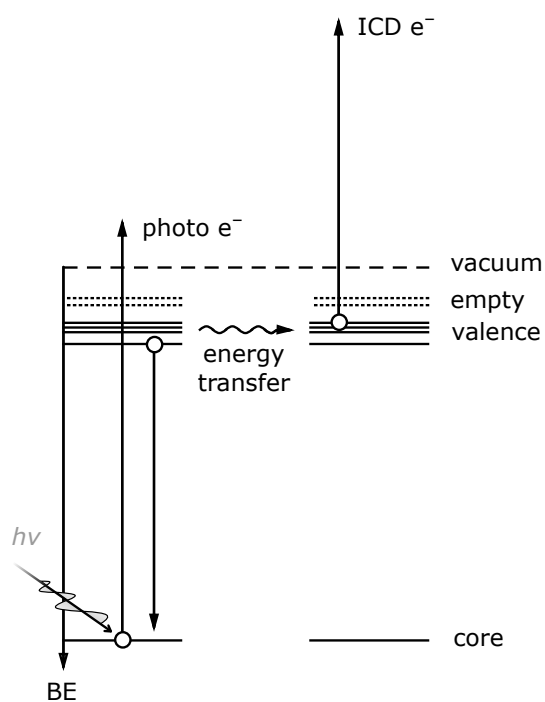


**Figure 2.3:** Diagram of the energy levels involved in an interatomic/intermolecular Coulombic decay process. Initiated by core ionization, the remaining core electron vacancy recombines with a valence electron. By transferring the excess energy to a second monomer it autoionizes accordingly. The released ICD electron is independent of the initial photon energy and carries more KE than the respective Auger decay analog, due to reduced Coulombic energy stored in the system. Unfilled circles indicate electrons involved in the ionization/decay process.

distance, making ICD extremely sensitive to small distance, essentially only involving the next neighbors of the ionized site.<sup>113</sup> In that sense, ICD is very similar to the Förster resonant energy transfer (FRET).<sup>114</sup> FRET is also mediated by non-radiative dipole–dipole coupling. However, ICD does not necessarily require resonant energy transfer as the final state of one of the involved electrons is a continuum state.<sup>101</sup> In other words, Förster transfer does not lead to ionization, whereas ICD does. Therefore, ICD is far more general than resonant energy transfer.

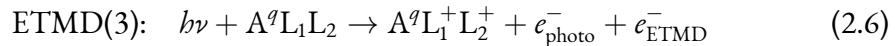
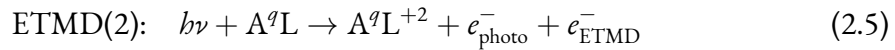
ICD is an ultrafast relaxation pathway, which proceeds on the timescale of sub-100 fs and its probability depends strongly on the number of nearest neighbors; the more neighbors, the faster ICD proceeds.<sup>101,115</sup> Nonetheless, if energetically feasible, local Auger decay rates usually dominate ICD rates, making experimental observation of ICD challenging. Differentiation between Auger and ICD electrons can be realized by either discriminating Auger decay (by the choice of the system), or by careful electron KE analysis. The final states in ICD are populated by two positive charges distributed between two separated sites, as compared to local Auger decay that has both charges at one location (compare Figure 2.1 and Figure 2.3 ). Accordingly, for ICD the total energy is lowered due to reduced Coulomb repulsion between the final state charges. Thus, considering two identical monomers, ICD creates second-order electrons with slightly higher KEs as compared to the respective Auger electrons. Another way to observe ICD is by detecting the two positively charged ionic products which repel each other (Coulomb explosion) upon ICD. The strength of the repulsion depends on the ion–ion distance and a measurement of the ionic momenta reveals the initial molecular arrangement.<sup>116,117</sup>

ICD was first predicted in 1997<sup>118</sup> and experimentally verified six years later by PE spectroscopy studies of atomic neon clusters, where a non-radiative decay has been observed, which is possible only by electron emission from neighboring sites of the vacancy.<sup>115</sup> This early work laid the foundations for exploring ICD in more complex systems. The first demonstration of ICD in aqueous solution was presented in 2008, by resonantly exciting O 1s from OH<sup>−</sup> aqueous solution.<sup>119</sup> The respective RPE spectrum showed signal corresponding to ICD decay between OH<sup>−</sup> and coordinated water. A sensitivity of ICD to solvent structure in liquids has been found for both Auger decay and ICD.<sup>120,121</sup> Few years later, a comparison of the autoionization features between normal and deuterated

water in liquid phase revealed that, due to its distance sensitivity, ICD spectroscopy is an ideal tool for probing local hydrogen-bond strengths, nuclear dynamics and solvent structure.<sup>36</sup> I will describe the details of this latter study in Chapter 5.

#### 2.2.4 ELECTRON-TRANSFER MEDIATED DECAY

Unlike Auger decay and ICD, for electron-transfer mediated decay (ETMD) the electron vacancy (upon ionization/excitation) is refilled by an electron from a neighboring atomic or molecular species.<sup>122</sup> The excess energy is either used to autoionize the electron donor itself (Auger-like), or a third, so far uninvolved species is being ionized (ICD-like). The first is referred to as ETMD(2), whereas the latter is referred to as ETMD(3).<sup>123</sup> The numbers in brackets indicate how many species are involved in the process. Similar to Auger decay and ICD, the ETMD electron is independent of the initial photon energy. However, ETMD produces charges that are not located on the initially photoionized molecule. Thus, the initially ionized site remains neutral upon ETMD, whereas it is singly charged after ICD and doubly charged after Auger decay. Whether the final two-hole state is located on a single (2h) or shared between two (1h1h) entities, depends on the actual decay pathway, as is shown in the following equations:



Both ETMD processes are sketched in Figure 2.4. The difference in Coulombic repulsion is reflected in the KE of the outgoing ETMD electron,  $e_{\text{ETMD}}$ , making it possible to experimentally differentiate between ETMD(2) and ETMD(3). For certain species ETMD is found to be a very efficient mechanism for the production of dications. Compared with direct double photoionization, ETMD has a several orders of magnitude higher efficiency to produce doubly charged final states.<sup>122</sup>

ETMD was first theoretically described for neon-argon dimers.<sup>124</sup> The authors of this study introduced ETMD as a process competing with ICD and concluded that ETMD is about four orders of magnitude less efficient for that particular system. With decreasing intermolecular distance ETMD becomes however more prominent. At small distances

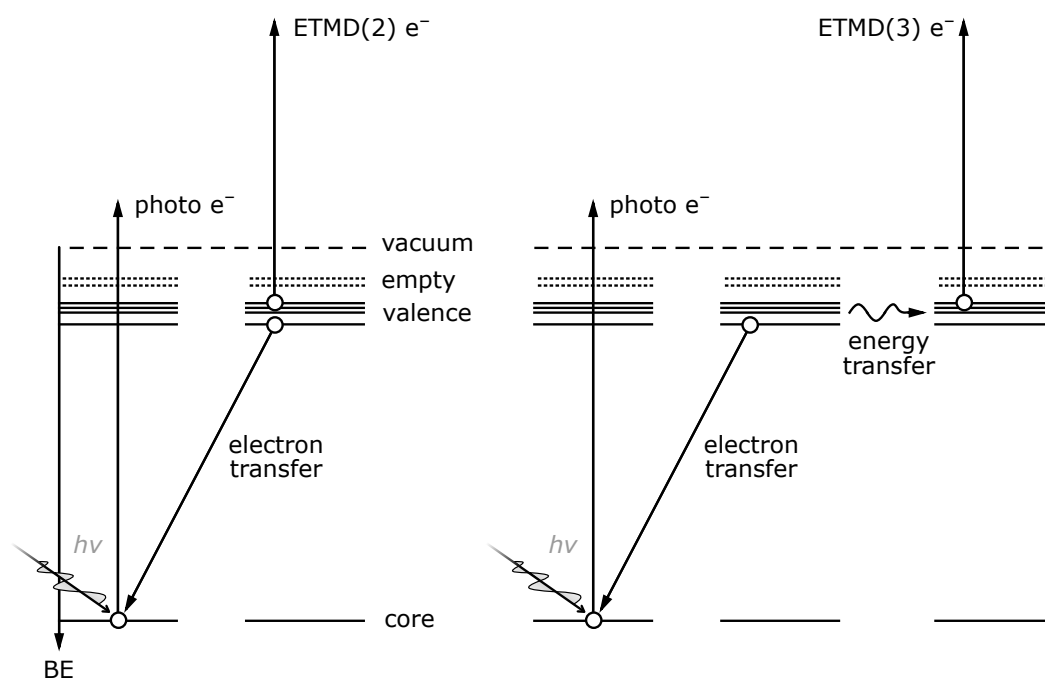


**Figure 2.4:** Diagram of the energy levels involved in an electron-transfer mediated decay process. Initiated by core ionization, the remaining core electron vacancy recombines with a valence electron from a second monomer. The excess energy is used to autoionize the transfer-electron donor itself (left) or a third, so far uninvolved monomer (right). The created ETMD electron is independent of the initial photon energy. Unfilled circles indicate electrons involved in the ionization/decay process.

ICD is only one order of magnitude more efficient. The lower ETMD efficiency is caused by the fact that electron transfer crucially depends on orbital overlap, whereas ICD has a  $R^{-6}$  (with nuclear distance  $R$ ) dependency and does not require orbital overlap.<sup>102</sup> Thus, ETMD is expected to be only relevant in systems comprising subunits with more directional and stronger orbital overlap. As such, ETMD is an ideal sensor for first solvation shell composition of strongly coordinated systems. However, observation of electronic signal from ETMD is most probable in scenarios where ICD and local Auger decay are energetically not possible or highly unfavored. This is the case, for example, for an Ar 3s vacancy in a Kr-Ar-Kr trimer<sup>125</sup> and also for solvated lithium ions<sup>122,126,127</sup> which have no remaining electrons to relax into a Li 1s vacancy.

In Chapter 6, I will present experimental proof for ETMD to be sensitive to changing solvation in aqueous environments. ETMD is a relatively recently discovered process, at least from an experimental point of view. There are other systems where ETMD may be favored over the alternative processes (or reasonably competitive), which are of particular relevance, but we are only beginning to understand these processes, and trying to exploit them as spectroscopic tool. I will also discuss ideas of studying ETMD in more complex systems.

### 2.3 SPECTRAL INTENSITIES

PE energies can be measured with great precision (modern electron analyzers feature few-eV energy resolutions<sup>32</sup>). For certain types of experiments, it is important though to be able to quantitatively interpret signal intensities which can then be used to determine relative sample composition or fragments of chemical processes. On a fundamental level, signal intensities, i.e., the photocurrent in a PE spectrum result from electronic transitions between an initially bound state (eigenstate  $\langle i |$ ) and a final state (eigenstate  $| f \rangle$ ). The corresponding probability  $\Gamma$  is given by Fermi's golden rule<sup>128</sup>

$$\Gamma_{i \rightarrow f} = \frac{4\pi^2}{b} |\langle f | \hat{H} | i \rangle|^2 \delta(E_f - E_i - h\nu) \quad (2.7)$$

where  $E_i$  and  $E_f$  are the energies of the initial and final state, respectively, and the  $\delta$ -function ensures energy conservation. Based on the approximations made in Sec-

tion 2.1, the Hamiltonian  $\hat{H}$  can be reduced to the interaction of an electron in an electromagnetic field,  $\vec{E}$  (so-called ‘dipole approximation’)

$$\hat{H} = -\vec{\mu} \cdot \vec{E} \quad (2.8)$$

with  $\vec{\mu}$  being the dipole moment. As a result, in this simplified but powerful picture, the photoionization process only depends on the initial and final state energies and the electrostatic potentials that are present.

However, in practice, signal intensities depend on multiple factors, some of which are of experimental nature (as collection space angle, spectrometer transmission function, target density and photon flux), and some of physical nature (as ionization cross-section, probing depth, etc.). Some of the experimental factors are unknown and expressed as an alignment factor,  $A$ . The total PE intensity can be described by<sup>27,129</sup>

$$I = A \cdot F \cdot n_{\text{target}} \cdot \sigma_{\text{photo}} \cdot l_{\text{IMFP}} \quad (2.9)$$

with the photon flux,  $F$ , the element-specific density,  $n_{\text{target}}$ , the electron’s inelastic mean free path (IMFP),  $l_{\text{IMFP}}$ , and the relative photoionization cross section,  $\sigma_{\text{photo}}$ . The photoionization cross section is an element and orbital specific quantity which describes the probability of photoionization to occur upon interaction of an atom or molecule with an incident photon. In fact, also the polarization of the incoming light has an impact on the  $\sigma_{\text{photo}}$  of polarized atoms.<sup>130–132</sup>

Free electrons have a significantly high propensity to interact with matter, i.e., much higher than photons.<sup>133,134</sup> The IMFP describes the mean distance an electron travels before undergoing inelastic scattering. Inelastic scattering causes loss of electron KE and to some extent loss of information relevant in a PE experiment.<sup>135</sup> Electron scattering is a generic term referring to either electron–electron and electron–phonon collisions (for solid state and very low electron KEs), or electron-impact ionization/excitation.<sup>27</sup> As such the IMFP has an inverse dependency on the scattering cross section of a material,  $l_{\text{IMFP}} = (n_{\text{total}} \cdot \sigma_{\text{el}})^{-1}$ , with the electron total scattering cross section  $\sigma_{\text{el}}$  (not to confuse with  $\sigma_{\text{photo}}$ ) at a given kinetic energy and the material density  $n_{\text{total}}$  (not to confuse with the target specific  $n_{\text{target}}$ ).<sup>29</sup> In most cases  $n_{\text{total}}$  is not homogenous but a depth distribu-

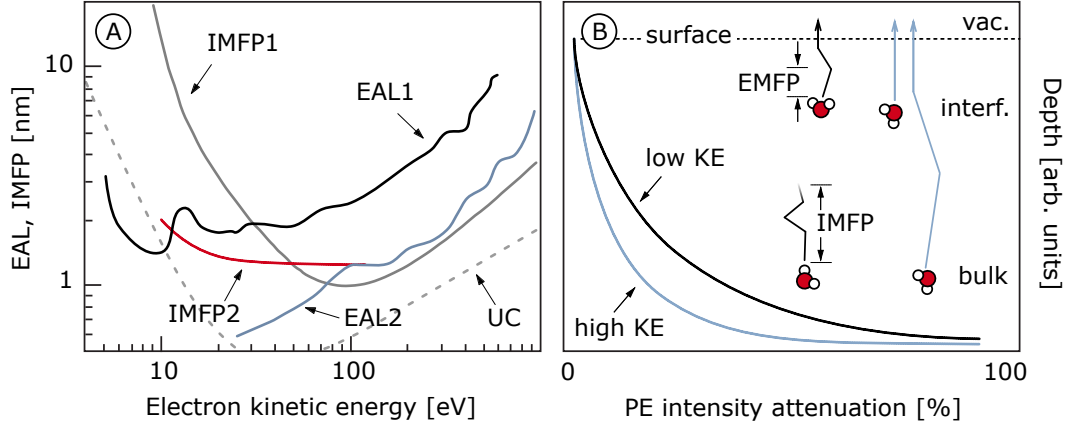


**Figure 2.5:** Panel A: Experimentally derived effective attenuation length (EAL) and simulated inelastic mean free path (IMFP) curves for liquid water. Details are described in the main text. Panel B: Schematic graphic of the electronic attenuation as a function of the depth into solution for the two cases: high and low initial electron KE. Inelastic and elastic mean free path (IMFP and EMFP) are depicted in the inset sketch. Panel A adapted from Ref<sup>136</sup>.

tion density function,  $n(z)$ , with depth,  $z$ . The total attenuated intensity  $I(z)$  for the photoelectrons escaping the material can be approximated as an integral, weighted exponentially by the IMFP:

$$I(z) = \int n(z) \cdot e^{\frac{-z}{\text{IMFP}}} dz \quad (2.10)$$

The IMFP is statistically defined as the length at which the total number of electrons without KE loss drops to  $1/e$ . For few selected metals the ‘universal curve’ (UC) has been established which presents the electron IMFP in nanometers as a function of the electron KE (see Figure 2.5A).<sup>133</sup> The UC has its minimum between 10 eV and 100 eV, an energy range where inelastic scattering is very effective since valence and core-level excitations with energies  $\geq 7$  eV lead to electron energy loss. While being well established for the solid phase, the IMFP is still under debate for the liquid phase.<sup>129,137,138</sup> Few studies have accomplished experiments giving access to the IMFP curve for liquid water; results are compiled in Figure 2.5A. Presented curves are deduced from angular distributions as obtained from core orbital photoelectron signal intensities of pure water (blue curve, EAL2),<sup>129,137</sup> and the black curve (EAL1) uses experimental values derived independently.<sup>138</sup> The gray curve (IMFP1) was estimated using a Bethe surface constructed from liquid water inelastic X-ray scattering data.<sup>138</sup> The red curve (IMFP2) reflects an estimate that has been scaled to better agree with energy-dependent photoelectron angu-

lar distributions.<sup>137</sup> The gray dashed line is a reprint of the UC.<sup>133</sup> Note that the UC is referenced to the Fermi level whereas liquid water IMFP and EAL are referenced to vacuum level. The curves shown in Figure 2.5A have their minima at approximately 50 eV to 100 eV KE, where the IMFP for electrons is only about some few nm. In a PE experiment, electron signal measured with low-KE energy will thus be strongly attenuated, whereas the attenuation is smaller for high KEs. The depth-dependent signal attenuation for electrons with low and high KEs is sketched in Figure 2.5B.

Due to the small IMFP, soft-X-ray PE spectroscopy probes mainly a thin layer at the sample surface and PE experiments have to be performed under vacuum conditions.<sup>139,140</sup> Only recent techniques as the liquid-jet approach used in my studies were successfully applied to PE spectroscopy from highly volatile liquids (discussed in Chapter 3).<sup>30,31</sup> Inelastically scattered electrons lose their energy and appear as enhanced background signal in the low-KE energy region of a PE spectrum, close to the zero-energy cutoff (see also Figure 2.1). In contrast, elastic scattering occurs as an unbound electron propagates through a medium and eventually scatters by maintaining its energy but changing its initial direction. This includes excitation of rotational modes, thus the term ‘elastic’ is often used less strictly, including minimal energy loss. Accordingly, elastic scattering leads to broadening of the angular distribution in a PE experiment. The travel distance accompanied with elastic scattering is called elastic mean free path (EMFP), see also the inset in Figure 2.5B. The actual type of energy loss depends strongly on the KE of the electron.<sup>141-143</sup>

Due to the typically unknown factors contributing to PE signal intensity and the fact that in most cases knowledge of relative intensities is sufficient, y-axes of PE spectra are usually labeled with ‘arbitrary units’ in the literature. In my thesis, PE spectra will always have a blank y-axis, representative of arbitrary units and plotted linear with PE yield.



# 3

## Experimental Methods

Photoemission spectroscopy from liquids is a fast-developing research field.<sup>144</sup> To overcome the problems of electrons having a small escape depth in a condensed phase, multiple approaches have been made during the last 40 years. In 1973, Siegbahn and Siegbahn used liquid solutions of low vapor pressure to measure photoelectrons.<sup>72,75</sup> These samples were introduced into the vacuum chamber via a needle with the exiting viscous liquid constantly flowing over a metal substrate. The jet diameter was about 1 mm and the sample chamber, which was pumped down to the sample's vapor pressure, was separated by differentially pumped slits from the high-vacuum part of the electron analyzer. Due to the restriction to low-vapor-pressure samples the field of liquid phase PE spectroscopy entered a state of hibernation until advance was made with the introduction of micrometer-sized liquid jets, compatible with vacuum techniques.<sup>28,145-148</sup> Photoemission spectroscopy from liquids is still a young research field and only a handful approaches have been developed to date. For a long time the liquid-jet was the only experimental technique to access highly volatile samples with PE spectroscopy. Only very recently, new experimental approaches such as near-ambient pressure PE spectroscopy, ultra-thin graphene membrane flow cells and the 'dip-and-pull' method have become available.<sup>30-35</sup> However, to guarantee a continuous replacement of the liquid sample and

to eliminate the potential influence of cell membranes or substrates affecting the measured signals, the use of a liquid jet with micrometer thickness is still the most attractive alternative. Detailed description of the liquid-jet technique and its advantages over the other approaches will be given in Section 3.2. This Chapter also includes descriptions of the light source, the vacuum chamber, and detection techniques.

### 3.1 LIGHT SOURCES

The choice of an ideal light source is determined by the photon energy and temporal resolution. For coincidence techniques as used in this thesis (described in Section 3.5) sources with low photon flux and kHz to MHz repetition rates are necessary. Moreover, pulsed light of high repetition rate suits liquid-jet experiments as it prevents sample space charging due to ionization.<sup>149</sup> Table-top laser systems provide pulses with high photon flux and are widely available,<sup>150,151</sup> but are usually limited to the extreme ultra violet regime. X-ray energies  $>5$  eV can only be achieved using higher harmonics, which reduces the photon flux.<sup>152</sup> Energies of tens to several hundred eV (soft-X-ray) are needed to cover the full electronic structure of light elements. Other common laboratory-based X-ray sources such as Helium II (21 eV and 41 eV respectively) and Al  $K\alpha$  (1486.6 eV) provide higher energies but lack temporal resolution. Also, these sources are not tunable in energy. Precisely selected photon energies are of great importance, as the initial excitation determines the possible decay channels. Too high photon energies enable too many possible decay pathways, making a spectral deconvolution impossible. On the other hand, too low energies do not initiate second-order decay at all. Especially for RPE experiments precise excitation of a well-known orbital is absolutely necessary.

First attempts on building energy-tunable light sources have been made by bombarding charged particles on selected metals to produce X-ray radiation at the metal element characteristic energies.<sup>14,153,154</sup> This so-called ‘Bremsstrahlung’ (German for ‘braking radiation’) is produced upon electron-impact ionization. Generally speaking, Bremsstrahlung is any radiation produced due to the de-/acceleration of a charged particle. Yet, accessible photon energies are pre-determined by the targeted material and the photon flux is rather low ( $10^9$  photons/sec).<sup>155</sup> High flux radiation and continuously tunable photon energies could only be realized with synchrotron radiation (which is a certain

type of Bremsstrahlung) produced at synchrotron facilities. The idea was introduced in 1945 with the theoretical description of highly collimated electromagnetic radiation which propagates tangentially to a charged particle with relativistic velocity, if this particle is forced on a bent trajectory.<sup>156</sup> Natural sources of synchrotron radiation are astronomical objects like pulsars or quasars containing hot plasma moving inside strong magnetic fields.<sup>157</sup> Synchrotron radiation features several unique properties. First, it provides a wide-range energy spectrum from infrared up to hard-X-ray radiation. Furthermore, it is highly intense (high photon flux), and pulsed with a well-defined time structure for both pulse length and spacing. Moreover, synchrotron light is naturally polarized. Synchrotron radiation is considered to be highly ‘brilliant’, which is a term that combines the aspect of intensity, angular divergence, cross-sectional area of the beam and bandwidth. The greater the brilliance, the more photons of a given wavelength and direction within a certain bandwidth are concentrated on a spot per unit of time.

All experimental data presented in this thesis were measured at the U49/2 PGM1, U41 PGM, or UE56/2 PGM1 undulator beamlines of BESSY II at the Helmholtz-Zentrum Berlin. All three beamlines provide a small focus of  $100 \times 22 \mu\text{m}^2$  (U49),  $20 \times 10 \mu\text{m}^2$  (U41) and  $90 \times 90 \mu\text{m}^2$  (UE56).<sup>158,159</sup> The energy resolution of all beamlines is better than  $\Delta E/E = 5 \cdot 10^{-4}$ , i.e., 350 meV for 650 eV photon energies and 60 meV for 200 eV energies. The photon flux at around 100 eV photon energy is on the order of  $3 \cdot 10^{13}$  photons/sec for all three beamlines. The micro-focus spot of the U41 beamline suited our experimental requirements best, but unfortunately stopped operation in 2015.

### 3.1.1 SYNCHROTRON RADIATION

A synchrotron facility provides radiation of a broad energy range. The emitted photon energy can be derived from the energy loss of a charged particle under acceleration.<sup>160</sup> It is assumed that, independent of the true trajectory, a charged particle moves along a linear path for infinitesimal small distances. It moves with velocity,  $v$ , and emits photons since it is forced on a bent trajectory. The emitted radiation propagates tangentially with the velocity of light,  $c$ . The charged particle emits a photon at position A, at  $t = 0$  and at position B, at  $t = t'$ . The time of observation is at  $t = t' + dt$ , which implies that the

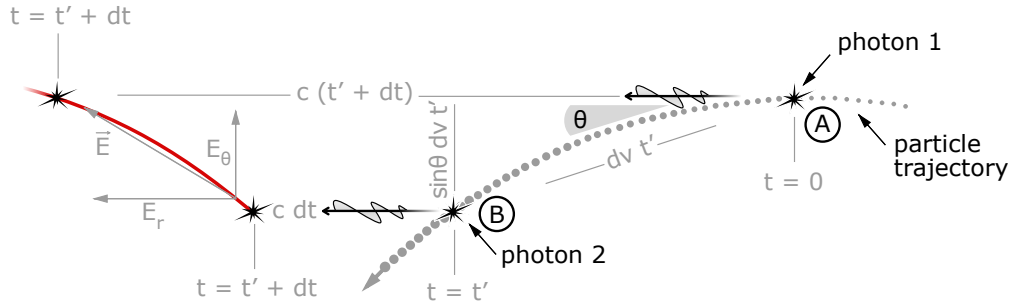


**Figure 3.1:** Sketch of a charged particle on a bent trajectory (gray dotted line). For infinitesimal short time scale the particle passes a linear path and emits parallel light beams (black lines). The solid red line indicates one stationary electric field line seen by an observer at time  $t = t' + dt$ . Local electromagnetic field components (gray arrows) parallel and perpendicular to the photon propagation emerge due the inhomogeneity of the emitted field line.

light emitted at point A travelled already a distance of  $c(t + dt)$  and the light emitted in point B a distance of  $c dt$ . This causes a local inhomogeneity of the electromagnetic field which can be separated in a radial,  $E_r$ , and a tangential,  $E_\theta$ , part as shown in Figure 3.1. The ratio of the electric field components can be expressed by the ratio of the two photon path lengths which were emitted from point A and B as

$$\frac{E_\theta}{E_r} = \frac{t \sin \theta dv}{c dt} \quad (3.1)$$

In the limit of infinitesimal times ( $dt \rightarrow 0$ ) the particles' acceleration can be assumed constant ( $dv/dt = a$ ). By substituting  $r = ct$  and inserting Coulomb's law the equation reduces to

$$E_\theta = \frac{q}{4\pi \epsilon_0 r c^2} a \sin \theta \quad (3.2)$$

with the vacuum permittivity,  $\epsilon_0$ , and the particle charge,  $q$ . The energy flow per area is given by Pointing's law

$$S = \epsilon_0 c E_\theta^2 \quad (3.3)$$

Inserting Equation (3.2) into Equation (3.3) and integrating the energy flow over all directions gives Larmor's formula

$$\frac{dE}{dt} = \frac{e^2 a^2}{6\pi c^2 \epsilon_0} \gamma^4 \quad (3.4)$$

where  $q$  has been replaced by the elementary charge,  $e$ , and the Lorentz factor,  $\gamma = 1/\sqrt{1 - (\frac{v}{c})^2}$ , has been added to account for relativistic electrons. Thus, the power of the radiation scales with  $\gamma^4$ , i.e., with the energy of the electron beam to a high order, which is one reason why large synchrotron facilities of several hundred meters circumference are needed in order to accelerate electrons up to 8 GeV.<sup>161</sup>

### 3.1.2 UNDULATOR DEVICE

The generation of synchrotron light underwent three major generations in the last 60 years.<sup>162</sup> The first generation was only parasitic, because accelerators were primarily used for high-energy or nuclear physics. As the concept proved its success, dedicated electron storage rings were built to produce synchrotron light. These facilities, which are designed with the main focus on producing synchrotron light, are considered as second-generation synchrotron sources. Storage rings are to date the basis for most synchrotron sources. The demand for bright light sources raised and dedicated insertion devices such as undulators were developed (third generation of synchrotron sources). Undulators consist of an array of closely spaced vertically oriented dipole magnets of alternating polarity. An electron beam passes longitudinally through the array, while its trajectory oscillates in the horizontal plane on a sine-shaped path. As the electron trajectories bend due to the magnetic field, they emit synchrotron radiation. Light amplification occurs if the oscillating electron beam,  $\lambda_{\text{el}}$ , is in phase with the emitted photons wavelength,  $\lambda_{\text{ph}}$ , as depicted in Figure 3.2. Under this assumption, the amplified photon wavelength can be expressed as the difference between the mean velocities of the electron beam along the y-direction,  $\vec{v}_y$ , and  $c$ :

$$\lambda_{\text{ph}} \approx (c - \vec{v}_y) \frac{\lambda_{\text{el}}}{c} \quad (3.5)$$

The electron velocity has only contribution in the xy-plane whereas the magnetic field lines are aligned along the z-axis. The Lorentz force dictates the trajectory. Solving the relativistic Lorentz force for a given magnetic field strength,  $B_0$ , with the electron mass,  $m_{\text{el}}$ , results in the undulator formula (for a more detailed derivation see Refs.<sup>163,164</sup>):

$$\lambda_{\text{ph}} = \frac{\lambda_{\text{el}}}{2\gamma^2} \left( 1 + \frac{K^2}{2} \right), \quad \text{with} \quad K^2 = \left( \frac{e B_0 \lambda_{\text{el}}}{2\pi m_{\text{el}}} \right)^2 \frac{1}{c^2} \quad (3.6)$$

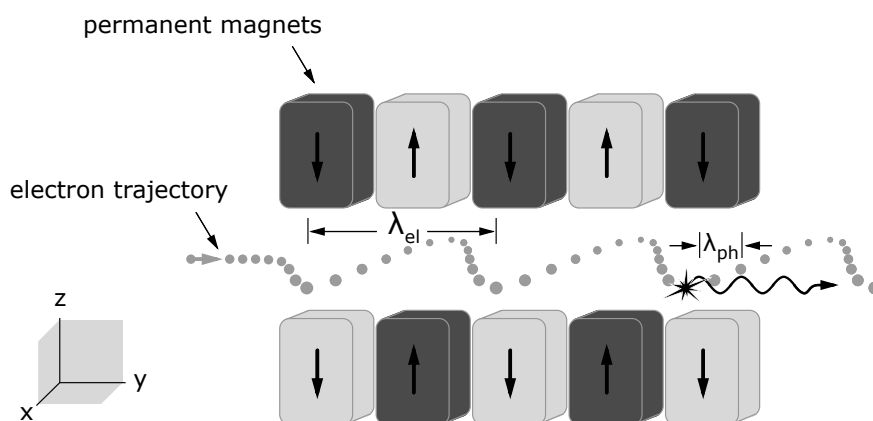


**Figure 3.2:** Concept schematic of an undulator. Two arrays of alternating permanent magnets are arranged in two rows such that each magnet faces another magnet of opposite polarity (in z-direction). The emerging magnetic field lines force electrons (with velocity along the y-axis) on a sine-shaped path (oscillations in x-direction). The permanent electron de-/acceleration induces light emission whereas photons which are in phase with  $\lambda_{el}$  become amplified via constructive interference.

The relation shows that the emitted synchrotron radiation has longer wavelengths at rising magnetic field strengths and shorter wavelengths at rising electron energies. The electron energies are determined by the accelerator, but the field strength in the undulator section can be tuned mechanically by adjusting the vertical spacing (gap) between the pole tips. The radiation cones emitted at each bend along the propagation direction interfere constructively. As a result, the so-created synchrotron beam features multiple spectrally narrow peaks – a fundamental and its higher harmonics. The beam is highly collimated in both, horizontal and vertical direction, that is, the beam has a high spectral brightness.

### 3.2 THE LIQUID MICROJET

The small IMFP of free electrons was ever since a problem in PE spectroscopy. Despite the early pioneering work from Siegbahn and Siegbahn on highly viscous samples,<sup>75</sup> PE experiments were mostly performed under ultra-high vacuum conditions, which restricted this method to solid-state and vapor-phase physics. The key idea for applying PE spectroscopy to the liquid phase is by creating a micrometer-sized stream which introduces the liquid sample into vacuum.<sup>145</sup> The small cylindrical size of the jet ensures a fast gas density decrease, scaling inversely quadratic with distance ( $r^{-2}$ ) from the jet axis,

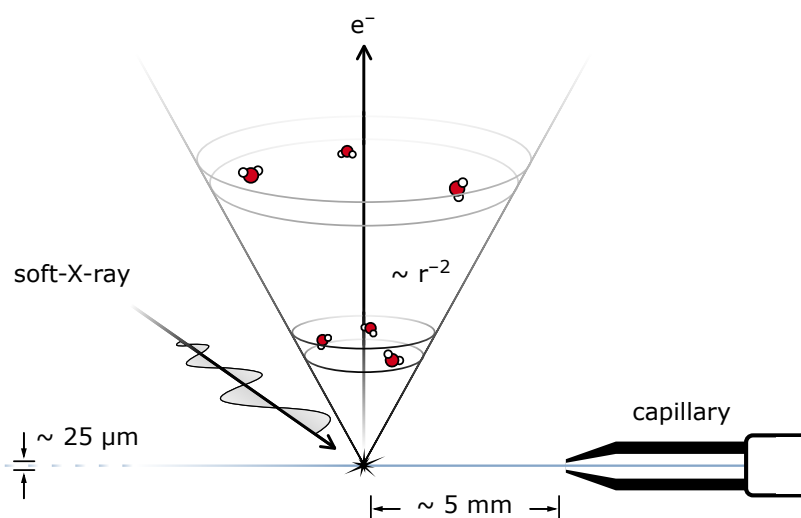


**Figure 3.3:** Sketch of a liquid jet introduced into a vacuum chamber via a glass capillary to maintain a pressure of  $10^{-5}$  mbar. The jet of  $\sim 40 \text{ ms}^{-1}$  velocity has an approximately 1 cm length of laminar flow. The interaction spot at which liquid and X-ray beam interact is very close to the capillary exit; commonly at  $\sim 5$  mm distance. The vapor density decreases with increasing distance to the jet with  $r^{-2}$  so that a sizeable number of ejected electrons can reach the detector without energy loss. Experiments described in this thesis are usually measured with capillaries which create a jet of around  $25 \mu\text{m}$  in diameter. The X-ray beam is focused down to a comparable size in order to minimize vapor contribution to the PE signal.

which increases the IMFP tremendously, from  $\mu\text{m}$  to  $\text{mm}$  (see Figure 3.3). The liquid jet is formed by pushing water with approximately  $0.5 \text{ ml/min}$  through a tapered glass capillary with an orifice of typically  $10\text{--}35 \mu\text{m}$  size. The choice of orifice size is a tradeoff between vapor phase contribution, and sample waste (preferentially small diameter) and jet stability (preferentially large diameter). The high pressure needed to form the jet is delivered by a high-performance liquid chromatography (HPLC) pump connected to the nozzle via chemically resistant tubings. As the jet has to be extremely stable over time, an additional loop is installed between nozzle and HPLC pump in order to damp pulsing induced by the pump. Prior degassing of the sample solution avoids gas bubbles which, when reaching the nozzle outlet, would lead to freezing inside the glass nozzle.

The so-created jet has a velocity of around  $40 \text{ ms}^{-1}$ , fast enough to maintain an approximately 1 cm length of liquid laminar phase until solid ice droplets are formed due to cooling by evaporation. In the laminar region, the jet is considered to be in a thermodynamic equilibrium, since evaporative cooling is effectively much slower than liquid–liquid molecule collisions. The time for evaporation of a monolayer of water

( $\sim 0.3$  nm) is between 50 ns<sup>148</sup> and 100 ns<sup>29</sup> for a  $>10$   $\mu\text{m}$  jet. Molecular rearrangement and molecule–molecule collisions that lead to equilibrium occur on a picosecond (ps) timescale, hence four orders of magnitude faster than evaporation. The diffusion coefficient of solutes in liquid water is comparably high. It takes approximately 4 ns for a solute of 1 mol per liter (M) bulk concentration to form a surface adsorbate layer, and 40  $\mu\text{s}$  for a 0.01 M concentration.<sup>29</sup> The given jet velocity implies that the liquid flow needs approximately 125  $\mu\text{s}$  to reach the point of observation at 5 mm distance from injection; thus the jet setup resembles natural surface/bulk concentrations. The temperature also resembles ‘real’ conditions, as a room-tempered water jet of 21  $\mu\text{m}$  diameter loses only about 20 K during this time due to evaporation.<sup>148</sup>

Another advantage of the liquid jet is that in PE experiments from electrically non conducting or poorly conducting aqueous liquid surfaces, electrostatic charging is considerably reduced through rapid liquid exchange. However, it has been known from the very first measurements that a neat liquid water jet will be almost inevitably charged, and only some of the underlying contributions to charging have been discussed.<sup>165–167</sup> There are two major sources of charging the liquid jet, (i) electrokinetic charging, induced by friction between sample and glass capillary/tubings and (ii) space charging due to photoionization of the liquid sample. In addition, a third effect (iii), the possible change or evolution of the solution surface potential due to a molecular dipole layer must be taken into account. This effect is associated with the orientation of molecules at the water/aqueous solution–vacuum interface; and related, the possible larger surface propensity of one type of charged species (atomic ions such as iodide) compared to another species will give rise to a double layer. It is perhaps useful to recall that molecular adsorption on single-crystal surfaces (typically investigated by PE spectroscopy in ultra-high vacuum) is well known to cause changes of the sample’s work function.<sup>168</sup> For aqueous-solution PE spectroscopy this has never been considered. Any of these three effects will influence the kinetic energy of the photoelectron (the position of the PE peak) that is measured in the experiment.

I only mentioned the most prominent contributions to potential jet charging. Other effects, such as chemical charging from dissociation of molecules (due to breaking of either covalently or electrostatically bound systems), could be considered as well, but are expected to have only minor contribution. Distinction and quantification of these con-



tributions in the PE spectra is beyond the recent experimental capabilities, and will have to await more dedicated liquid-jet designs. These effects make every single microjet experiment unique and careful calibration of each experiment is crucial. For most experiments, however, addition of millimolar salt concentrations is sufficient to prevent evolution of local space charges induced by high-flux radiation and electrokinetic charging. Accurate energy calibration is one motivational aspect of Chapter 4.

### 3.3 SOL<sup>3</sup>

The experimental station SOL<sup>3</sup>, at which the majority of the experiments described here was conducted, was built at the synchrotron facility BESSY II in order to measure PE spectra from volatile samples. I was fully involved in planning, constructing and commissioning SOL<sup>3</sup>. A detailed description of the setup together with proof-of-principle measurements can be found in Ref<sup>32</sup>. SOL<sup>3</sup> consists of three main components: (i) The electron analyzer, (ii) the interaction chamber, and (iii) a differentially pumped stage between analyzer and chamber (see Figure 3.4). The electron spectrometer used for SOL<sup>3</sup> is a ‘ScientaOmicron R4000 HiPP-2’ high-resolution hemispherical electron energy analyzer developed for near-ambient pressure photoelectron spectroscopy.

The analyzer (i) consists of two hemispherically shaped electrodes (radius of the outer hemisphere is 200 mm), set at high electrostatic potentials in order to disperse electrons of different KEs for imaging. All electrons that enter the analyzer through a slit are forced on a curved trajectory. The particular trajectory depends on the initial electron KEs and the electrode potential, but also the angle of entry will affect the electron paths through the analyzer. The choice of electrode potential filters out all electrons of a certain energy. Electrons with KEs different from this so-called ‘pass energy’ collide with the analyzer walls and get thus eliminated before reaching the detector unit at the end of the analyzer, opposite to the entrance slit. However, all electrons with KEs within the given pass energy window ( $\pm 8\%$  distribution) are imaged onto a 2-dimensional detector, consisting of a micro-channel plate (MCP)/fluorescence screen stack and a charge-coupled device (CCD) camera. The detector image registered by the CCD camera corresponds to a rectangle of 560 simultaneous energy channels and 460 channels in the spatial/angular dispersion. The pass energy is fixed during a PE measurement. Electrostatic lenses prior to

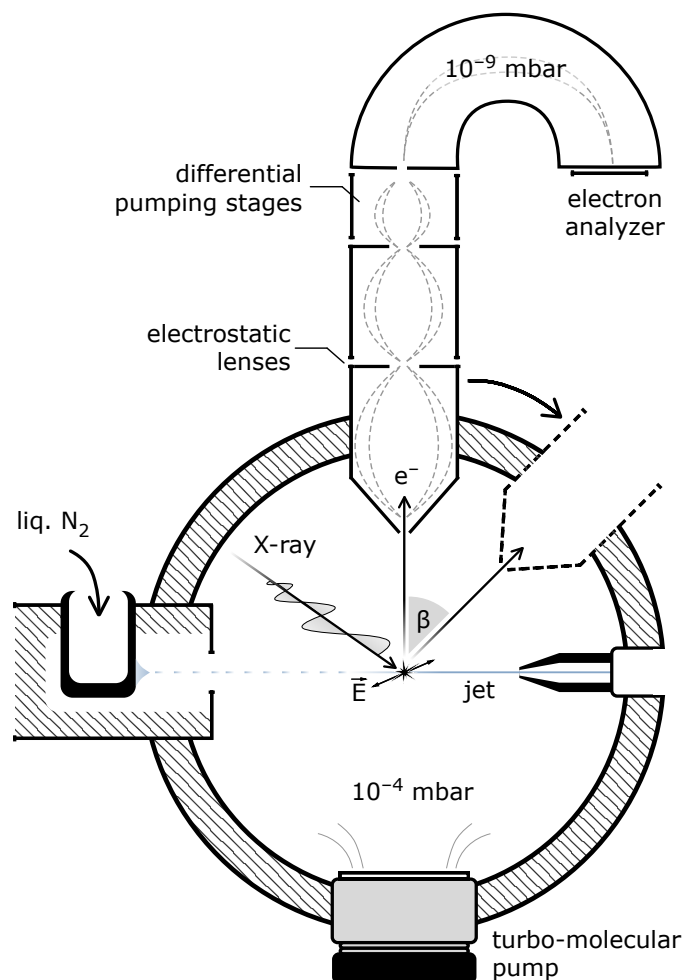


**Figure 3.4:** Sketch of the basic components of the SOL<sup>3</sup> experimental station for liquid phase PE spectroscopy at BESSY II. The jet is introduced into the experimental vacuum chamber via a glass capillary. After passing the interaction region, where liquid and X-ray beams are crossed, a liquid nitrogen cooled vessel catches the jet. The distance to the interaction region is  $\sim 5$  mm for the glass capillary and on the order of  $500 \mu\text{m}$  for the analyzer entrance. Photoelectrons enter the differentially pumped electron analyzer via an entrance cone of  $500 \mu\text{m}$  diameter size. This is necessary to separate the  $10^{-4}$  mbar atmosphere of the interaction chamber from the high vacuum part of the analyzer. The electron analyzer is differentially pumped featuring four chambers separated by mm-sized pinholes. An electrostatic hemisphere energy disperses the electron stream which eventually hits a detector consisting of a fluorescence screen-MCP stack. The detector stack requires ultra-high vacuum conditions, e.g., a pressure of  $10^{-9}$  mbar. SOL<sup>3</sup> features the possibility to measure PE angular distributions (anisotropy parameter,  $\beta$ ) by rotating the electron analyzer around the X-ray beam axis.

the entrance slit enable well-defined de- or acceleration of the electron beam. By continuously changing the lens voltages, it is possible to scan through the distribution of electron KEs. The R4000 is capable of detecting electron energies ranging from 5 eV to 6000 eV (XUV to soft-X-ray) in transmission mode and 10 eV to 6000 eV in angular mode. Nine different slit sizes at the hemisphere entrance are available, of which we used mostly the largest one ( $0.5 \times 30 \text{ mm}^2$ ) for enhanced signal collection rate. At this slit size, the energy resolution is 25 meV at 200 eV KE (for 20 eV pass energy). The energy resolution,  $\Delta E$ , of an electron analyzer depends mainly on the slit size,  $d$ , the radius of the hemisphere,  $R$ , and the acceptance angle,  $\alpha$ , and can be estimated using the relation:

$$\Delta E = \left( \frac{d}{2R} + \frac{\alpha^2}{2} \right) \quad (3.7)$$

The hemispherical analyzer is pumped to reach a final pressure of  $10^{-9}$  mbar at the MCP. Ambient pressure operation of the R4000 analyzer is accomplished with the help of a multi-stage pumped drift stage (iii). A 500  $\mu\text{m}$  entrance cone separates the first section of the drift stage from the interaction chamber and is followed by three differentially pumped drift stages to overcome the maximal pressure difference of  $10^{-10}$  mbar between interaction chamber and detector. Each section is equipped with one or two 250 L/s turbo-molecular pumps and separated by  $\mu\text{m}$ -sized pinholes. Electrostatic lenses guide the electrons through these pinholes.

Near-ambient pressure measurements can be realized at SOL<sup>3</sup> either by using liquid jet experiments or liquid–surface approaches stabilized at high relative humidity. Maximal pressures equal 20 mbar H<sub>2</sub>O or 50 mbar N<sub>2</sub> at the sample position.<sup>30,31</sup> When running the liquid jet experiment, the pressure in the interaction chamber can be as low as  $10^{-4}$  mbar; this pressure is reached by using two cold traps (metal cylinders with approximately 1000 cm<sup>2</sup> surface area each) filled with liquid nitrogen and a 1600 L/s non-corrosive turbo-molecular pump. The interaction chamber (ii) is designed to be rather big which facilitates maintenance and also increases the volume for evaporated water and hence decreases the gas load at the jet. The interaction point is in the middle of the chamber, where synchrotron beam, jet, and analyzer axis intersect (center of Figure 3.4). Downstream the jet axis, at the opposite side of the interaction chamber, is a dedicated liq-

uid nitrogen vessel which is needed to collect and freeze the liquid jet immediately. The jet itself is mounted on an xyz-manipulator with  $\mu\text{m}$  screws to allow for precise positioning. The distance between analyzer cone and liquid jet is kept small (approximately  $500\ \mu\text{m}$ ) to reduce the travel length of the free electrons. Analyzer cone and jet can be observed through front and bottom windows. A camera with  $\geq 30\times$  magnification is installed to monitor the jet. This is crucial for an initial rough positioning of the jet and for stability monitoring, as it is important to have jet, synchrotron beam focus, and analyzer aligned to overlap and kept stable on a  $\mu\text{m}$ -scale.

SOL<sup>3</sup> is equipped with a manual swing mechanism, allowing for quick rotation of the analyzer about the synchrotron-light beam axis. This rotation allows for detection of angular distributions of emitted electrons at any angle between  $0^\circ$  and  $90^\circ$ , with respect to the polarization vector of the synchrotron light, which is typically in the floor plane. To rotate the analyzer, breaking the vacuum is necessary. External magnetic fields, in particular, the earth magnetic field, are compensated for by a Helmholtz-coil arrangement consisting of three pairs of separately powered magnetic coils. Currents are optimized to yield zero magnetic field, measured with a Hall sensor in front of the electron analyzer entrance cone.

### 3.4 MAGNETIC-BOTTLE TIME-OF-FLIGHT SPECTROMETER

Another approach to measure electron KEs, is by detecting their velocities using a time-of-flight (TOF) spectrometer. This technique is particular useful for time-resolved experiments due to the possibility of collecting a whole electron spectrum in a single shot. The basic concept of a TOF spectrometer is that the time required for an electron to pass a defined length is related to its kinetic energy via

$$KE = \frac{1}{2}m_{\text{el}} \cdot \left(\frac{s}{t}\right)^2 - eU \quad (3.8)$$

with the electron mass,  $m_{\text{el}}$ , elementary charge,  $e$ , retardation voltage,  $U$ , and the flight length,  $s$ . Flight times of the setup I used ( $\sim 60\ \text{cm}$  flight length and  $10\text{--}100\ \text{eV}$  KEs) are typically on the order of  $50\text{--}200\ \text{ns}$ . Accordingly, it is clear that this method needs pulsed light with a repetition rate lower than the electron flight times, such as kHz lasers, free

electron lasers or specific operation modes of synchrotron sources. BESSY II provides the so-called ‘single-bunch mode’ in which the repetition rate is reduced to 1.25 MHz (800 ns between pulses). The electron flight times were synchronized to an electron bunch marker signal provided by BESSY II and were finally recorded using a multi-hit capable time-to-digital converter of 60 ps bin width. Measured time channels translate directly into flight times by putting 1 channel to 60 ps. Note that for short electron flight times the number of electrons reaching the detector within the 60 ps is higher than for longer flight times. This leads to unjustified high signal in the extracted spectra. A Jacobian factor,  $dt/dKE$ , has to be multiplied to every single data point to ensure area conservation in the spectrum. Calibration measurements, i.e., measuring a well-known core-hole peak at different photon energies is necessary before each single measurement to have a reliable energy reference. Nonetheless, an uncertainty of these data points leads to a systematic uncertainty of  $\pm 0.25$  eV for the kinetic energy axis of the whole spectrum.

The magnetic bottle setup used in my work is basically an electron TOF spectrometer in which additional magnetic fields dramatically increase the collection efficiency, while still covering the full kinetic energy range in a single measurement. The total efficiency is linear and between 24% and 50% (MCP efficiency already included). A detailed description of the theory of a magnetic-bottle TOF can be found in Ref<sup>169</sup>; the here used setup is best described in Refs<sup>170,171</sup>. Figure 3.5 presents a sketch of the setup. Compared to SOL<sup>3</sup> the rotatable electron analyzer is now exchanged by a TOF spectrometer and a 450 mT permanent magnet ( $\text{Sm}_2\text{CO}_{17}$ ) is placed below the interaction region; all other parts are similar. The permanent magnet creates a strong inhomogeneous field and additional coils inside the TOF drift tube create a weak homogeneous field. The so created diverging magnetic field aligns the trajectories of electrons that travel from the strong field region to the weak field region. This significantly enhances the electron collection efficiency as the collection angle is almost  $4\pi$  ( $2\pi$  for the liquid-jet geometry). The coils guide the collected electrons along the drift tube whereas the electron trajectories inside the TOF resemble a bottleneck, which is the reason for the naming of the spectrometer. After reaching the end of the drift tube electrons are counted by an MCP pair. The significantly enhanced collection efficiency and compatibility with the liquid-jet source present

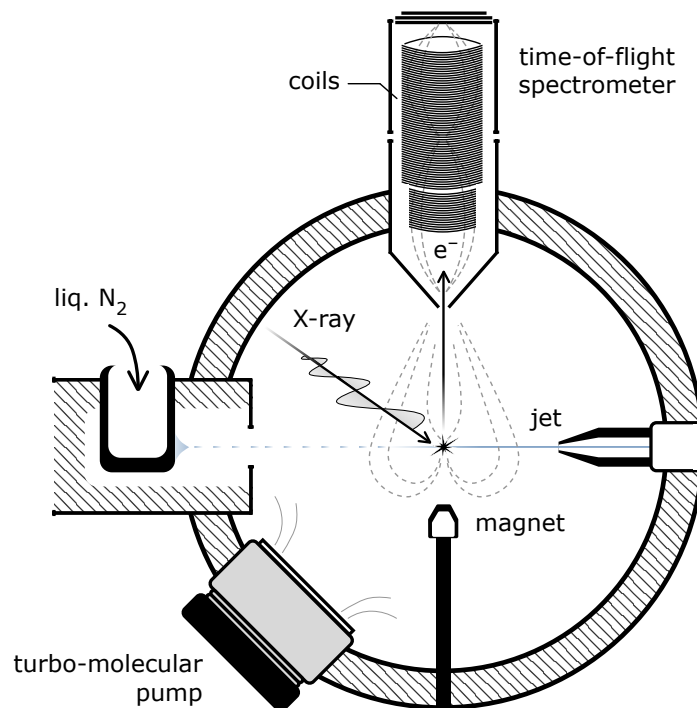


**Figure 3.5:** Sketch of the basic components of the magnetic-bottle PES experimental station for liquid phase PE spectroscopy at BESSY II. The components for handling the liquid jet are identical to the SOL<sup>3</sup> setup. The electron analyzer is replaced by a magnetic-bottle time-of-flight spectrometer featuring a drift tube with two coils, a small and a large one, in order to de- and accelerate electrons on their way to the MCP-fluorescence screen stack at the end of the spectrometer. The collection efficiency is increased by a permanent magnet placed below the point of liquid-light interaction. The magnet setup can be aligned relative to the drift tube via a xyz-manipulator. Opposite the magnet and 45 mm away from the interaction region is the entrance cone (25 mm in diameter) of the drift tube. The drift tube has an inner diameter of 85 mm and a length of 600 mm.

two obvious advantages of this detection technique; a drawback on the other hand is that angular information is lost.

### 3.5 ELECTRON-ELECTRON COINCIDENCE

As mentioned earlier, inelastically scattered electrons create a large background signal in the low-KE part of a PE spectrum. In our case ETMD creates slow electrons around 30–40 eV, as will be explained in Chapter 6. As the physical origin of two electrons – be it an ETMD electron or an inelastically scattered electron – with same KE cannot be disentangled by means of conventional PE spectroscopy, alternative detection schemes have to be used. The key idea of electron–electron coincidence detection is to selectively detect slow electrons that are coincident with a photoelectron; i.e., slow electrons that reach the detector within a defined time span after a photoelectron of known KE is detected. We reduced the photon flux considerably to about  $10^{11}$  photons/sec using a beamline slit of 1–10  $\mu\text{m}$  and an insertion device aperture of 0.1 mm. This was necessary in order to reach a situation in which, for most of the BESSY pulses, zero or one electron reaches the detector within the given time window. Each time two electrons reach the detector within that time span, a coincidence event was recorded and accordingly represented in a 2-dimensional map. The coincidence map x-axis represents the first electron and the y-axis the second one, as sketched (not measured) in Figure 3.6. The map is divided by a diagonal while the bottom-right half-map is empty. This is because our detector does not differentiate between electrons and counts always the first electron arriving at the detector as fastest electron. In the experiments described here typical acquisition times were 1800 seconds per map. In this time, typically 6 million coincidence events could be registered.

Different processes upon single-photon absorption can lead to the ejection of electron pairs. Most of the electron pairs (triggering coincidence events) are physically unrelated, be it by ionization of two separated monomers or by detection of electrons that outrun the 800-ns time window and appear in later bunches. All of these so-called ‘random events’ represent electron pairs that share independent total energies and appear as noisy background contributions to a coincidence map. Signal from electron pairs resulting from ionization followed by a second-order process, such as autoionization, shows

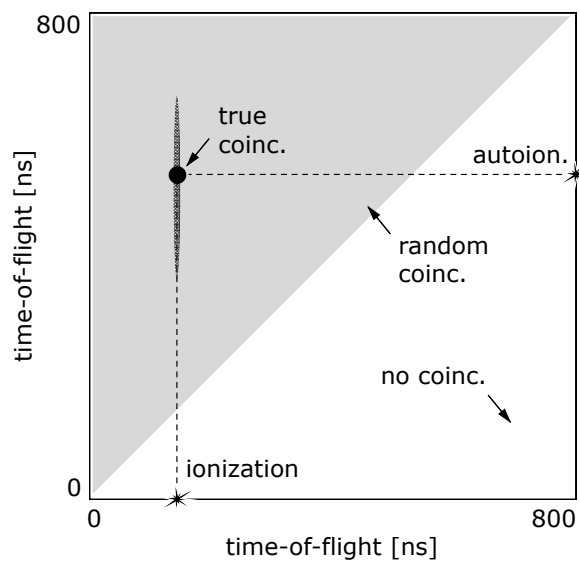


**Figure 3.6:** Principal sketch of an electron–electron coincidence map as measured with the magnetic-bottle TOF spectrometer. If a two-electron event occurs at the detector within the measuring window (800 ns in our case), the flight times of the electrons will be mapped onto a 2-dimensional representation. The fastest electron is always plotted on the x-axis which is the reason why the bottom right part of the map is empty. Random coincidences – two-electron events where both electrons are not related to the same decay process – can have all kinds of energy distributions for both electrons and appear as unstructured background. Processes that are related to an ionization event appear as dense areas along vertical lines in the map.



up along a vertical line; see shaded line in Figure 3.6. Note that the temporal delay between photoelectron (first) and autoionization electron (second) due to the lifetime of the excited, singly ionized state is at most in the few fs range and does not play a role in the interpretation of the flight times.

To extract the underlying signal of electrons only related to ionization – the ‘true coincidences’ – I select a narrow region of interest (ROI) on the x-axis that exactly covers the vertical line. Afterwards integration along the y-axis gives a spectrum that contains ionization related second-order electrons together with a random background. A binning factor of 20 is usually sufficient to ensure enough counts per channel. To get rid of background signal the same procedure was performed for a region next to the original ROI, on the right hand side. This region is considered to mostly contain signal from random coincidences and inelastically scattered electrons from true coincidences. As the new region is on the right side of the original ROI it contains slower electrons. The number of electrons recorded is generally higher for faster electrons as these arrive at the detector more frequently within a given constant time span. To account for this behavior, I rescale the integrated signal intensity of the off-region to match the baseline of the integrated ROI spectrum. Subtracting both spectra provides the background-free second-order electron spectrum. Results from using this detection method for measuring ETMD from aqueous lithium solutions are presented in Chapter 6.



# 4

## Photoemission from Liquid Water

The electronic configuration of an isolated water molecule in the ground state is  $(1a_1)^2(2a_1)^2(1b_2)^2(3a_1)^2(1b_1)^2$ , adopting a  $C_{2v}$  representation.<sup>172</sup> Within this description, the highest-energy electrons are associated with the  $1b_1$  orbital which is primarily of oxygen lone-pair character (O  $2p_x$ ) and is thus non-bonding. The lower-lying non-bonding  $3a_1$  orbital is again predominantly of oxygen p-orbital type, while the  $1b_2$  electrons dominantly contribute to the O–H bonds. The  $2a_1$  orbital results from O  $2s$ –H  $1s$  hybridization, yet it shows largely O  $2s$  character. A typical PE spectrum from liquid water using a liquid jet is presented in Figure 4.1. It consists of two main regions; the valence band orbitals are located around 10–35 eV BE, and the core level is at around 530–540 eV BE. The valence spectra were measured at 150/175 eV (liquid/gas) and the core level at 575 eV photon energies. All peaks represent molecular orbitals of the water molecule, as presented in the energy diagram in the top part of Figure 4.1. Note, that a PE spectrum of liquid water always inevitably contains a considerable amount of gas-phase water due to evaporation around the liquid jet. A spectrum of solely water vapor was measured by moving the jet out of the beamline light focus (to identify the gas-phase features), as presented in Figure 4.1 with a thin dashed line. Electron-density contours visualize the shape of molecular orbitals. The orbital plots represent computed electronic densities of

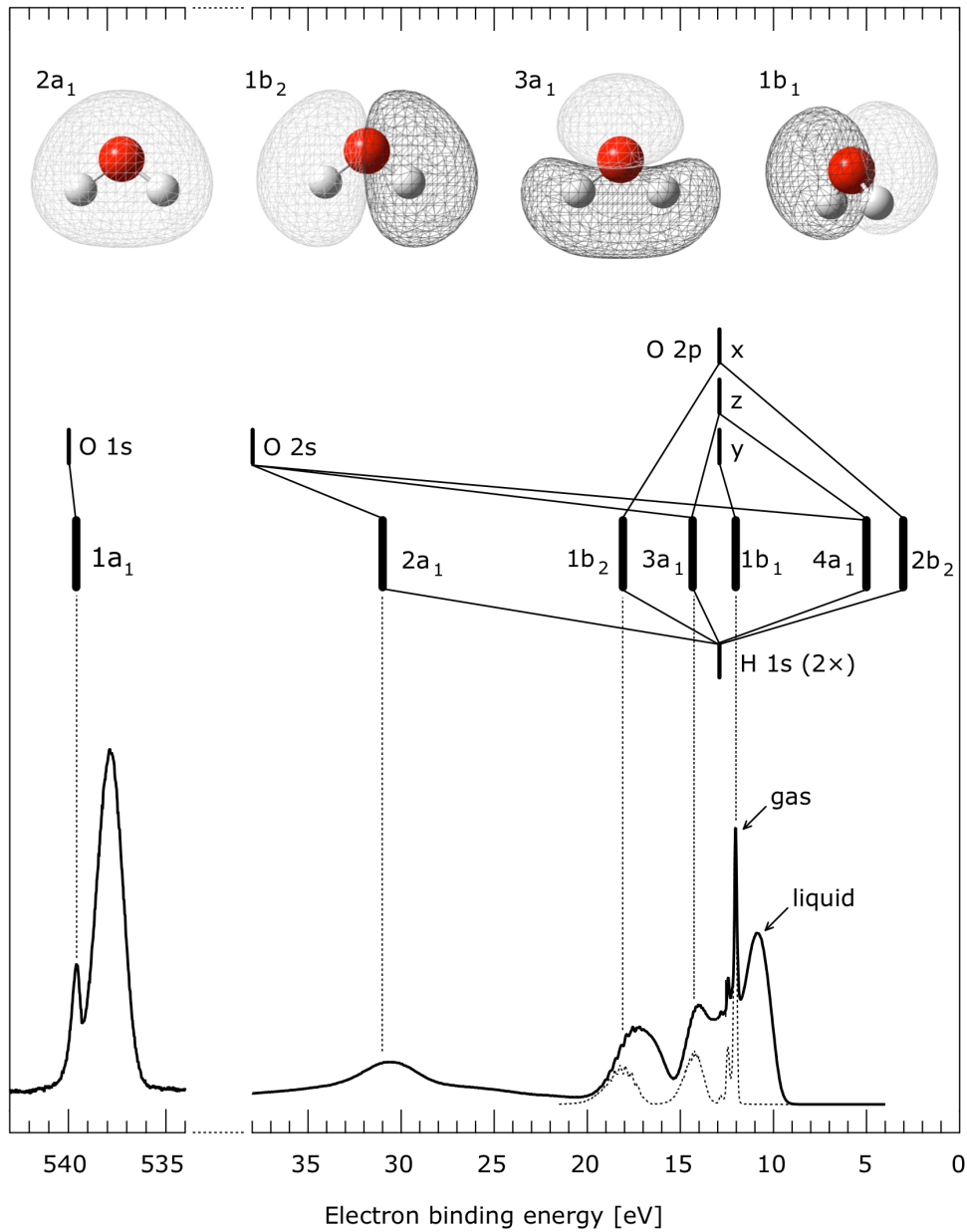


**Figure 4.1:** Top: Energy-level diagram and molecular bonding scheme of the H<sub>2</sub>O molecule. All atomic and molecular levels are positioned according to their binding energy (taken from Ref<sup>162</sup> for the atoms and from Refs<sup>173,174</sup> for H<sub>2</sub>O) on the energy scale. Electron-density contours are assigned to each molecular orbital, according to Ref<sup>172</sup>. Bottom: Liquid-jet PE spectrum from liquid water in the O 1s and valence band region. Additional signal from gaseous water is brought by the vapor waist around the liquid jet. The pure gas-phase spectrum of water is shown for the outer-valence region (9–21 eV BE, dashed spectrum). The gas spectrum is shifted by  $-0.48$  eV to align with the liquid phase spectrum. Dashed lines assign all gas peaks to their molecular orbital. Liquid phase contributions are shifted to lower BEs by some eV due to dielectric screening, as indicated by arrows for the  $1b_1$  peak.  $4a_1$  and  $2b_2$  orbitals are unoccupied orbitals and therefore not visible in the PE spectrum.

free water molecules.<sup>172</sup> Electrons of the free water molecule are tightly bound, with the first ionization energy ( $1b_1$  electron) at 12.6 eV, followed by higher ionization energies from the  $3a_1$  (14.8 eV),  $1b_2$  (18.6 eV),  $2a_1$  (32.6 eV) and  $1a_1$  (O 1s, 539.9 eV).<sup>28,29,173–175</sup> These ionization energies, which correlate with electron BEs, are solvent-shifted to approximately 1.2–1.4 eV lower values in liquid water due to dielectric screening and intermolecular interactions;<sup>176–178</sup> the gas–liquid BE shift for the O 1s core-level is 1.8 eV. Also, the distribution of electron BEs is broader for aqueous phase than for the gas phase due to the many hydration configurations adopted in liquid water. The  $3a_1$  peak in liquid water exhibits a doublet structure that arises from the strong  $3a_1$ – $3a_1$  orbital interactions in the fluxional hydrogen-bonded network;<sup>179–181</sup> this separates the  $3a_1$  in a bonding ( $3a_1H$ ) and a non-bonding ( $3a_1L$ ) orbital. This peak splitting is known to be less pronounced in liquid phase than for crystalline ice, with the differences in the ice and liquid water spectra interpreted as a consequence of the varying local geometries in the disordered structure of liquid water.<sup>179</sup>

Liquid-jet PE spectra are calibrated and presented with respect to the vacuum level. However, determination of exact absolute binding energies in a liquid-jet experiment is challenging since an inhomogeneous field between charged jet and grounded analyzer will influence the KE of emitted electrons on their way to the detector (see Section 3.2 for more detail). One of the consequences is that the measured BEs of the gas-phase  $H_2O$  orbitals are usually not proper references for assigning liquid-phase binding energies. As electrostatic potentials affect the energies of all outgoing electrons similarly, energy shifts are not peak specific and will affect the whole PE spectrum; the effect is the same as if one applies a bias voltage to a conductive sample. Therefore, determination of one stable reference in a PE spectrum allows for calibration of all other peaks. This issue was acknowledged already early on and has been a topic of debate and concern in the liquid-jet community. Examples of thorough investigations focusing particularly on this aspect involve Refs<sup>28,180</sup>. For all studies an assumption was made that the BE of a solute species can be obtained with reference to the lowest-ionization peak ( $1b_1$ ) of liquid water. The  $1b_1$  peak was chosen since it is energetically well separated from other orbitals. However, the exact value of the  $1b_1$  peak is not settled and ranges between 11.16 eV BE (onset at approximately 9.9 eV BE)<sup>28</sup> and 11.31 eV BE<sup>180</sup>. The two values were determined by

referencing the spectra to water vapor. In these studies, the gas phase peak position was constant, which is not necessarily true but a consequence of thorough grounding and a low light flux. The consequences of insufficient grounding and space charging due to high flux (effects (i) and (ii) as explained in Section 3.2) are presented in greater detail in the outlook (Chapter 8). In my studies, the  $1b_1$  BE of 11.16 eV according to Ref<sup>28</sup> is used, which I also confirmed by manually reducing the conditions leading to charging considerably. Both, sample flow rate and photon flux were reduced up to a point where charging was negligible and measured BEs did not shift any further in the PE spectrum. Note, that especially reducing the flux will inevitably decrease the signal intensities in an PE experiment.

Adding millimolar concentrations of salt to neat water is usually a good compromise between sufficient conductivity and an undistorted water spectrum. This is a very common procedure in liquid-jet experiments to reduce charging effects without sacrificing light flux. However, this leads to the question how solutes influence the electronic structure and thus the measured binding energies of liquid water. One justification for using this procedure is that even at considerably high concentrations of for example 1 M salt solution, undistorted water molecules with  $\sim 55$  M<sup>39</sup> would still be the dominant configuration. Thus, in most liquid jet studies, the assumption is made that small amounts of solutes do not change the overall electronic structure of water and PE spectra of aqueous solutions are essentially a superposition of the water PE spectrum and single solute peaks of approximately Gaussian shape.<sup>28,179,180</sup> However, until today, this assumption has never been verified. The following chapter presents my study on the influence of highly concentrated dissolved sodium iodide, NaI, on the electronic structure of liquid water, which has been recently submitted.<sup>182</sup>

#### 4.1 WATER IN THE PRESENCE OF SALT

More than a hundred years ago, the ionic theory of electrolytes was established,<sup>183</sup> yet the molecular understanding of ion–solvent interactions is still incomplete.<sup>184</sup> Even the geometric structure of neat liquid water itself remains a subject of ongoing controversy.<sup>185–190</sup> Especially at very high concentrations of several M, the effects of salt on the water electronic structure is highly unclear. One early liquid-jet study observed the water

electronic structure to be unaffected up to addition of 12 M of NaI.<sup>191</sup> This is, however, counterintuitive and presumably a consequence of the experimental resolution available at that time, because adding high concentrations of electrolytes into liquid water should have a profound effect on the electronic structure of water, especially when going to concentrations at which the water hydrogen-bond network is highly distorted\*. Also, at high concentrations, the effect of ions may be stronger than the electrostatic effects of the water molecular dipoles. Such ionic effects might be specific as different ions adopt different proximities to individual water molecules.<sup>119,190</sup> However, it is noted that the effects of ions on nearby water molecules are considerably greater for gaseous species when compared to liquid water, the latter exhibiting a large screening ability.<sup>192-196</sup> In addition to the dielectric screening by the solvent, the electrostatic attenuation brought about by the ions (i.e., Debye-Hückel screening<sup>197</sup>) must be explicitly considered. Such screening abilities will scale with electrolyte concentration. Recent studies utilizing X-ray scattering methods revealed that the influence of ions on the water structure is poor and does not extend beyond the first coordination shell,<sup>198,199</sup> with only a few exceptions where strongly hydrated ions, are found to affect the hydrogen-bond network considerably (cooperative effect).<sup>200</sup> As such the iodine anion,  $I^-$ , has been found to have an exceptional influence on the extended hydrogen-bond network due to its large polarizability that can delocalize charge towards its solvating water molecules.<sup>198</sup>

A detailed understanding of the associated effects on the electronic structure are important from a fundamental perspective as well as for applications. For instance highly concentrated electrolytes extend the water electrochemical window from 1.5 eV up to 3.0 eV, prompting recent suggestions to use such solutions in environmentally friendly water-based batteries.<sup>201-203</sup> Also, the anomalous increase in screening length that follows the classical decrease of the Debye screening length has been found to be relevant in chemistry, biology and energy storage.<sup>204,205</sup> As the structure and formation of an ionic environment is of fundamental importance for understanding electrochemical processes in water, I seek to quantify the mentioned effects in the following.

---

\*The water-to-solute ratio of a 12 M NaI aqueous solution is approximately 5:1.

## 4.2 NaI IN AQUEOUS SOLUTION: FROM LOW TO HIGH CONCENTRATIONS

Extended valence band PE spectra from 0.05 M, 0.5 M, 1 M, 2.5 M, 3 M, 4 M, 5 M, 6 M, 7 M and 8 M NaI in aqueous solution have been measured to identify and quantify specific changes of the electronic structure of water. Solutions were prepared by dissolving NaI of  $\geq 99\%$  purity (Sigma-Aldrich, #793558) in highly demineralized water (conductivity  $\sim 0.2 \mu\text{S cm}^{-1}$ ). Photon energies of 180 eV and 198 eV were used to measure the full valence spectrum. Additionally, 650 eV photons were used to be more bulk sensitive, corresponding to approximately 5 nm probing depth.<sup>136–138</sup> Several studies on interfacial density distribution of different ions have demonstrated that electrons with KEs  $> 600$  eV yield bulk properties.<sup>206–208</sup> Electrons were detected using the SOL<sup>3</sup> setup. It is particularly important to think about precision in our measurements. The U49 beamline resolution is on the order of 60 meV for  $\sim 200$  eV photon energies and 350 meV for  $\sim 650$  eV photon energies. However, from fitting analyses of the  $3a_1$ ,  $1b_2$ , and  $1b_1$  PE peaks in multiple data sets under similar conditions, it is concluded that water peak positions and widths can generally be determined with 40–60 meV uncertainties in the  $\sim 200$  eV and 650 eV photon energy data sets, which is a more realistic estimate of the accuracy of reported values. Similar uncertainties are obtained for the more intense and spectrally separated solute peaks ( $\text{Na}^+$  2p and  $\text{I}^-$  4d). In situations where solute peaks overlap with other features ( $\text{I}^-$  5p and  $\text{I}^-$  5s peaks) and solute concentrations are relatively low, the BE determination uncertainties are dominated by fitting errors in the range of 40–400 meV.

Figure 4.2 shows the valence band photoelectron spectrum from 0.5 M and 8 M NaI aqueous solution in the 5–60 eV BE range, measured at 198 eV photon energy. Both spectra are manually shifted in energy to align at the liquid water  $1b_1$  peak at 11.16 eV, and are normalized to the liquid  $1b_1$  intensity. A linear background is subtracted to account for inelastically scattered electrons. The seemingly better energy resolution of the 8 M spectrum (best seen at the gas-phase  $1b_1$  peak) is due to a better conductivity and thus more effective charge compensation as compared to the 0.5 M spectrum. As an electrostatic potential between jet and analyzer influences emitted electrons from gas phase molecules as a function of their distance to the analyzer, gas phase peaks become broadened. The large peak at 35 eV BE arises from ionization of  $\text{Na}^+$  2p. Peaks near 8 eV and 55 eV BE are due



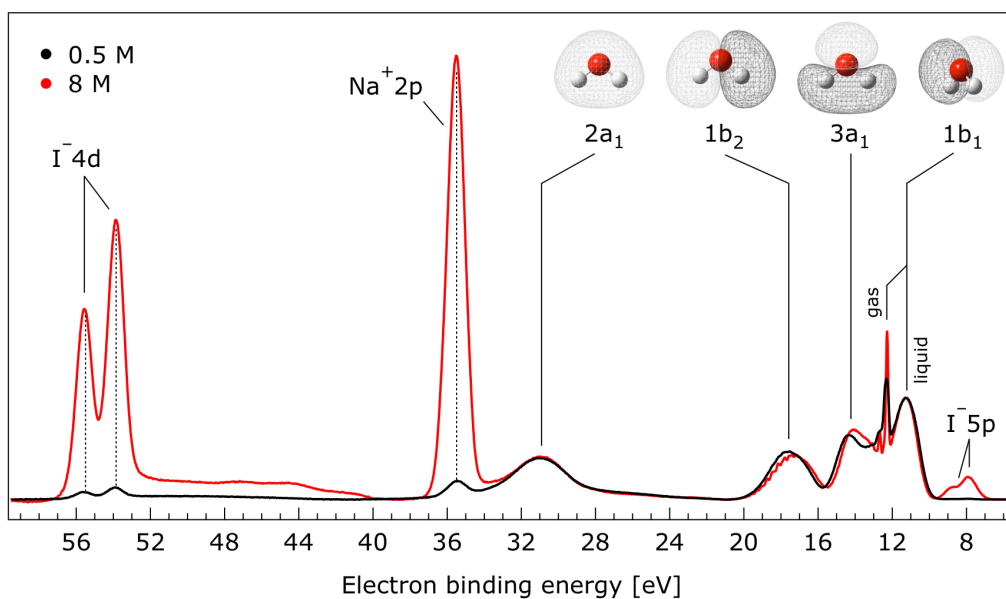


**Figure 4.2:** Valence photoelectron spectra of 0.5 M (black) and 8 M (red) NaI (aq) measured at 198 eV photon energy. Both spectra are energetically aligned at the Na<sup>+</sup> 2p and I<sup>-</sup> 4d peaks after shifting the liquid water 1b<sub>1</sub> peaks to 11.16 eV BE as indicated by dashed lines. Small structures on the slightly increased signal in the 41–52 eV BE region for the 8 M solution can be assigned to energy loss processes where Na<sup>+</sup> 2p photoelectrons excite quasi-optical transitions of water<sup>209</sup>. Schematics of the molecular orbitals of water in the top right corner are taken from Ref<sup>172</sup>. Figure reprinted from Ref<sup>182</sup>.

to ionization of  $I^-$  5p and  $I^-$  4d orbitals, respectively.<sup>29,136</sup> The double-peak structure arises from different spin-orbit states. The intensity of solute peaks scales with salt concentration but does also reflect photoionization cross sections and angular distributions of the respective orbitals.<sup>136</sup> The important observation from Figure 4.2 is that all solvent and solute peaks are aligned for the two solutions, as indicated by dashed lines. This absence of any obvious energy shifts implies that electronic structure changes due to the ion–water interactions are absent or small. Yet, detailed spectral analysis does reveal a very small energy shift of the water  $1b_2$  peak, and a change of the spectral shape of the water  $3a_1$  peak occurs, which will be focused on later in greater detail. The evolution of the energy positions of solute peaks is displayed in Figure 4.3.  $I^-$  4d undergoes only a minor spectral change when comparing 0.5 M and 8 M. A slight BE shift of  $-100 \pm 60$  meV from 0.5 M to 8 M NaI is observed, which is on the order of our estimated experimental accuracy.  $Na^+$  2p is even more stable. For low concentrations the 2p peak is dominated by background signal from water  $2a_1$ . To judge the 2p location and shape, the  $2a_1$  background has been subtracted and Gaussian fits were calculated which are almost identical for both concentrations, as indicated by shaded areas in Figure 4.3B. This procedure yields a BE shift of only  $20 \pm 60$  meV for  $Na^+$  2p when going from 0.5 M to 8 M NaI (aq). The  $I^-$  5p peak position is also rather stable with a BE shift of only  $-110 \pm 70$  meV when going from 0.5 M to 8 M NaI aqueous solution, as presented in Figure 4.3C. This observation is in contrast with previous investigations that did not observe any influence of high concentrated aqueous alkali halides on the solute BEs.<sup>211</sup> Obtained experimental BEs of the solute orbitals are summarized in Table 4.1 where energies reported for crystalline NaI are reported as well.<sup>212</sup> Note, that  $I^-$  5p orbitals form the valence band in the crystalline phase and hence, their BEs are not included. The energy positions differ between solid and condensed phase but the energy differences between all NaI peaks as well as the spin-orbit splittings are the same. This weak sensitivity to the different environments is a clear indication of a negligible effect of the solvation on the electronic structure of the ionic constituents. In this case the maintenance of constant energetic differences cannot be associated with a constant spectral offset of the cation and anion features as any solvent-induced perturbations or bonding interactions would be expected to lead to differential shifts of the anion and cation peaks.

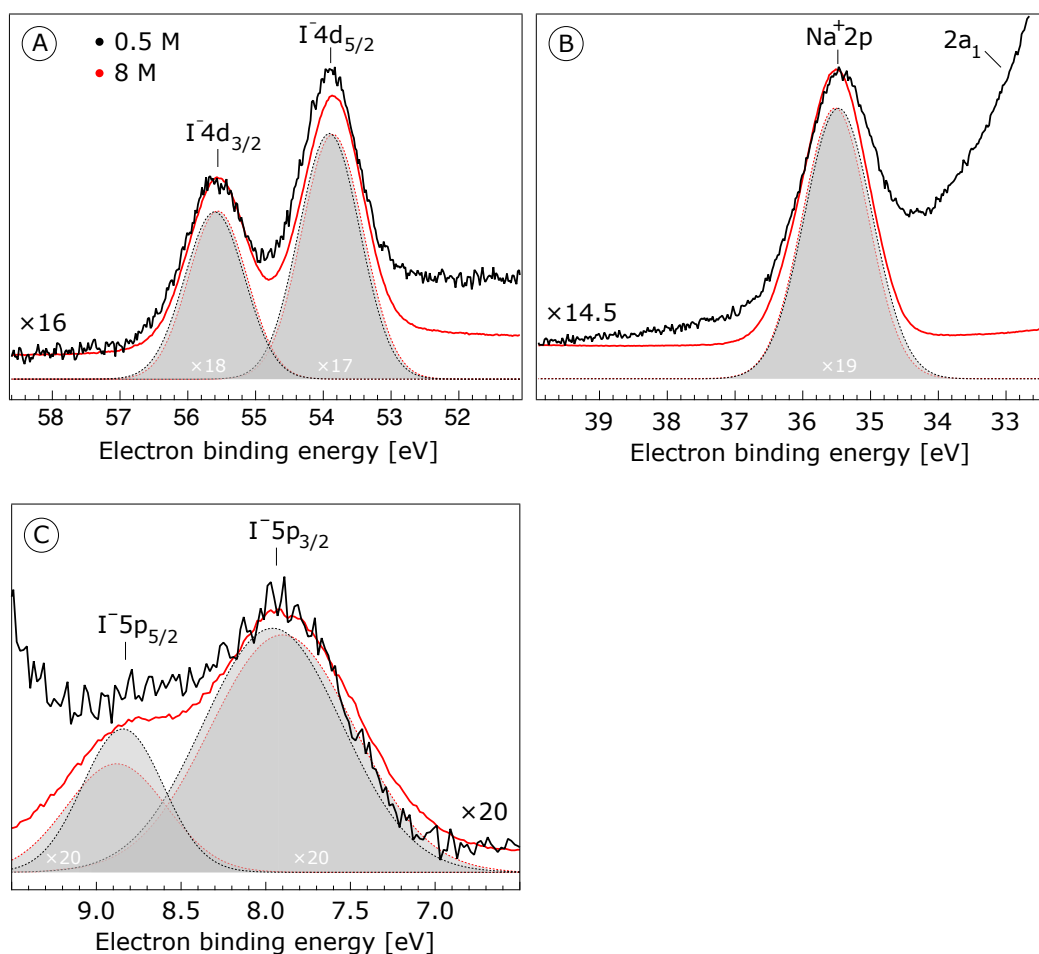


**Figure 4.3:** Photoelectron spectra of 0.5 M (red) and 8 M (black) NaI (aq) measured at 198 eV photon energy. Gaussian fits of the respective peak components are presented by gray shaded areas. The Gaussian curves are intensity normalized in order to better visualize their energy positions and widths; white numbers indicate the respective scaling factors for the 0.5 M fit curves. Panel A: Enlarged view of  $I^- 4d_{5/2}$  and  $I^- 4d_{3/2}$ . A factor of 16 is applied to the 0.5 M spectrum to yield the same peak height as the spectrum measured at 8 M solution. Panel B: Enlarged view of  $Na^+ 2p$  and  $2a_1$ . A factor of 14.5 is applied to the 0.5 M spectrum to yield the same  $Na^+ 2p$  peak height as the spectrum measured at 8 M solution. Spectral contributions due to  $2a_1$  ionization have been subtracted. Panel C: Enlarged view of  $I^- 5p_{5/2}$  and  $I^- 5p_{3/2}$ . A factor of 20 is applied to the 0.5 M spectrum to yield the same peak height as the spectrum measured at 8 M solution. Note that intensity scaling factors differ from the theoretically expected factor of 16, as background signal from inelastically scattered electrons increases with raising salt concentration. Also, iodide tends to populate the liquid–vacuum interface<sup>210</sup> which causes slightly higher iodide signal contribution in our spectra as would be expected from the bulk concentrations. Figure reprinted from Ref<sup>182</sup>.

After I demonstrated that solute ionization energies underlie only minor relative change with changing chemical environment, I want to take a closer look at the solvent water structure itself – something that has been widely overlooked in past studies. Figure 4.4 shows a concentration series of the outer valence PE spectrum from 0.05 M to 8 M NaI (aq). Note, that over the large concentration variation the viscosity of the aqueous solution increases, potentially leading to the liquid jet experiencing small changes in position which will alter the relative liquid-gas signal intensity ratio. A continuous narrowing of the gas-phase peak linewidths when going from 0.05 M to 8 M is due to a reduced vapor pressure and increased conductivity of the higher concentrated solutions. Spectra are again energetically aligned at 11.16 eV for water 1b<sub>1</sub>. Gaussian multi-peak fits have been applied for each spectrum according to Refs<sup>180,191</sup>, as indicated by shaded areas. Note the smaller water 1b<sub>1</sub> gas-phase peak in the spectra of Figure 4.4 as compared to Figure 4.2 is due to a smaller focal size of the photon beam of the U41 PGM beamline at BESSY II. It is clearly seen from Figure 4.4 that the 1b<sub>1</sub> peak remains constant in shape (location is manually fixed) for all concentrations and no specific solute-induced effect is detected. The other water peaks are strongly overlapping, yet the fit curves show a  $-370 \pm 60$  meV BE shift of the 1b<sub>2</sub>, as indicated by a small arrow in the top-most spectrum. The evolution of the peak positions obtained from Figure 4.4 is linear as visualized in Figure 4.5. Indicated error bars were determined from standard deviation of the fitting procedure. The 1b<sub>2</sub> relative energetic shift with concentration can likely be considered an absolute energetic shift as the relative separations of the solute PE spectra features and the

**Table 4.1:** Measured ionization energies from NaI in aqueous solution and in crystal phase. Aqueous phase spectra were measured using a photon energy of 198 eV to probe solute ionization energies with interface sensitivity. Crystal phase energies are taken from Ref<sup>212</sup>. Table reprinted from Ref<sup>182</sup>.

Peak	Binding energy [eV]			NaI crystal
	0.5 M	8.0 M	$\Delta E$	
I <sup>-</sup> 5p <sub>3/2</sub>	7.83 ± 0.04	7.72 ± 0.05	-0.11 ± 0.07	-
I <sup>-</sup> 5p <sub>1/2</sub>	8.70 ± 0.11	8.67 ± 0.05	-0.03 ± 0.12	-
Na <sup>+</sup> 2p	35.39 ± 0.04	35.41 ± 0.04	+0.02 ± 0.06	29.29
I <sup>-</sup> 4d <sub>5/2</sub>	53.84 ± 0.04	53.74 ± 0.04	-0.10 ± 0.06	47.68
I <sup>-</sup> 4d <sub>3/2</sub>	55.52 ± 0.04	55.44 ± 0.06	-0.08 ± 0.07	49.35

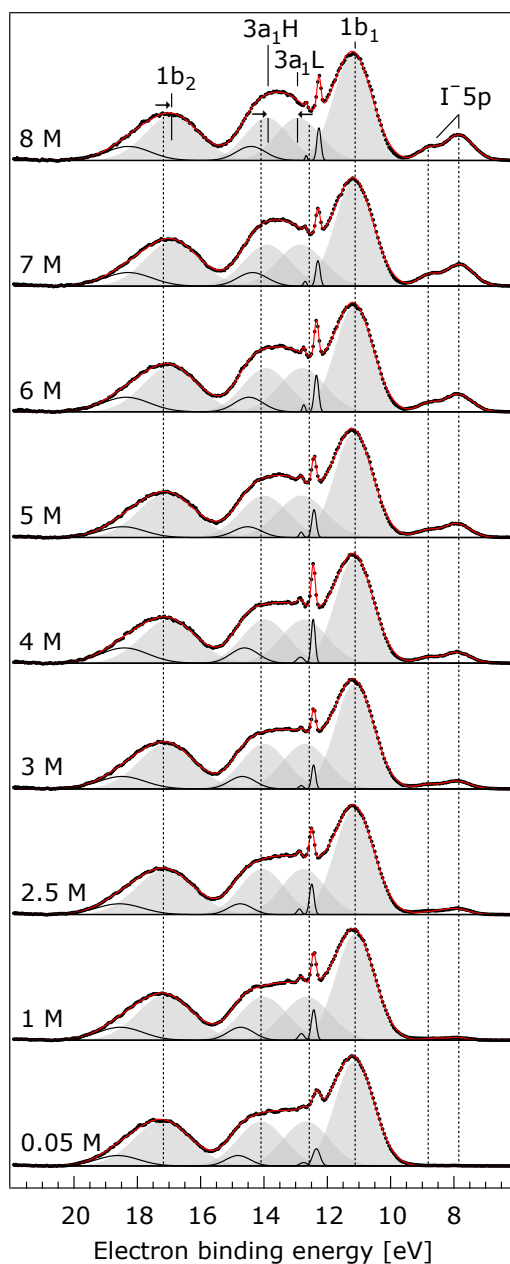


**Figure 4.4:** Valence photoelectron spectra from NaI aqueous solutions as a function of concentration, 0.05 M to 8 M. The photon energy was 180 eV. Intensities were normalized to yield the same  $1b_1$  peak heights for each solution. Peaks in grey are the Gaussian fits representing the photoelectron contributions due to ionization of the four water valence orbitals. Solid black lines represent Gaussian fits of gas-phase water valence orbitals. For the lowest concentration, the fit parameters previously reported for water were used.<sup>28</sup> For the higher concentrations, all liquid-phase peak positions were allowed to vary. Both  $3a_1$  Gaussian fit component peaks ( $3a_1L$  and  $3a_1H$ , see main body of the text for details) are constrained so that they exhibit similar widths and heights in each spectrum. Arrows indicate shifting peaks. Smaller linewidths of the gas-phase contributions for high NaI concentrations are caused by decreasing gas phase density around the jet due to reduced vapor pressure and increasing sample conductivity. Figure reprinted from Ref<sup>182</sup>.

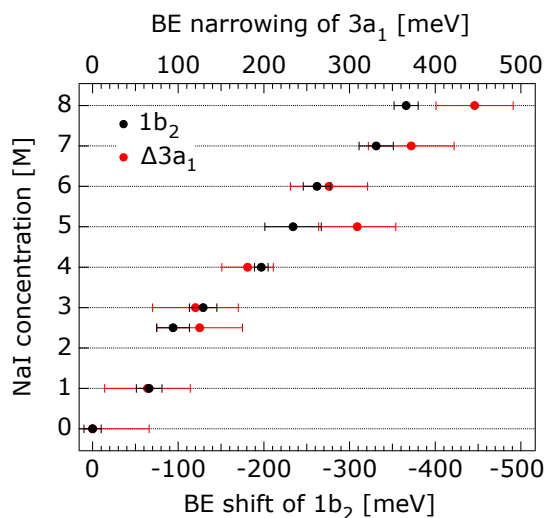


**Figure 4.5:** Changes of the water  $1b_2$  binding energy and  $3a_1$  energy splitting in NaI aqueous solutions as a function of concentration, 0.05 M to 8 M. All data are extracted from Figure 4.4. The error bars represent the uncertainties of the fitting procedure. Figure reprinted from Ref<sup>182</sup>.

liquid water  $1b_1$  feature all remain unaltered over the studied concentration range. Given the opposite charges of the solute components, the expected non-bonding nature of the water  $1b_1$  orbital, and the intermolecular bonding character of the  $1b_2$  orbital, the alternative explanation that the  $1b_2$  feature remains fixed in energy while the solute and  $1b_1$  solvent features shift is deemed likely. The second notable spectral change occurs at the position of the water  $3a_1$  peak, in the 12–16 eV BE region. At low concentrations the flat-top profile typical for neat liquid water, represented by two Gaussians, is observed. The flat top turns into a curved maximum when approaching high concentrations which can be attributed to the reduced splitting of the  $3a_1$ . Thereby the bonding  $3a_1H$  experiences a shift to lower BEs and the non-bonding  $3a_1L$  orbital a shift to higher BEs. In the spectral analysis all peak parameters were free to change, I only restricted the  $3a_1H$  and  $3a_1L$  peaks to be of similar width and intensity as has been manifested in Ref<sup>180</sup>. The shifts are indicated by small arrows in the 8 M spectrum of Figure 4.4. The total reduction of the  $3a_1$  splitting amounts to  $450 \pm 90$  meV for the 8 M concentration. The evolution is again linear as displayed in Figure 4.5. A peak width analysis of the  $3a_1$ ,  $1b_2$  and  $1b_1$  peaks revealed no noticeable trends and is therefore not further considered here.

The measurements at 180 eV and 198 eV are rather interface sensitive. To explore the ionization energies deeper into bulk, PE spectra at 650 eV photon energy have been

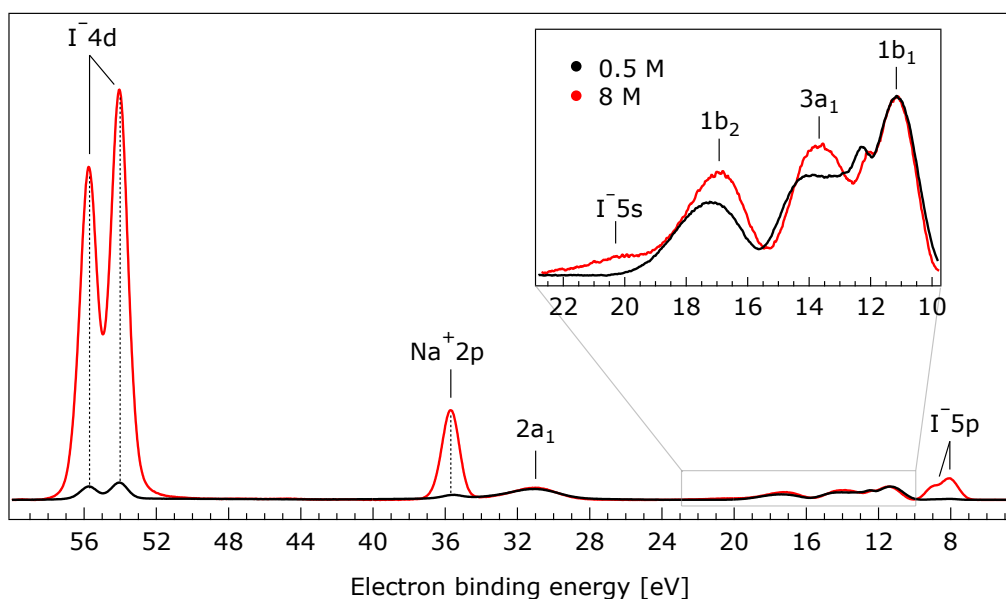


**Figure 4.6:** Valence photoelectron spectrum from 0.5 M (black) and 8 M (red) NaI (aq) measured at 650 eV photon energy. Inset: Enlarged region of the outer-valence spectrum. Figure reprinted from Ref<sup>182</sup>.

recorded. Results from the 650-eV photon energy measurements are shown in Figure 4.6. The first observation is that solute features are much more enhanced with respect to the low photon energy measurements. This is due to larger relative photoionization cross sections and photoelectron angular distributions. Most prominent is the large increase of the  $\text{I}^-$  4d to  $\text{Na}^+$  2p intensity ratio, where the initially larger  $\text{Na}^+$  peak height becomes much smaller than the  $\text{I}^-$  peak height; primarily due to the steep increase of the iodide 4d anisotropy parameter between 200 eV and 600 eV electron KE.<sup>129</sup> Note, that the detection angle was  $90^\circ$  with respect to the polarization direction of the linearly polarized incident light. Another observation is, that due to the enhanced solute intensities, an additional iodide peak – the  $\text{I}^-$  5s orbital – appears at around 20 eV BE. This feature is located at the high energy side of water 1b<sub>2</sub>, see inset of Figure 4.6. This peak shows a rather broad structure but its location is confirmed by our computation, giving a value of  $20.2 \pm 0.2$  eV. This assignment is also in agreement with the  $\sim 20\%$  smaller cross section compared to the  $\text{I}^-$  5p (value taken for atomic iodide<sup>213</sup>). Considering a further reduction of 1/3 since a s-orbital only holds two electrons while a p-orbital has six of them and

**Table 4.2:** Measured ionization energies from NaI in aqueous solution and in crystal phase. Aqueous phase spectra were measured using a photon energy of 650 eV to probe solute ionization energies with higher bulk sensitivity. Crystal phase energies are taken from Ref<sup>212</sup>. Table reprinted from Ref<sup>182</sup>.

Peak	Binding energy [eV]			NaI crystal
	0.5 M	8.0 M	$\Delta E$	
I <sup>-</sup> 5p <sub>3/2</sub>	7.82 ± 0.04	7.71 ± 0.04	-0.11 ± 0.07	-
I <sup>-</sup> 5p <sub>1/2</sub>	8.71 ± 0.10	8.67 ± 0.04	-0.04 ± 0.11	-
I <sup>-</sup> 5s	-	19.60 ± 0.40	-	11.21
Na <sup>+</sup> 2p	35.44 ± 0.04	35.41 ± 0.04	-0.03 ± 0.06	29.29
I <sup>-</sup> 4d <sub>5/2</sub>	53.89 ± 0.04	53.74 ± 0.04	-0.15 ± 0.06	47.68
I <sup>-</sup> 4d <sub>3/2</sub>	55.57 ± 0.04	55.44 ± 0.04	-0.13 ± 0.06	49.35

even further reduction due to the smaller anisotropy parameter in the case of s-orbital ionization, the intensity reduces to less than a fourth of the 5p intensity.

Most important when comparing Figure 4.6 with Figure 4.2 is that one can essentially draw the same conclusions as for the interface-sensitive spectrum. Again, when referencing both spectra to the 1b<sub>1</sub> feature, all solute ionization energies remain mostly aligned with changing concentration; minor BE shifts of maximal  $-150 \pm 60$  meV (for I<sup>-</sup> 4d<sub>5/2</sub>) are observed. The positions of the individual concentration-dependent solute peaks are summarized in Table 4.2. Also the solvent water features do not change considerably. However, small spectral variations are again observed for the orbitals 3a<sub>1</sub> and 1b<sub>2</sub>, which shift in the same direction as for the low photon energies, by a similar amount. Upon closer inspection, a  $-330 \pm 60$  meV BE shift of the 1b<sub>2</sub> orbital is extracted when the NaI concentration is raised from 0.5 M to 8 M, similar to the interface sensitive analysis of Figure 4.4. The 3a<sub>1</sub>L and 3a<sub>1</sub>H fit components are found to shift to higher and lower BEs, respectively, resulting in a narrowing of the peak separation by  $310 \pm 120$  meV. Thus, one can conclude that the concentration-dependent BE changes extracted from Figure 4.6 are equivalent to the trends observed in the interface-sensitive measurements in Figure 4.2. Considering the surface activity of I<sup>-</sup>,<sup>211,214-216</sup> the overall preservation of the PE spectrum when probing bulk rather than interface is a further clear indication of a minimal effect of solvation on the electronic structure of the ionic constituents.



### 4.3 DIELECTRIC SCREENING OF LIQUID WATER

The observation that the large structural changes, occurring when going from the dilute aqueous solution to the viscous almost crystalline-like phase, have so little effect on the PE spectra are clearly surprising. To further investigate the mechanisms theoretical simulations have been performed by the Slaviček group. Briefly described, they modelled water clusters embedded in a dielectric continuum to account for the environment of water dipoles. The clusters were generated in two different ways. First, the geometries were optimized for a water pentamer in which the central water molecule is perfectly tetrahedrally solvated (non-optimized). To investigate the effect of ionic solutes they replaced one of the water units in the water pentamer either by a sodium cation (positioned in place of the hydrogen bond donor molecule) or an iodide (positioned in place of the hydrogen bond acceptor unit), or both ions replacing two water monomers. As a second approach, they also performed molecular dynamics (MD) simulations for neat water, and 3 M and 8 M NaI in water, in order to account for structural variations. 500 randomly selected water heptamers have been extracted from simulated boxes of different sizes: 2240 water molecules in a  $\sim 3.3 \times 3.3 \times 6.2 \text{ nm}^3$  box for the neat water simulations, 2496 water molecules, 155 iodide and 155 sodium ions in a  $\sim 3.5 \times 3.5 \times 7.1 \text{ nm}^3$  box for the 3 M simulations, and 1540 water molecules, 350 iodide and 350 sodium ions in a  $\sim 3.4 \times 3.4 \times 6.4 \text{ nm}^3$  box for the 8 M simulations. The pressure was kept at 1 bar and the temperature at 300 K. Details regarding the used packages and parameters for the MD simulations are given in Refs<sup>217-226</sup>.

The ionization energies for both optimized and realistic clusters extracted from the MD trajectory were calculated in a way that the ionization is treated as an excitation into a distant center. Details of the calculation can be found in Ref<sup>227</sup>. As the models used are of a rather limited size, we account for the remaining water molecules by a dielectric continuum. However, the screening ability of electrolyte solutions is different from that of neat water and needs to be adapted.<sup>228-231</sup> The value of the dielectric constant  $\epsilon_r$  decreases with increasing electrolyte concentration for a wide range of salts. This phenomenon is called dielectric decrement and results from the formation of hydration shells around ions and ion pairs which prevents orientation of these water molecules in the external electric

**Table 4.3:** Average coordination numbers of iodide and sodium around a central water molecule as inferred from RDFs of water heptamers. Figure adapted from Ref<sup>182</sup>.

Concentration	Coordination number I <sup>-</sup>	Coordination number Na <sup>+</sup>
3 M	0.450	0.329
8 M	2.691	1.001

field. The dielectric properties of electrolytes are still subject of research and beyond the scope of the present study. The pragmatic approach is to align  $\epsilon_r$  according to our experimental data (as will be shown later). The permittivities are set to:  $\epsilon_r = 22$  for 8 M NaI solution,  $\epsilon_r = 46$  for 3 M NaI solution and  $\epsilon_r = 78.39$  for pure water. The optical dielectric constant, however, stays approximately constant, at  $\epsilon_{\text{opt}} \approx 1.78$ .

I want to start with looking at the molecular structure as obtained from MD simulations. Radial distribution functions (RDFs) are presented in Figure 4.7. Panel A displays the RDFs for the distance between water oxygen and the an-/cation for 3 M and 8 M NaI (aq). The first peak of O–Na<sup>+</sup> lies at 2.37 Å while the O–I<sup>-</sup> distance is located at 3.50 Å, which is in line with neutron diffraction studies.<sup>232,233</sup> With the RDFs it is possible to determine the coordination numbers of the ions, as presented in Table 4.3. The RDF of Na<sup>+</sup>–I<sup>-</sup> shows a first maximum at  $\sim 3$  Å as presented in Figure 4.7B. This first peak indicates contact ion pairs, while the second maximum at  $\sim 5$  Å is an indication of solvent-shared ion pairs. The fraction between contact- and solvent-shared ion pairs increases when going from 3 M to 8 M concentration as the number of available hydrating water molecules decreases. Figure 4.7C represents the RDFs for O–O for 0 M, 3 M and 8 M aqueous NaI solution. The structural changes inferred from the O–O distance are only marginal. However, for the 8 M solution, the RDFs differ significantly. The strong decrease of the first maximum indicates that the water hydrogen bond structure is strongly distorted which is brought about by ions coordinated around most of the water molecules. In summary, the impact on the overall water structure for 3 M NaI solution is small with average coordination numbers of only 0.450 for iodide and 0.329 for sodium (see Table 4.3). In 33% of the 500 simulated structures the sodium cation resides within the first hydration shell, while only 15% are tetrahedrally coordinated, featuring an ideal O–H...I<sup>-</sup> angle of 109°. The iodide is in the first solvation shell for 44% of the structure, with 27% being tetrahedrally coordinated. Less than 5% have both, anion and cation in

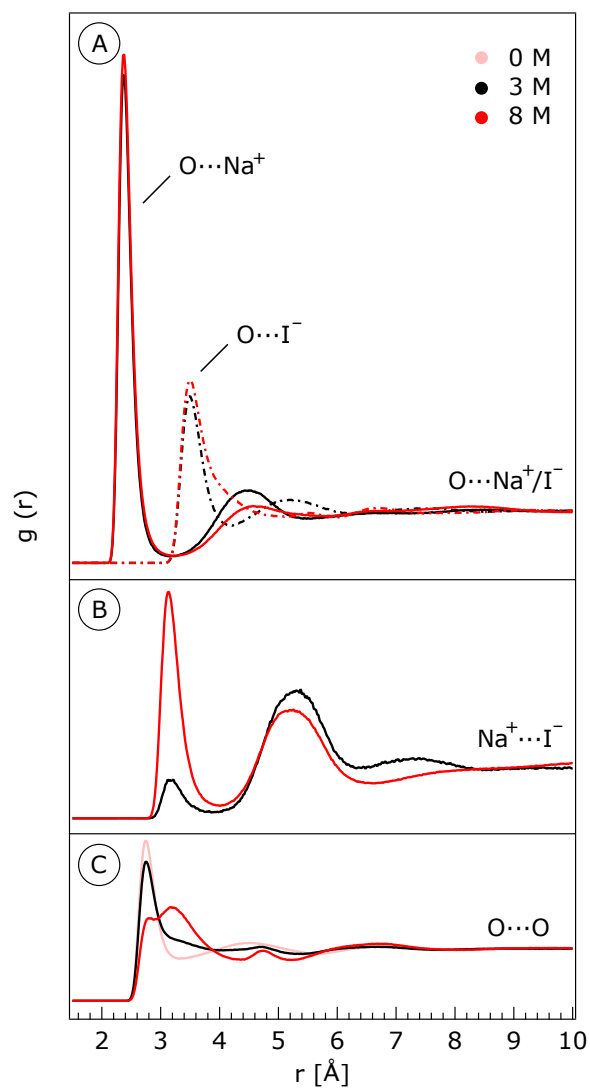


**Figure 4.7:** Radial-distribution functions for (panel A)  $\text{O}\cdots\text{Na}^+$  and  $\text{O}\cdots\text{I}^-$ , (panel B)  $\text{Na}^+\cdots\text{I}^-$  in 3 M and 8 M aqueous solutions of NaI, respectively. Panel C: Radial distribution functions for  $\text{O}\cdots\text{O}$  for pure water, 3 M and 8 M aqueous solutions of NaI. Figure reprinted from Ref<sup>182</sup>.

the first hydration shell. This, however, changes with higher concentration. For 8 M NaI solution, a randomly selected water molecule would typically have a sodium cation in its first solvation shell at a distance of 3.2 Å and one iodide within a distance of 4.5 Å. The same molecule has in average a second iodide in its first, and a third iodide in its second solvation shell. The MD simulations also reveal that the sodium cation integrates quite well into the tetrahedral structure. The average H–O...Na<sup>+</sup> angle is 120°, while 80% of the structures have a sodium cation and 100% an iodide in the first solvation shell. Iodine anions generally induce a larger structural change as the average O–H...I<sup>-</sup> angle is simulated to be 170°. The amount of tetrahedrally coordinated ions yields to 35% (sodium), 55% (iodide) and 20% (sodium and iodide).

We have seen from the MD calculations that, in particular for high concentrations, ionic solutes change the natural water structure considerably, which opens the question why the overall PE electron spectrum remains remarkably constant. To explore this, ionization energies (IE) have been inferred from the water pentamer, (H<sub>2</sub>O)<sub>5</sub>, for both, free molecules and embedded into a dielectric continuum. Furthermore, the three cases of the ions coordinated around the central water molecule have been simulated; (H<sub>2</sub>O)<sub>4</sub>I<sup>-</sup>, Na<sup>+</sup>(H<sub>2</sub>O)<sub>4</sub> and Na<sup>+</sup>(H<sub>2</sub>O)<sub>3</sub>I<sup>-</sup>. The results are presented in Figure 4.8A. The water orbitals 1b<sub>1</sub>, 3a<sub>1</sub> and 1b<sub>2</sub> have been evaluated. The IEs of all water molecules in the particular cluster are indicated by small horizontal lines. Consequently, the number of those line reduces to four (or three) when replacing one (or two) water molecules by ions. The solid circles represent the mean value of all individual IEs for the respective configuration and orbital. Vertical bars represent the total range of the individual IEs for all five (or four, or three) water molecules. Already for the pure water pentamer the range of IEs of all five water molecules is large; up to >2 eV. The central water molecule has generally the least variation in IE, because it is best stabilized by the surrounding water units. It is apparent that IEs change largely when adding ions into the clusters. For the configuration of sodium replacing one water monomer, Na<sup>+</sup>(H<sub>2</sub>O)<sub>4</sub>, the effect is strongest, providing a maximum energy shifts of up to 6.1 eV (for 3a<sub>1</sub>) to higher BEs. Replacing one outer water with iodide, (H<sub>2</sub>O)<sub>4</sub>I<sup>-</sup>, has the opposite effect, e.g., shifting the same orbital by 5.1 eV to lower BEs. The IE shifts reduce if both sodium and iodide are coordinated around a central water molecule and thus compensate their influence. Yet, the shifts are still large; up

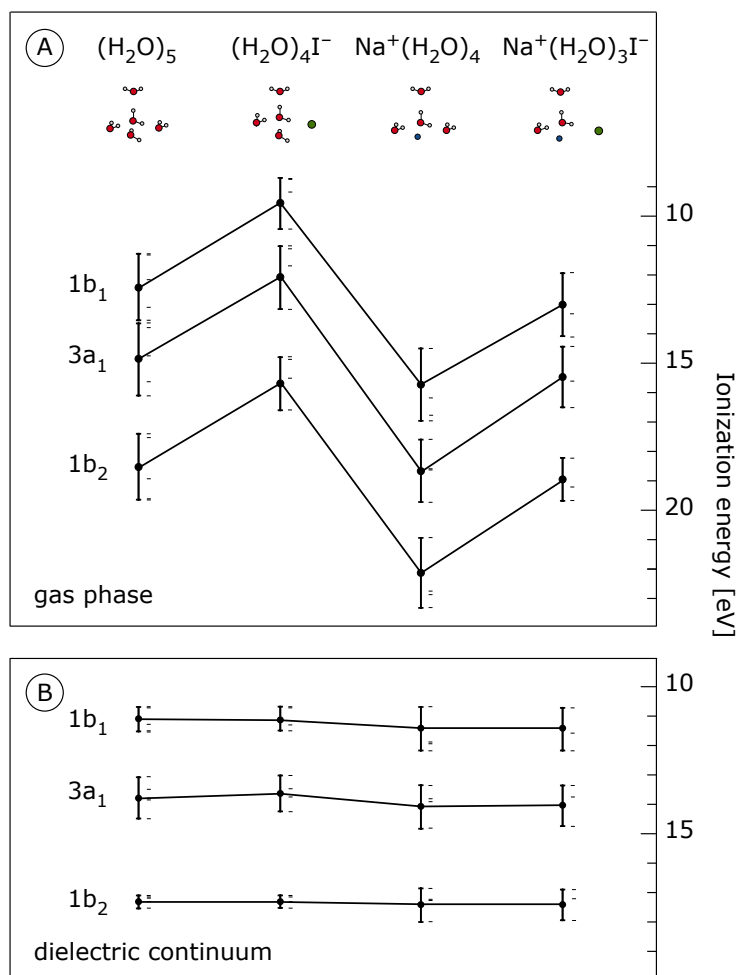


**Figure 4.8:** Calculated ionization energies (IE) from water pentamers in a model water cluster. Panel A: IEs of  $1b_1$ ,  $3a_1$  and  $1b_2$  orbitals are represented for four different configurations: Clusters of (i) five water molecules, (ii) four water molecules and iodide, (iii) four water molecules and sodium, and (iv) three water molecules, iodide and sodium. The O-I<sup>-</sup> distance is 3.6 Å and the O-Na<sup>+</sup> distance is 2.3 Å in all configurations. IEs for each water in the cluster were calculated, as indicated by small horizontal lines. The solid circles indicate the averaged value of the individual IEs for all water molecules for the respective coordination and orbital. Panel B: IEs of the same orbitals, but with the four cluster variants embedded into a dielectric continuum. Figure reprinted from Ref<sup>182</sup>.

to 2.9 eV when comparing the individual IEs. However, the averaged IEs are reasonably stable with shifts  $<0.8$  eV.

Embedding these clusters into a dielectric continuum reduces the changes drastically. The polarizable continuum model is a commonly used method in computational chemistry to model the solvation effects of dipolar solvents.<sup>234-236</sup> This model mimics the dielectric field induced by dipolar solvents rather than computing a large cluster of the solvent molecules. This reduces the computational costs significantly and makes *ab initio* computations feasible. The results are presented in Figure 4.8B. As can be seen in the figure, all three orbitals remain stable under varying ionic environment. The calculated averaged IE values for the water pentamer (11.5 eV for  $1b_1$ , 13.9 eV for  $3a_1$  and 17.3 eV for  $1b_2$ ;) are remarkably close to the experimentally observed binding energies, compare Figure 4.1. The case of both iodide and sodium around the central water molecule leaves the IEs rather unaffected; a maximum shift for the averaged IEs of  $<0.4$  eV is observed, which is on the order of the experimentally observed shifts. Furthermore, the range of the individual IE for a specific orbital and configuration is reduced, with a maximum range of 1.8 eV for the  $3a_1$  orbital in the  $\text{Na}^+(\text{H}_2\text{O})_4$  pentamer. This shows very well the ability of the dielectric continuum to shield intermolecular interactions. In general, the effect of the cation on the IEs is stronger than the anion. This is brought about by the closer distance between water and cation compared to water and anion, as can be seen in the RDFs in Figure 4.7.

The computations of micro-solvated clusters visualize the stabilizing effect of a dielectric continuum very well. The simulated IEs resemble the experimental values with  $<1.8$  eV deviation. However, the large range of possible individual IEs prevents us from exploring the reason for the experimental observations. In order to generate a more comprehensive picture the aforementioned total number of 500 clusters as extracted from MD simulations have been sampled. Simulations of 8 M NaI concentration were performed by putting  $\text{Na}^+$  and  $\text{I}^-$  always in the first solvation shell around the central water molecule. For 3 M concentration, however, both ions were allowed to exist at larger distance to the central monomer (solvent-shared). The simulated PE spectra are shown in Figure 4.9. We first focus on the neat water spectrum (0 M) at the bottom of Figure 4.9A. Calculated (red curves) and experimental (gray curves, taken from Figure 4.4) spectra are

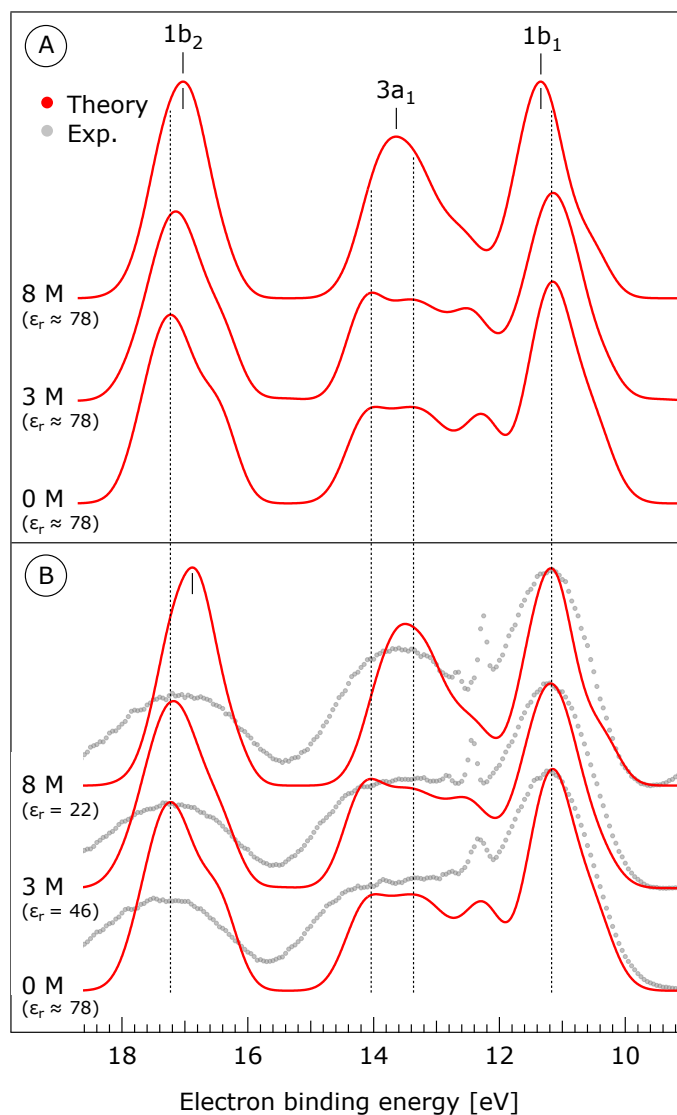


**Figure 4.9:** Theoretical photoemission spectra (red) resembling 0 M, 3 M and 8 M NaI in aqueous solution. Panel A: Simulations for water heptamer clusters containing one Na<sup>+</sup> and one I<sup>-</sup> ion embedded in a polarizable continuum having the permittivity 78.39 which corresponds to pure water. Panel B: Simulations for the same water clusters embedded in a polarizable continuum having the permittivity 46 for 3 M NaI and 22 for 8 M NaI solution. Experimental spectra (grey) are reprinted from Figure 4.4. Data for water correspond to water heptamers embedded in polarizable continuum having the permittivity 78.39 in both (A) and (B). The theoretical spectra are shifted to lower BEs by 0.3 eV so that those spectra representing neat water are aligned at 11.16 eV BE for the 1b<sub>1</sub> in accord to experimental data. Vertical dashed lines indicate the 1b<sub>1</sub>, 3a<sub>1</sub>L, 3a<sub>1</sub>H and 1b<sub>2</sub> energy positions, as inferred from the fittings in Figure 4.4. Figure reprinted from Ref<sup>182</sup>.

in very good agreement. All water valence peak energies overlap exactly. Even the flat-top structure of the  $3a_1$  peak is resembled. This is indicated by vertical dashed lines in Figure 4.9 which mark the  $1b_1$ ,  $3a_1H$ ,  $3a_1L$ , and  $1b_2$  energy positions inferred from the peak fittings. The calculated peaks are narrower which is due to the classical nature of the MD simulations used in the present study.<sup>177</sup> The dielectric constant of all three spectra was set to  $\epsilon_r = 78.39$  in order to mimic water. The  $3a_1$  loses its flat-top structure when going to 3 M and 8 M, similar to what we have seen in the experiment. On the other hand, both  $1b_1$  and  $1b_2$  experience an energy shift in opposite directions:  $1b_1$  ( $\sim 150$  meV) to higher BEs and  $1b_2$  ( $\sim 200$  meV) to lower BEs. The theoretical  $1b_1$  shift is in disagreement with our experimental observations, as argued above. In Figure 4.9B, we adjusted the model slightly by accounting for a change in the dielectric constant when replacing water with iodide and sodium. The small shift of the  $1b_1$  energy almost disappears once we apply  $\epsilon_r = 46$  for 3 M and  $\epsilon_r = 22$  for 8 M NaI in water. The small energy shift of the  $1b_2$  still remains. This result is in very good agreement with our experimental findings.

#### 4.4 WEAKENED INTERMOLECULAR INTERACTIONS

I want to emphasize that both experiment and computations show a remarkable stability with respect to increasing solute concentration. The observed shifts are relatively small ( $\leq 450$  meV) within a total concentration range of 7.95 M. In Figure 4.4 I have shown that for the 3 M NaI solution the  $1b_1$  peak aligns with neat water and the  $1b_2$  peak shifts by less than 100 meV to lower BEs compared to neat water. For the 8 M NaI solution, the  $1b_2$  peak shifts to lower BEs by  $\sim 370$  meV compared to neat water. This observation is explained in terms of stabilization of the non-bonding  $1b_1$  orbital by the sodium cation, and destabilization of the  $1b_2$  orbital by the iodine anion. The main effect from the electrolyte is caused by the sodium cation according to our calculations. The electrostatic interaction between the anion and the water is smaller since its coordination distance is larger. Upon increasing the ion–water distances, the energy shifts decrease. We make similar observations for the  $3a_1$  electrons. The  $3a_1$  spectral change, however, is explained by a weakening of the  $3a_1L$ – $3a_1H$  interaction between neighboring water molecules upon addition of the salt. Proton vibrations of the hydrogen-bond donor unit apparently modulate the electronic interaction, i.e., the interaction is different for different geometric



arrangements. When some of the associated water units are replaced by ions, the intermolecular bonding interaction is weakened, resulting in a narrowing of the  $1b_1$  and  $3a_1$  PE features. Thus, our findings show very well that disruption of the hydrogen bonds in water that mediate intermolecular interactions has a considerable effect on the electronic structure of water.

Adding high concentrations of solutes to water reduces intermolecular interactions up to a point where the individual water units can be considered as separated, yet embedded in a dielectric continuum. This effect is the most robust manifestation of ionic influence on the electronic and molecular structure of liquid water. Altered intermolecular interactions in water with increasing salt concentration have also been observed in other spectroscopies. Studies using techniques such as infrared<sup>237</sup>, (low-frequency) Raman<sup>238–241</sup>, time-resolved Kerr effect<sup>242</sup> and dielectric relaxation<sup>243,244</sup> show evidence for partial breaking of the water hydrogen-bond structure<sup>190</sup> and the formation of solvation shells around the ions. These studies draw similar conclusions, that the main structural change is connected to the first solvation shell and the effect is small beyond the solvation shell. Recent studies utilizing infrared spectroscopy on water nanodroplets containing either  $\text{Na}^+$  or  $\text{I}^-$ ,<sup>245</sup> and resonant X-ray emission on hydrated  $\text{MgCl}_2$ <sup>200</sup> also support this conclusion.

The finding that the large molecular structure change, i.e., the transformation from the dilute aqueous solution to the viscous phase, has so little effect on the PE spectra is clearly surprising. Both the PE spectroscopy experiments and theoretical calculations show that the solute and solvent peak positions in the PE spectra are surprisingly stable with respect to increasing electrolyte concentrations. One important consequence from an experimental and practical viewpoint is that the present results fully justify the common procedure of aligning liquid-jet PE spectra from aqueous solutions using the well-resolved liquid water  $1b_1$  peak. The relative energetics of the solute peaks – that are energetically-referenced to the  $1b_1$  peak – are found to be insensitive to ion concentration. This behavior may surprise in the light of the X-ray PE spectroscopy technique's high sensitivity to a local atomic (chemical) environment which can lead to core-level (chemical) energy shifts of several electron volts.<sup>27,75,246</sup> The insensitivity of the present spectra points toward the impressive screening ability of polar liquids and the more delo-

calized nature of the valence electrons on which we focus here. The experimental results presented indicate that aqueous-phase valence electron BEs are quite insensitive to purely electrostatic interactions between molecules over a wide range of concentrations. We can contrast this result with autoionization electron energetics that have been shown to be much more sensitive to intermolecular interaction.<sup>122,127</sup> The next chapters of this thesis deal with autoionization spectroscopy as an approach to acquire information on local solvation, ion pairing and nuclear dynamics upon core-level photoionization.

# 5

## Autoionization from Aqueous Systems

In the previous chapter I demonstrated how photoionization from liquid water creates photoelectrons with KEs directly related to the occupied electronic structure of water. As core-level photoionization results in an excited state, the system relaxes within a few fs, i.e., approximately 4 fs for O 1s and 6.4 fs for N 1s vacancies.<sup>96,97</sup> The excess energy (some hundred eV) upon core-level de-excitation can trigger a multitude of processes. In the current chapter I focus on non-radiative relaxation processes that occur upon ionization of the oxygen 1s orbitals of water and other hydrogen-bonded systems (and later nitrogen 1s for NH<sub>3</sub> and NH<sub>4</sub><sup>+</sup>). Before proceeding, it is relevant to first clarify the terminology of the current chapter. The term ‘water Auger’ electrons, refers to Auger electrons released from the water molecule upon ionization of the O 1s level. The O 1s BE of liquid water is 538.1 eV.<sup>247</sup> Liquid phase water valence binding energies range from 11.2 eV to 31.2 eV. Thus, based on Equation (2.3), water Auger electrons have KEs between 515.7 eV and 475.7 eV. This is however only a rough estimate that neglects binding energy lowering of the double-ionized final state due to polarization screening which has been shown to cause KE shifts of several electronvolts. The magnitude of the polarization screening shift scales with the square of the charge, so doubly charged final states with the two holes localized on the same molecule will be shifted down even further.<sup>248</sup> The spectral range in

which Auger electrons appear will be called autoionization spectrum because also ICD electrons contribute to this KE region. In this chapter I start by introducing previous discoveries on ICD in liquid  $\text{H}_2\text{O}$ ,  $\text{NH}_3$  (aq) and  $\text{H}_2\text{O}_2$  (aq) before I move on to recent results on  $\text{NH}_4^+$  (aq).

### 5.1 CORE-LEVEL ICD IN AQUEOUS SOLUTIONS

A typical autoionization spectrum of gas phase water recorded at 600 eV photon energy is presented in the top tier of Figure 5.1. The intensity onset is around 507 eV KE with the leading local Auger peak at  $\sim 503$  eV KE. The leading 2h state (indicated by a dashed

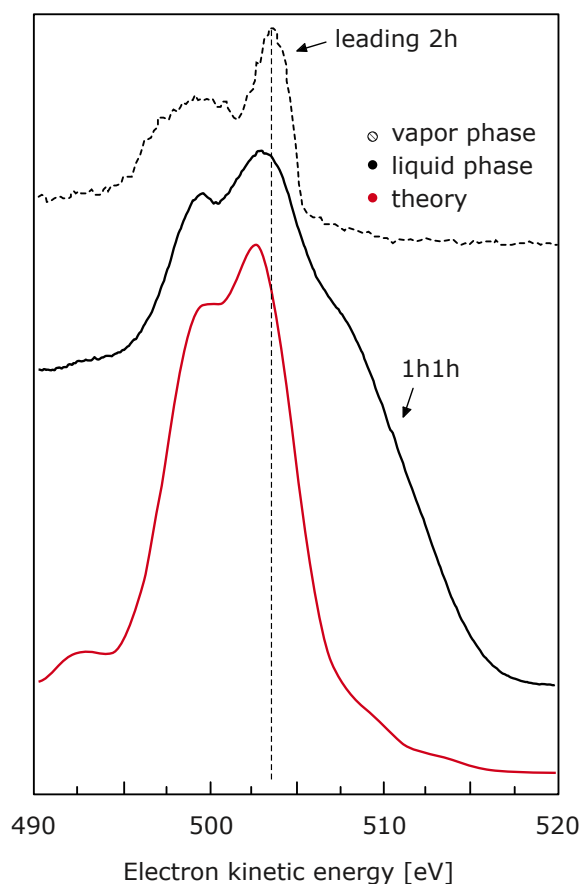


**Figure 5.1:** Oxygen 1s autoionization electron spectra from water in the gas phase and liquid phase. The experimental spectra were measured at 600 eV photon energy. In the gas phase local Auger processes occur solely resulting in 2h states, whereas additional intensity on the high-energy side in the liquid phase spectrum is an indication of non-local 1h1h states. The leading 2h state is indicated by a dashed line. Figure adapted from Ref<sup>249</sup>.

line) is due to  $1s-1b_11b_1$  Auger decay. The middle spectrum shows the analogous liquid water spectrum which exhibits more extended features. This is due to the fact that this spectrum is a combination of liquid and gas phase water. The spectrum has been aligned for a 4.5 eV gas-to-liquid-phase energy shift arising from liquid water's electronic polarization. The most remarkable part in the liquid phase spectrum is the broad new signal at  $>505$  eV KE. This is solely liquid phase contribution and the gas phase autoionization spectrum does not exhibit similar features. We already know that the gas-liquid BE shift of valence and core level is rather similar, i.e.,  $\sim 0.4$  eV difference (1.8 eV for O 1s and 1.4 eV for  $1b_1$ ). This implies, according to Equation (2.3), that liquid phase 2h Auger states are shifted by approximately 0.8 eV ( $2 \times 0.4$  eV) compared to gas phase. Yet, the high-energy shoulder extends up to 10 eV higher KEs (505–515 eV KE). This is an unequivocal signature of 1h1h final states of liquid water and thus a clear indication of charge migration within the 4-fs lifetime of the water O 1s core-hole. Whether this is mediated by nuclear motion or electron transfer (or both) is not directly clear from this measurement alone. In the gas phase, autoionization is considered as purely electronic and local, because gas molecules do not interact with each other. However, none of the above assumptions are justified in condensed-phase systems, characterized by bonding interactions between the constituting monomers (hydrogen bonds in liquid water). Here, nuclear dynamics can contribute to the relaxation of core-ionized states.

## 5.2 PROTON TRANSFER IN WATER

The next step was to explore whether charge separation in liquid water (occurrence of 1h1h states), which is absent in gas phase water (only 2h states), results from nuclear or purely electronic processes. In the following, I will discuss the effect of nuclear dynamics on an autoionization spectrum. A full O–H stretch vibration ( $\sim 10$  fs<sup>100</sup>) proceeds on the same timescale as autoionization from water O 1s ( $\sim 4$  fs), as described in Section 2.2.1. Thus, nuclear motion can principally be traced by means of ICD/ETMD spectroscopy.<sup>97</sup> In order to determine autoionization spectral changes resulting from nuclear rearrangement in more detail, theoretical simulations have been performed by quantum chemical methods.<sup>249</sup> Figure 5.2 shows simulated autoionization spectra for three explicit geometries of the water pentamer (as depicted), representing structural changes

upon proton dynamics. Results are shown for the O–H proton-transfer coordinates 0.95 Å (ground-state geometry, Panel A), 1.40 Å (referred to as ‘Zundel-like’ structure<sup>250</sup>, Panel B), and 1.85 Å (water–hydronium complex, Panel C). The areas under the black, red, and blue curves reflect the contributions of the local Auger, ICD, and ETMD processes, respectively, to the total spectral intensity according to the calculations. As intuitively expected, local relaxation (resulting in 2h final states) is the by far dominant channel for the ground-state nuclear geometry (but excited state electronic configuration), while ICD and ETMD have only minor contribution to the spectrum in this geometry. The probability for non-local decay pathways increases dramatically when one proton of the central water monomer is shared with a neighboring water monomer, resulting in a transient Zundel-like structure,  $\text{OH}\cdots\text{H}^+\cdots\text{H}_2\text{O}$ .<sup>97,251–255</sup> In this case it is seen that 1h1h final states resulting from ICD (i.e.,  $\text{OH}\cdots\text{H}^+\cdots\text{H}_2\text{O}^+$ ) are as probable as 2h final states resulting from normal Auger (i.e.,  $\text{OH}^+\cdots\text{H}^+\cdots\text{H}_2\text{O}$ ).<sup>249</sup> The same holds for the probability of ETMD which can create both 2h and 1h1h final states:  $\text{OH}^-\cdots\text{H}^+\cdots\text{H}_2\text{O}^{2+}$  for ETMD(2) and  $\text{OH}^-\cdots\text{H}^+\cdots\text{H}_2\text{O}^+\cdots\text{H}_2\text{O}^+$  for ETMD(3). These results indicate that a possible proton transfer would increase the probability of ICD and ETMD significantly if the proton migration is significant enough within the fs time window. For example, a recent study has demonstrated a 10-fold enhancement of the ICD efficiency for proton-transferred geometries in ammonia clusters as compared to the ground state geometry.<sup>249,256</sup> Note that the additional signal from 1h1h final states would shift the total spectrum (gray shaded area) to higher KEs, which is consistent with our experimental observation, compare Figure 5.1. This is due to reduced Coulombic interaction for separated charges as explained in Section 2.2.3. The local Auger electrons also shift to higher KEs as a function of nuclear coordinate, however not to the same extent.

In summary, we can see that the probability of charge-separated final states (1h1h) compared to localized final states (2h) increases significantly with increasing proton distance; an effect named proton-transfer mediated charge separation (PTM-CS).<sup>36,249</sup> Consequently, if PTM-CS supports non-local decay processes, systems with slower proton mobility should show a lower abundance of 1h1h final states. To test this assumption, an autoionization spectrum of heavy water ( $\text{D}_2\text{O}$ ) in comparison with normal water ( $\text{H}_2\text{O}$ ) has been measured and compared in Figure 5.3. The normal water spectrum (black curve)

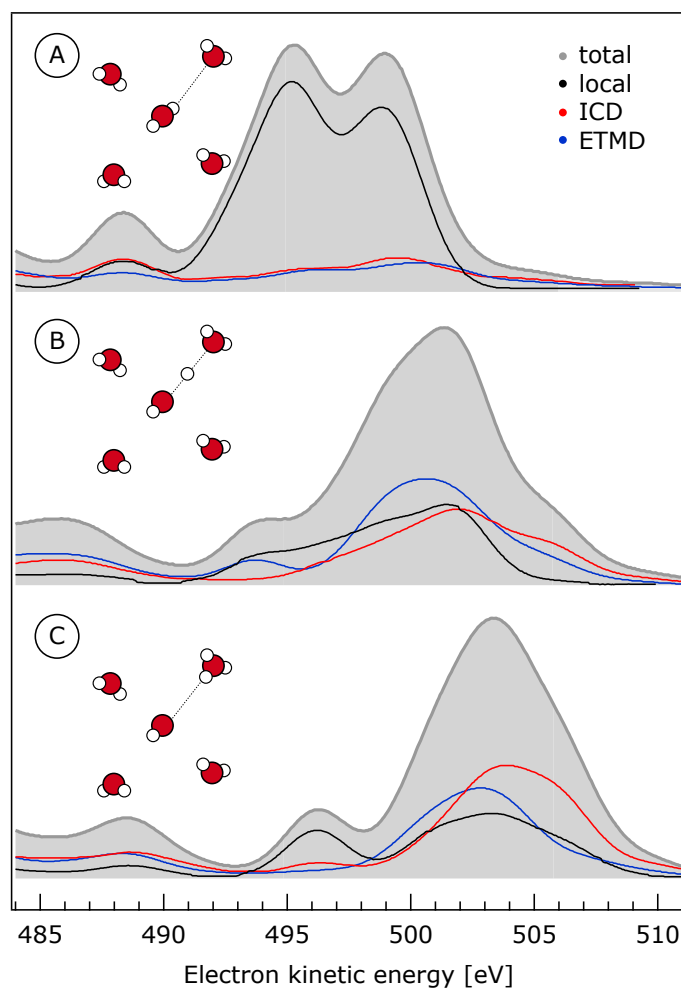


**Figure 5.2:** Simulated autoionization spectra of water pentamers in the three coordinations: With a proton from the central monomer detached at a distance of 1.85 Å (Panel C), and 1.40 Å (Panel B). Panel A represents ground-state configuration. For all three configurations the contributions of Auger decay (black), ICD (red) and ETMD (blue) have been simulated. The gray curve represents the resulting total autoionization spectrum. Figure adapted from Ref<sup>249</sup>.

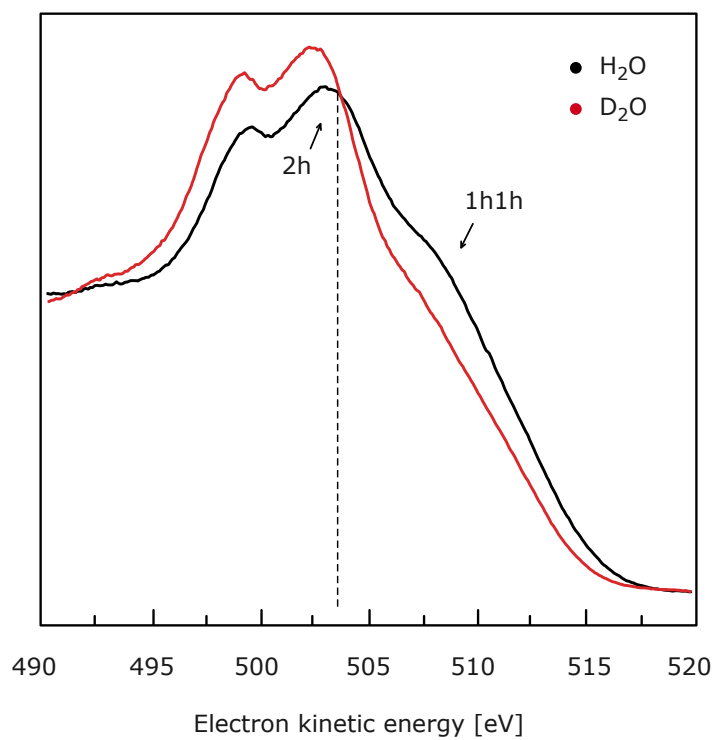


**Figure 5.3:** Oxygen 1s autoionization spectra from normal (black) and heavy (red) liquid water. The experimental spectra were measured at 600 eV photon energy. Figure adapted from Ref<sup>249</sup>.



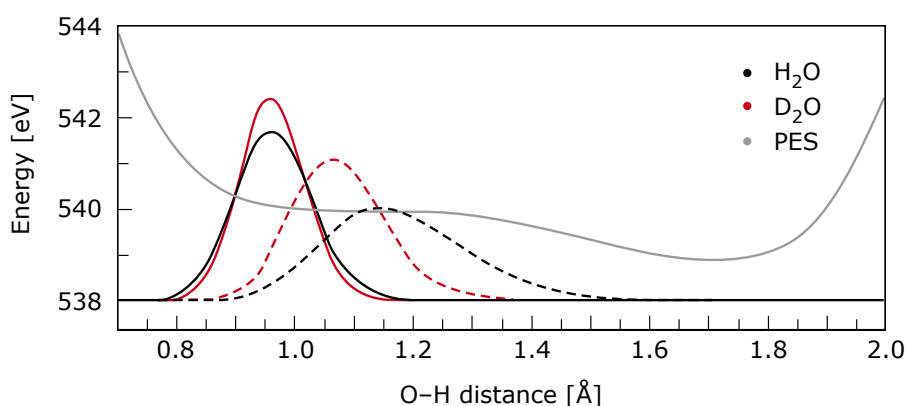


**Figure 5.4:** The O 1s ionized lowest potential-energy surface (PES, gray line) along the O–H coordinate for H<sub>2</sub>O/D<sub>2</sub>O as inferred from quantum chemical calculations. The ground-state O–H distance before ionization is at 0.95 Å. Upon ionization, an energy minimum at 1.75 Å implies a complete proton transfer. The time frame of only 4 fs (core-hole lifetime) limits the wave packets to a mean distance of only 1.15 Å and 1.05 Å for H<sub>2</sub>O (black dashed line) and D<sub>2</sub>O (red dashed line), respectively. Figure adapted from Ref<sup>249</sup>.

is the same as in Figure 5.1. The striking difference between the normal and the heavy isotope spectra is found in the high-KE shoulder of the spectrum, which has been argued to result from the differences in the decay rates forming 1h1h final states. However, the spectral intensity in the high-KE region is less strong for the deuterated form of water as compared to the spectrum of normal water. This is a clear indication for a kinetic isotope effect (i.e., the involvement of nuclear motion). Since deuterium is heavier than hydrogen, the O–D stretch frequency as well as the deuteron-transfer dynamics is slowed down compared to that of normal hydrogen.<sup>257</sup>

Quantum dynamical calculations<sup>36</sup> of the O 1s core-ionized lowest potential-energy surface (PES) associated with O–H stretching of the water dimer, shown in Figure 5.4, support this interpretation. The O–H stretch mode is identified as the most important proton-transfer coordinate (as explained earlier) and the chosen dimer geometry corresponds to the structure of condensed-phase water (I<sub>h</sub> ice) with an O–O distance of 2.7 Å.<sup>39</sup> The core-ionized PES of the water and D<sub>2</sub>O dimers indicates that dissociation is energetically feasible, featuring a minimum at 1.75 Å for both isotopes (gray curve in Figure 5.4). At that distance the proton/deuteron is fully detached, creating OH<sup>+</sup>...H<sub>3</sub>O<sup>+</sup> (or the respective deuterated forms). However, the PES is rather flat and the driving force for this reaction is not strong and thus not likely to complete within the lifetime of the

core-ionized state. This can be seen when comparing the calculated wave packets (squared wave functions) of the ionized water dimer in the ground-state geometry and the structure that evolves after 4 fs, when the average O–H distance has increased. The wave packets overlap at  $t = 0$  (ground-state geometry before ionization) and diverge after 4 fs. In the ground state (before ionization) the O–H distance is 0.95 Å for both normal and heavy water as indicated by black (H<sub>2</sub>O) and red (D<sub>2</sub>O) solid lines in Figure 5.4. After 4 fs the wave packet for normal water has its center at 1.15 Å and reaches out to a maximum of 1.6 Å (black dashed line). In contrast to that, the wave packet of D<sub>2</sub>O (black dashed line) does not evolve as far, with a center at 1.05 Å extending to a maximum distance of 1.35 Å. These calculations demonstrate the weaker nuclear dynamics in heavy water as compare to normal water and thus explain, based in the findings from Figure 5.2, the attenuated creation of 1h1h final states in D<sub>2</sub>O upon O 1s ionization.

Both, calculations on small clusters and measurements on two water isotopes suggest that PTM-CS strongly enhances non-local decay pathways. As an overview, the full PTM-CS process in water with its possible decay channels is sketched in Figure 5.5. Starting from the ground-state dimeric structure, H<sub>2</sub>O...H<sub>2</sub>O, a positive charge is created at one water site upon O 1s ionization. The electronically excited state induces a proton transfer along the hydrogen-bond axis, which results in an excited singly charged Zundel-like structure, \*OH...H<sup>+</sup>...H<sub>2</sub>O. The asterisk indicates a neutral but excited molecule. Autoionization – be it of Auger, ETMD or ICD nature – of the excited Zundel-like system occurs within 4 fs. Different non-radiative decay processes are possible, of which Figure 5.5 only sketches the most important. The PTM-Augere decay, i.e., Auger decay of a transient proton-transferred geometry, results in an OH<sup>+</sup>...H<sup>+</sup>...H<sub>2</sub>O final state (left branch in Figure 5.5). The ultimate configuration is H<sub>2</sub>O<sup>2+</sup>...H<sub>2</sub>O. Alternatively, the positively charged parent water molecule repels the proton, which finally creates OH<sup>+</sup>...H<sub>3</sub>O<sup>+</sup>. However, this complete proton transfer happens slower than the 4-fs time span and has thus no influence on the outgoing Auger electron and cannot be detected by means of PE spectroscopy. Another decay channel, PTM-ICD creates an OH...H<sup>+</sup>...H<sub>2</sub>O<sup>+</sup> final state, with charges already spatially separated after 4 fs (middle branch in Figure 5.5). Coulombic repulsion will push the hydrogen to its original position, ending up with H<sub>2</sub>O<sup>+</sup>...H<sub>2</sub>O<sup>+</sup>. The last shown example (right branch in Fig-

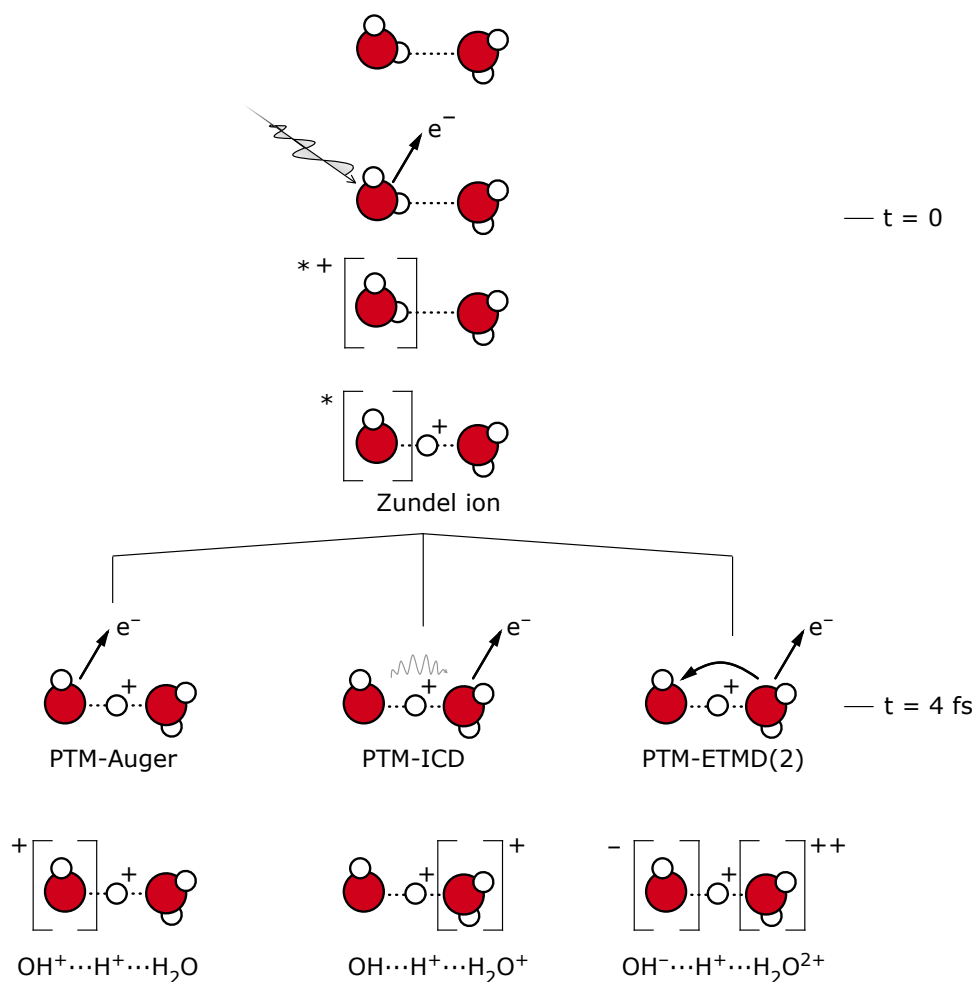


**Figure 5.5:** Sketch of PTM-CS processes upon O 1s ionization of a water dimer. Water oxygen atoms are represented by red circles and hydrogen atoms by white circles. Proton transfer along the hydrogen bond axis creates an intermediate Zundel-like ionic state. Electronic relaxation occurs either local, via Auger decay, or non-local, via ICD and ETMD. Only one possible ETMD channel is shown in this schematic, ETMD(2). ETMD(3) is a fourth possible decay channel for water clusters bigger than two. Final charge states after 4 fs are indicated at the bottom. Further (slow) charge migration caused by Coulombic interaction of the charged species is outside the measurable capabilities of PE spectroscopy and thus neglected in this picture.

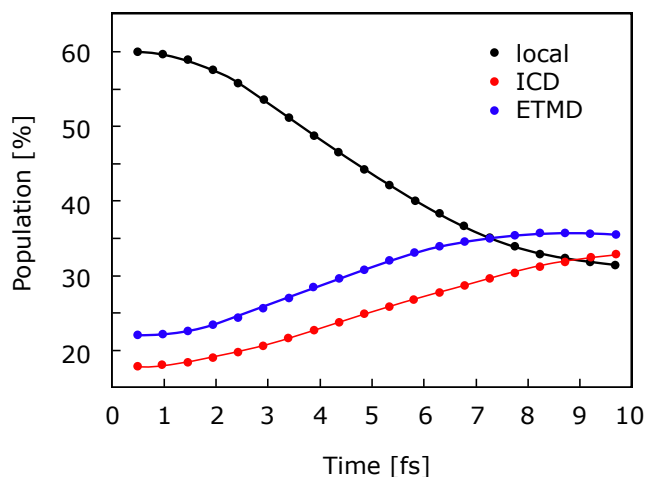


**Figure 5.6:** Populations of the final states by different competing electronic relaxation processes in the model water pentamer computed for different time instants. At 4 fs the population of ETMD and ICD final states amounts to 25% and 20% respectively. The populations were obtained by determining the areas of the respective contributions to the total spectral intensities of the spectra in Figure 5.2. Figure reprinted from Ref<sup>249</sup>.

ure 5.5) is PTM-ETMD(2), which ends up in a  $\text{OH}^- \cdots \text{H}^+ \cdots \text{H}_2\text{O}^{2+}$  final structure. We see from Figure 5.5 that the final products of autoionization are diverse. Water dications are mainly produced by Auger decay, while pairs of water cations are produced by ICD and ETMD. So-called PTM fragments ( $\text{OH}^+$ ,  $\text{OH}^-$ ,  $\text{H}_3\text{O}^+$ , etc.) are produced by all PTM-autoionization processes which occur for geometries along the proton transfer coordinate with O–H distances larger than 1.4 Å.

The total populations of the Auger, ICD, and ETMD final states have been calculated for different times after ionization, see Figure 5.6. At 4 fs, 2h final states created by Auger decay – be it ground-state or proton-transferred – amount to 45%. Charge separated 1h1h final states amount to 25%; 20% created by ICD and 5% by ETMD. Figure 5.6 also illustrates very well the enhancement of charge-separated 1h1h final states at later times. It is non-trivial though to disentangle PTM-Auger and PTM-ICD in an experiment since they both contribute to the autoionization spectrum with similar KEs. Yet, the combined study of autoionization spectroscopy of different isotopes and quantum chemical calculations provide a clear indication for enhanced population of non-local 1h1h final states by nuclear dynamics. As a consequence, it seems reasonable to assume that non-local autoionization is both, a general phenomenon for hydrogen-bonded systems and in

principle scales with the strength of the intermolecular interactions. In the next section, I will show that non-local relaxation, in particular ICD, is well observable in other aqueous systems and ICD spectroscopy can be used as a probe for hydrogen-bond strength.

### 5.3 PROTON TRANSFER IN OTHER AQUEOUS SYSTEMS

Autoionization spectra from other hydrogen-bonded systems of distinctly different hydration configurations have been studied:  $\text{H}_2\text{O}_2$  (aq)<sup>258</sup>,  $\text{NH}_3$  (aq)<sup>259</sup> and their deuterated analogues. The aim was to investigate (i) if PTM-CS associated non-local decay is a general phenomenon for hydrogen-bonded systems, (ii) how the strength of intermolecular interaction affects non-local decay rates, and (iii) if these processes can be exploited to gain information on liquid-state structure. Hydrogen peroxide,  $\text{H}_2\text{O}_2$ , was chosen because it can be considered a complex analog to water, as  $\text{H}_2\text{O}_2$  and water exhibit equally strong hydrogen bonds. On the basis of the findings for liquid water, our expectation is that nuclear dynamics is more probable the stronger the intermolecular hydrogen bonds are. Ammonium,  $\text{NH}_3$ , in aqueous solution has a weaker hydrogen bond interaction with water than the water–water hydrogen bonds.  $\text{NH}_3$  was chosen as a good comparative model system due to its isoelectronic structure with water and its biological relevance, as it resembles the amino group found in many biomolecules such as proteins. For  $\text{NH}_3$ , the proton transfer is expected to occur along the hydrogen bond donor coordinate,  $\text{N}-\text{H}\cdots\text{O}$ . A third, and important reason for choosing ammonia is that the BE of nitrogen 1s lies around 400 eV<sup>260</sup>, well below oxygen 1s (around 538.1 eV BE<sup>247</sup>) which limits possible decay channels upon N 1s ionization significantly. The nitrogen 1s core-hole lifetime (6.4 fs) is on the same order as for oxygen (4 fs).<sup>96,97</sup>

Figure 5.7 presents molecule geometries corresponding to hydrogen-bonding arrangements with densities obtained from MD simulations at 300 K for a solute in a water box. Further details regarding the simulation program are found in Refs<sup>262–264</sup>. A hydrogen bond is considered as particular strong if two conditions are fulfilled. First, the distance between proton donor and acceptor (O–O or N–O) must be smaller than 3.2 Å, and second the hydrogen bond must be somewhat collinear to the covalent bond,  $\text{N/O}-\text{H}\cdots\text{O} = 180^\circ \pm 60^\circ$ . Molecular arrangements that fit these requirements are indicated by a gray rectangle in Figure 5.7. This area comprises most data points from liquid

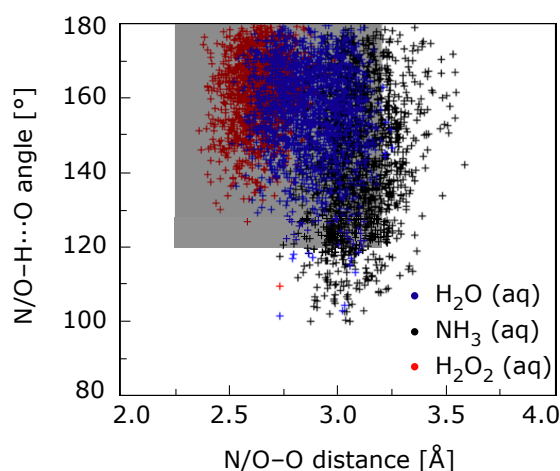
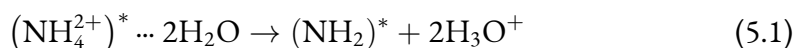


**Figure 5.7:** Density plot along two coordinates characterizing hydrogen-bond strengths in water, ammonia (aq) and hydrogen peroxide (aq). X-axis: The distance between the oxygen or nitrogen, for water (blue), hydrogen peroxide (red) and ammonia (black) respectively. Y-axis: Angle between the heavy atom (oxygen or nitrogen) and the oxygen of a neighboring water molecule. The gray area indicates geometries corresponding to strong hydrogen-bonding. Figure reprinted from Ref<sup>261</sup>.

$\text{H}_2\text{O}$  and  $\text{H}_2\text{O}_2$  (aq), but not from  $\text{NH}_3$  (aq) which indicates that ammonia tends to form on average weaker hydrogen bonds. PTM-CS is anticipated to be less likely here. The trend in hydrogen-bond strengths follows  $\text{H}_2\text{O}_2$  (aq) >  $\text{H}_2\text{O}$  >  $\text{NH}_3$  (aq). PTM-CS has been shown to scale the same way, however in the case of  $\text{H}_2\text{O}_2$  (aq) experimental validation of strong nuclear dynamics could not unequivocally be demonstrated because of competing intramolecular de-excitation. Also, unlike in water, for  $\text{H}_2\text{O}_2$  (aq) the dicationic final states (2h) have energies very similar to the states that correspond to delocalization of the two charges across the  $\text{H}_2\text{O}_2$  molecule (1h1h). Nonetheless, it has been shown that the probability of PTM-CS is a general phenomenon in hydrogen-bonded systems and strongly correlates with hydrogen-bond strength, which naturally makes this particular spectral fingerprint (the high energy part of the autoionization spectrum) a rather sensitive probe of hydration structure. My next step is to explore the effect of charge and addition of a further hydrogen bond. The systems under investigation are  $\text{NH}_4^+$  (aq) and  $\text{ND}_4^+$  (aq).

#### 5.4 PROTON DYNAMICS IN AQUEOUS AMMONIUM

Based on the findings that PTM-CS correlates with hydrogen-bond strength, a large effect was expected when going from neutral to cationic molecules. The results presented in this chapter have been published in Ref<sup>265</sup>. Ammonium,  $\text{NH}_4^+$ , in aqueous solution is an ideal case, as it forms stronger hydrogen bonds with water than does neutral  $\text{NH}_3$ ,  $\text{H}_2\text{O}$  or  $\text{H}_2\text{O}_2$ .<sup>259,266</sup> The positive charge of  $\text{NH}_4^+$  induces a strong dipole interaction with water already in the ground-state. Another effect of the positive charge is stronger repulsion of a proton from the parent cation when compared to neutral  $\text{NH}_3$ . Furthermore, we expect that one additional hydrogen compared to  $\text{NH}_3$  increases the coordination number and thus the probability for a proton transfer. Lastly, core ionization of the ammonium cation creates an excited, doubly charged cation,  $(\text{NH}_4^{2+})^*$ , which is suspected to enable a possible double-proton transfer:



Inferred from these considerations and based on our observations from the previous studies a strong PTM-CS and thus ICD effect is expected for ammonium in aqueous phase. The investigation of relaxation processes in  $\text{NH}_4^+$  (aq) is an important prerequisite for understanding radiation induced damage in biological relevant molecules, as amino acids and proteins.

Again, the first step is characterizing the hydrogen-bond strength of  $\text{NH}_4^+ \cdots \text{H}_2\text{O}$  and compare it with the aforementioned aqueous solutes. The stronger interaction of ammonium with water can be already inferred from a computational analysis of the molecular dimers; the  $\text{NH}_4^+ \cdots \text{H}_2\text{O}$  complex is stabilized by 87 kJ/mol, which is much stronger compared to the  $\text{NH}_3 \cdots \text{H}_2\text{O}$  (10 kJ/mol) and the  $\text{H}_2\text{O} \cdots \text{H}_2\text{O}$  (21 kJ/mol) complexes. The bond strengths correlate with the intermolecular distances between the heavy atoms (N/O and O) contributing to the hydrogen bonds in the dimers:  $\sim 2.67$  Å bond length for ammonium,  $\sim 2.9$  Å for water, and  $\sim 3.24$  Å for ammonia. Similar to the previous studies, the hydrogen-bond strengths of aqueous solutes are determined more accurately by their geometrical configuration, which was approached by *ab initio* MD simulations in thermal equilibrium. Simulations have been performed by the Slavíček group and fur-

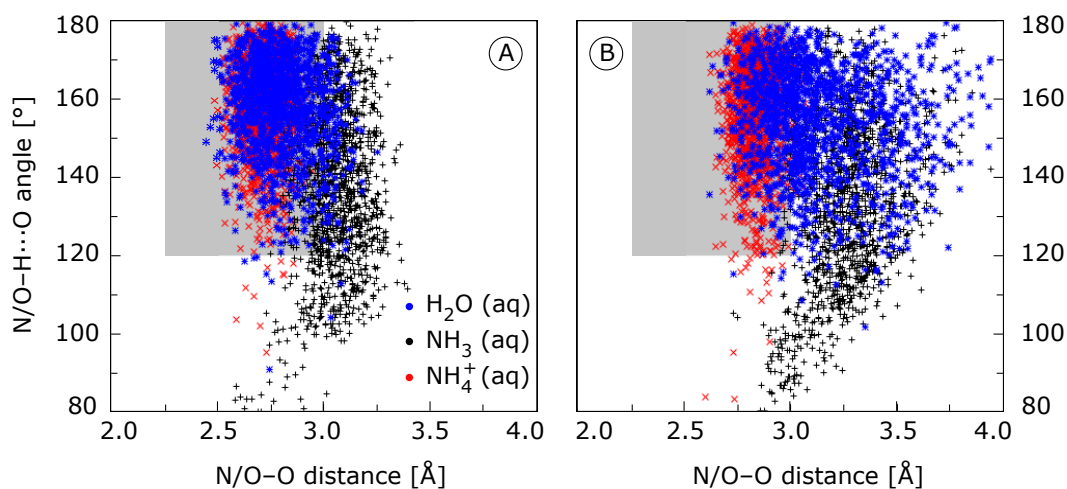


**Figure 5.8:** Density plot along two coordinates characterizing hydrogen-bond strengths in water, ammonia (aq) and ammonium (aq). X-axis: The distance between the oxygen or nitrogen, for water (blue), ammonia (black) and ammonium (red), respectively. Y-axis: Angle between the heavy atom (oxygen or nitrogen) and the oxygen of a neighboring water molecule. The gray area indicates geometries corresponding to strong hydrogen-bonding. Panel A represents the strongest hydrogen bond and panel B the second strongest. Figure reprinted from Ref<sup>265</sup>.

Further details regarding the programs and parameters are found in Refs<sup>262-265</sup>. The particularly strong hydrogen bond network of ammonium is presented in Figure 5.8, from which we infer similar hydrogen bond lengths (2.5–3.0 Å) and angles (120°–180°) for the strongest hydrogen bond of  $\text{NH}_4^+$  than for water.  $\text{NH}_3$  (2.8–3.3 Å and 100°–180°) has the same values as in Figure 5.7, essentially outside the region of strong hydrogen bonding. The ammonium cation can potentially form four hydrogen-donor bonds and the simulated average coordination number is 3.3. This motivated us to also analyze the second-strongest hydrogen bond, which turned out to also be in the region of strong bonding. This finding of a second strong hydrogen bond aligns with our idea of a two-proton transfer upon core ionization. According to the average coordination number we computed the energetics of the micro-solvated  $\text{NH}_4^+(\text{H}_2\text{O})_3$  cluster upon core ionization. The computed 2-dimensional lowest PES associated with two N–H transfer coordinates upon N 1s core-ionization is shown in Figure 5.9. Details regarding the geometry optimization and construction of the PES are found in Refs<sup>267-271</sup>. The PES has a negative slope with an energy minimum at  $\sim 1.8$  Å for the N–H distance along both coordinates, along the strongest and the second strongest hydrogen bond. The N–H distance of 1.8 Å corresponds to a complete proton transfer, forming  $\text{H}_3\text{O}^+$ . The steep negative slope of



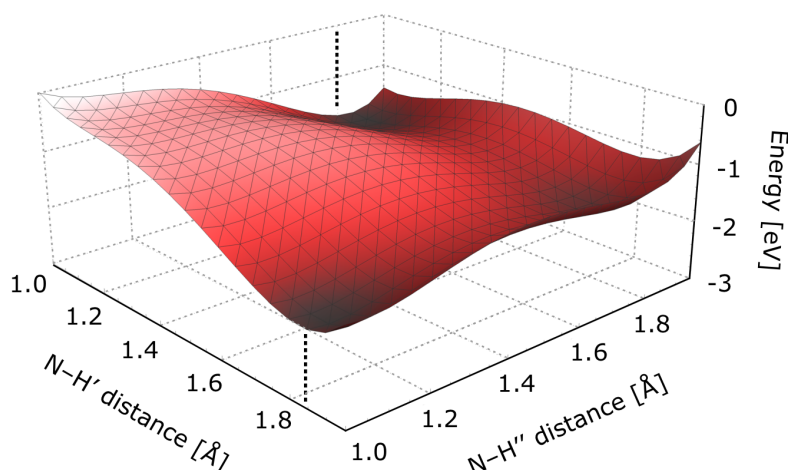


**Figure 5.9:** Two-dimensional cut through the excited-state potential-energy surface of a core-ionized  $\text{NH}_4^+(\text{H}_2\text{O})_3$  cluster, representing the electronic energy as a function of the N–H distances along the direction of two hydrogen bonds. The N–H ground state distance (before excitation) is at 1.0 Å. The minimum energy corresponding to the fully transferred proton is at  $\sim 1.8$  Å for both the strongest (H') and the second-strongest (H'') hydrogen bond, as marked by black dotted lines. The global minimum of the energy surface is for both protons fully transferred. Figure adapted from Ref<sup>265</sup>.

the surface indicates that a double-proton transfer is energetically favorable. Yet, the pure energetics do not tell whether these dynamics actually happen within the ultra-short time window of 6.4 fs. Dynamical calculations on the N 1s core-ionized state for a large number of hydrated ammonium clusters,  $\text{NH}_4^+(\text{H}_2\text{O})_{20}$ , are presented in Figure 5.10, where proton density is plotted as a function of N–H/D distance for two protons at  $t = 0$  and  $t = 7$  fs. Figure 5.10A presents the case of normal ammonium whereas Figure 5.10B is for the deuterated form. Both, normal and deuterated form have the same ground state ( $t = 0$ ) N–H/D distance of  $\sim 1.0$  Å. We observe a considerable migration of proton 1 and 2 within the 7 fs for both normal and deuterated species. In the non-deuterated case the density distribution of the strongest hydrogen-bonded proton reaches out to 2.1 Å N–H distance after 7 fs with a center at 1.8 Å. Remember that 1.8 Å is the energetic minimum and corresponds to a proton fully transferred, creating ammonia and hydronium cation. The density distribution of the second proton after 7 fs reaches out to 1.9 Å with a center at 1.4 Å which is almost half the way between its parent  $\text{NH}_4^+$  molecule and the coordinated water monomer. The deuterated picture in Figure 5.10B shows similar dynamics but slowed down as expected. The center of the proton density plot of the

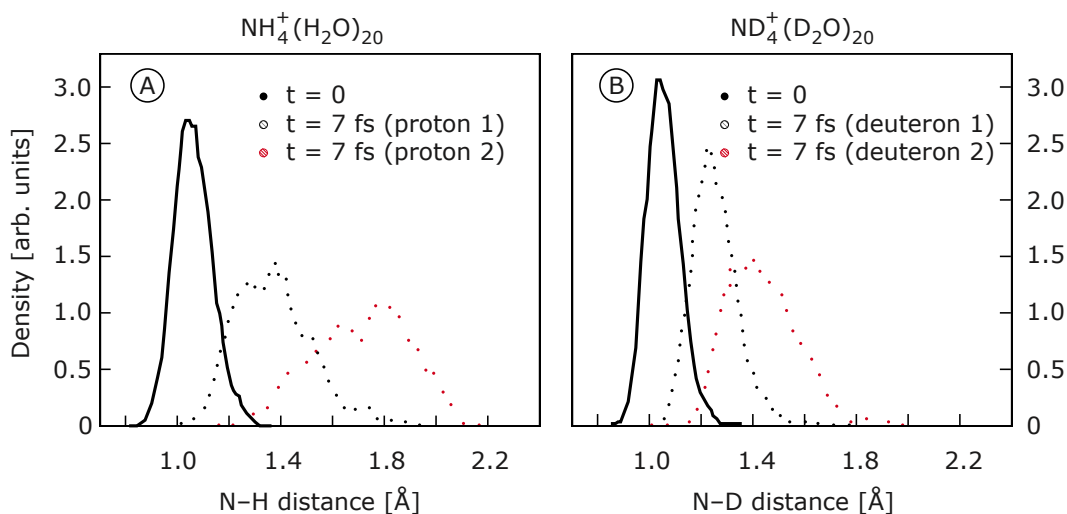


**Figure 5.10:** Time-dependent proton (deuteron) densities along the proton (deuteron) transfer coordinates obtained from MD simulations on the core-ionized state of the (Panel A)  $\text{NH}_4^+(\text{H}_2\text{O})_{20}$  and (Panel B)  $\text{ND}_4^+(\text{D}_2\text{O})_{20}$  clusters. The initial structures were taken from liquid-phase MD simulations of the solvated ammonium cation in the ground state. Densities along the strongest (dashed line) and second strongest (dotted line) N–H bonds are shown after 7 fs, together with the ground-state proton density (thick line). Figure adapted from Ref<sup>265</sup>.

first (strongest hydrogen-bonded) deuteron is at 1.4 Å N–D distance, while the second deuteron peaks at 1.2 Å after 7 fs.

Similar to our previous studies on  $\text{NH}_3$  the signature of PTM-ICD is expected at the high-KE side of the N 1s autoionization spectrum near 380 eV KE.<sup>259</sup> Figure 5.11 shows autoionization spectra from 2 M  $\text{NH}_4\text{Cl}$  (in  $\text{H}_2\text{O}$ ) and 2 M  $\text{ND}_4\text{Cl}$  (in  $\text{D}_2\text{O}$ ) aqueous solutions measured at 500 eV photon energy. Spectra are presented as measured. Only intensities were scaled in order to align the integrated area under both curves, which is justified by similar ionization- and decay cross sections of normal and deuterated ammonium. The spectrum exhibits a distinct double-peak structure, which we will refer to as peak A and peak B. The first observation in Figure 5.11 is a distinct isotope effect on the high-KE side of the spectrum, which aligns with our expectations that autoionization creates 1h1h final states with a high probability in  $\text{NH}_4^+$ .  $\text{ND}_4\text{Cl}$  (aq) has considerably less intensity on the high-KE shoulder than  $\text{NH}_4\text{Cl}$  (aq). Note, that less high-KE signal of  $\text{ND}_4\text{Cl}$  (aq) is compensated for by more intensity on the peak maximum of feature A and B. This is a well-known effect, which we have seen already for  $\text{H}_2\text{O}$ . The abundance of 1h1h final states correlates with a decrease of 2h states, as a core-ionized state can only

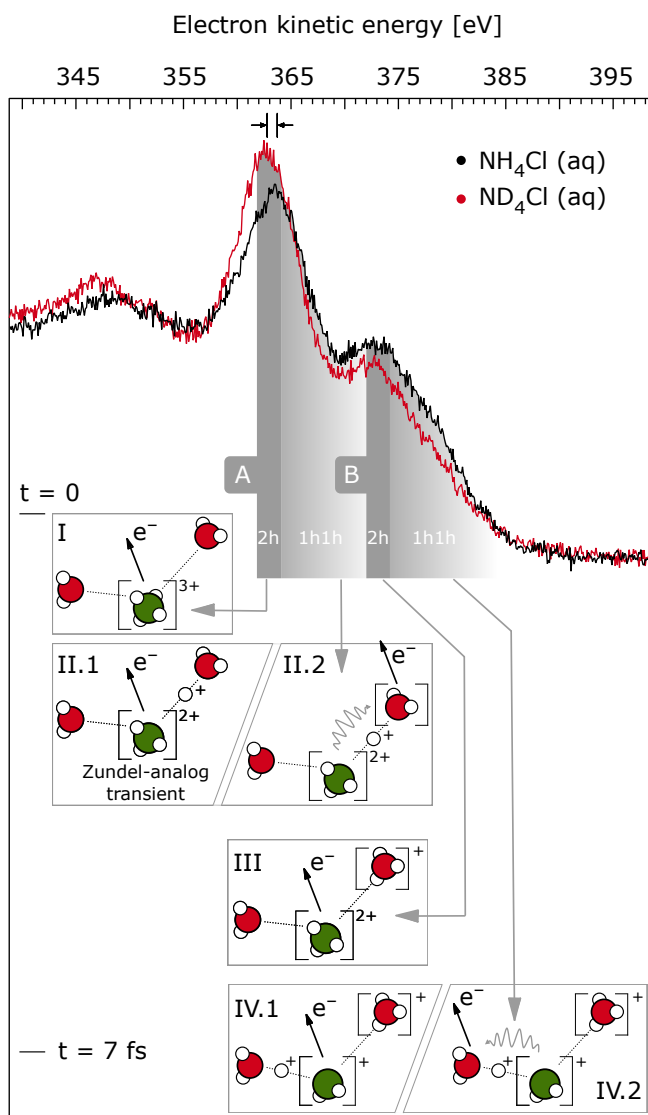


**Figure 5.11:** Top: Nitrogen 1s autoionization spectra from 2 M  $\text{NH}_4\text{Cl}$  (black curve) and 2 M  $\text{ND}_4\text{Cl}$  (red curve) aqueous solution measured at 500 eV photon energy. Peak A is assigned to 2h states of  $\text{NH}_4^+$  while peak B represents 2h states of  $\text{NH}_3$ . Bottom: Schematic illustration of the proton dynamics occurring upon N 1s core ionization. Only two water monomers are illustrated for simplicity. The single cartoons illustrate: (I) Local Auger decay of core excited  $\text{NH}_4^{2+*}$ , (II) local Auger decay and ICD of proton-transferred transient  $\text{NH}_3^{+*} \cdots \text{H}^+ \cdots \text{H}_2\text{O}$ , (III) local Auger decay of core excited  $\text{NH}_3^{+*}$ , and (IV) local Auger decay and ICD of proton-transferred transient  $\text{NH}_2^{+*} \cdots \text{H}^+ \cdots \text{H}_2\text{O}$ . The cartoons are ordered vertically due to the temporal succession of the processes I to IV, with IV being completed after 7 fs. Figure adapted from Ref<sup>265</sup>.

decay by one pathway, creating either a 2h or a 1h1h final state. Peak A and B both show a similar isotope effect and are distinctly separated from each other. Note that non-local decay processes occur continuously while the proton transfer evolves, with rising probabilities at later times within the 6.4 fs and the abundance of 1h1h final states increases gradual with time. This, however, does not explain the drastic intensity increase leading to peak B. We therefore conclude that the peaks A and B correspond to two independently emitting species, each influenced by nuclear dynamics.

In contrast to H<sub>2</sub>O and NH<sub>3</sub>, NH<sub>4</sub><sup>+</sup> is not stable as a gas phase species, and thus we must rely on theory in estimating the leading local Auger energy of NH<sub>4</sub><sup>+</sup> (gas). To calculate the absolute energy position of the leading local Auger peak, we first calculated the energy of the leading Auger peak in the gas phase as the difference between the core-ionized state and the ground state of the doubly-ionized system. Further details regarding the simulation are found in Refs<sup>272–274</sup>. After determining the gas-phase energy, we can estimate the solvent energy-shift using a polarizable continuum model according to Refs<sup>235,275</sup>. The model employed was first tested for well-studied water and ammonia molecules. All results are compared in Table 5.1. As can be inferred from Table 5.1 calculated gas-phase energies are within 0.1 eV accuracy and aqueous phase is within 0.5 eV accuracy. The experimentally non-existent gas phase NH<sub>4</sub><sup>+</sup> value is calculated to be at 349.8 eV and in the aqueous phase at 361.9 eV, which is only 0.6 eV below the center

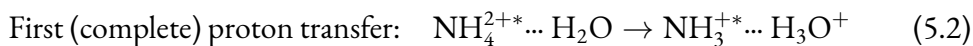
**Table 5.1:** Calculated and experimental energies of the leading (local) Auger peak for H<sub>2</sub>O, NH<sub>3</sub> and NH<sub>4</sub><sup>+</sup> in the gas phase and in aqueous solution. The calculated gas-phase values were obtained using the MOM-CCSD(T) method with cc-pCVTZ basis set for heavy atoms and cc-pVTZ basis set for hydrogen atoms. The solvent shift was calculated within a polarizable continuum model as described in Ref<sup>265</sup> and has been used to determine the theoretical Auger energies for aqueous phase. The molecular geometries were optimized at the MP2/cc-pVTZ level. Experimental values for H<sub>2</sub>O and NH<sub>3</sub> are taken from Figure 5.1 and Ref<sup>259</sup>, respectively. The value for NH<sub>4</sub><sup>+</sup> (aq) is obtained from Figure 5.11 (peak A), and the bracket indicates that the peak assignment is assisted by computations. Table reprinted from Ref<sup>265</sup>.

Species	Energy (gas) [eV]		Energy (aq) [eV]	
	Exp.	Theory	Exp.	Theory
H <sub>2</sub> O	498.6	498.7	503.1	503.6
NH <sub>3</sub>	370.0	374.0	374.0	374.4
NH <sub>4</sub> <sup>+</sup>	not available	349.8	(362.5)	361.9

of peak A. The calculations assume ground-state geometry of the system, thus ignoring the dynamics of the core-ionized state. An isotope shift of approximately 600 meV can already be seen for the local peak A, as indicated by arrows in Figure 5.11. Our calculations show for the gas-phase molecule the N–H bonds are elongated by 0.1 Å which leads to a 600 meV shift to higher KEs. Thus, we have evidence to assign peak A at 362.5 eV as the leading local Auger peak of  $\text{NH}_4^+$  (aq).

As argued above, peak B has to be the signature of a different decay channel, unrelated to local and non-local decays of  $\text{NH}_4^+$  and its transient structures. A most likely explanation of the presence of peak B is based on the following consideration (compare cartoons in Figure 5.11): At  $t = 0$  after the ionization event, the only possible structure, with 100% contribution to the autoionization signal, is  $\text{NH}_4^{2+*} \dots \text{H}_2\text{O}$ , assigned to peak A. The dominant electronic decay channel in this case is local Auger decay leading to 2h states as shown in panel (I). The core-ionized state establishes a proton transfer from ammonium to a neighboring water monomer and  $\text{NH}_3^{+*} \dots \text{H}^+ \dots \text{H}_2\text{O}$  transient structures evolve in time, as shown in panel (II). Peak A broadens with increasing  $\text{NH}_3^{+*} \dots \text{H}^+$  distance. Auger (II.1) and ICD (II.2) electrons emitted during the transfer process carry more KE due to reduced Coulombic interaction and thus contribute to the high-KE side of peak A. The population of these transient structures decays exponentially as they are formed later in time and autoionization continuously drains the population. The emergence of a new peak B hence indicates that a new relaxation channel opens within  $t < 6.4$  fs, leading to a sudden increase of electron emission near 373 eV KE. We conclude that once a full proton transfer is completed, as predicted from the dynamics calculations, core-ionized ammonia remains:  $\text{NH}_3^{+*} \dots \text{H}^+ \dots \text{H}_2\text{O} \rightarrow \text{NH}_3^{+*} \dots \text{H}_3\text{O}^+$ . The peak B is thus a signature of local Auger decay of the core-ionized ammonia molecule which forms upon complete proton migration. This coincides with the location of the leading aqueous phase 2h Auger peak of  $\text{NH}_3$  (aq) at 374 eV, compare Ref<sup>259</sup>. Panel (III) illustrates the local Auger decay of ammonia. Panel (IV) shows the analog process to panel (II), with (IV.1) being the Auger decay and (IV.2) the ICD of the transient proton-transferred structures. The second proton transfer is slower and does not exhibit a complete transformation. The predicted

mechanism is summarized in the following equations:



The first proton transfer leads to the formation of core-ionized ammonia  $\text{NH}_3^{+*}$  and a hydronium cation within  $<6.4$  fs. As soon as the first proton transfer is completed,  $\text{NH}_3^{+*}$  decays via local Auger and ICD. The second proton transfer creates an intermediate  $\text{NH}_2^* \dots \text{H}^+ \dots \text{H}_2\text{O}$  structure. Note that the two proton motions are not sequential, yet the  $\text{NH}_3$  signature only appears as the first proton, be it either of both, is fully transferred. Hence, the existence of the well separated peak B confirms the remarkable conclusion of a full chemical reaction  $\text{NH}_4^{2+} \rightarrow \text{NH}_3^+$  within less than 10 fs which, to our best knowledge, has never been observed before in an experiment. Due to the very effective charge separation observed here and the fact that ion pairing in ammonium chloride is well characterized<sup>276</sup>, the ammonium cation seems a very suitable test case for probing the local environment.

In this chapter I presented non-local electronic decay mechanisms which are general phenomena in hydrogen-bonded systems. Furthermore, I discussed experimental and theoretical findings of nuclear dynamics supporting the population of 1h1h final states. Yet, in certain cases it is impossible to distinguish decay rates quantitatively and to differentiate between competing non-local autoionization channels, e.g., ICD *versus* ETMD, as they create free electrons with comparable KEs. In the next chapter, I show how it is possible to discriminate certain decay channels, i.e., local Auger decay and ICD, by the choice of the system.

# 6

## ETMD in Aqueous Lithium Solutions

ETMD has been predicted theoretically to occur in hydrogen-bonded complexes.<sup>64,126,249</sup> As other decay channels (ICD, PTM-Auger decay, etc.) effectively compete with ETMD<sup>36,119,277,278</sup>, we chose a system in which no other non-radiative relaxation channel than ETMD is allowed. Hence, autoionization signal (if present) can be unambiguously assigned to ETMD electrons. We measured lithium in aqueous solution in the form of lithium chloride, LiCl, and lithium acetate, CH<sub>3</sub>COOLi (short: LiOAc). Upon Li 1s core ionization the lithium cation assumes an 1s<sup>1</sup>2s<sup>0</sup> excited state which cannot relax via Auger decay or ICD due to the lack of occupied higher orbitals.<sup>126</sup> However, ETMD remains a possible decay channel. The results presented in this chapter have been published in Refs<sup>122,127</sup>.

In order to describe the possible ETMD pathways that can be expected in LiCl (aq), I refer to Figure 6.1. Li 1s ETMD always features a non-local electron transfer between the ionized Li<sup>2+</sup> and a neighboring water molecule. Figure 6.1 only illustrates the most relevant ETMD pathways and ignores orbital specific ETMD. The simplest case is electron transfer between lithium and one single neighboring water molecule. In this case, the electron-donating water molecule emits an ETMD electron and the process is referred to as ETMD(2): W<sup>-2</sup>. The number in brackets refers to the number of monomers involved

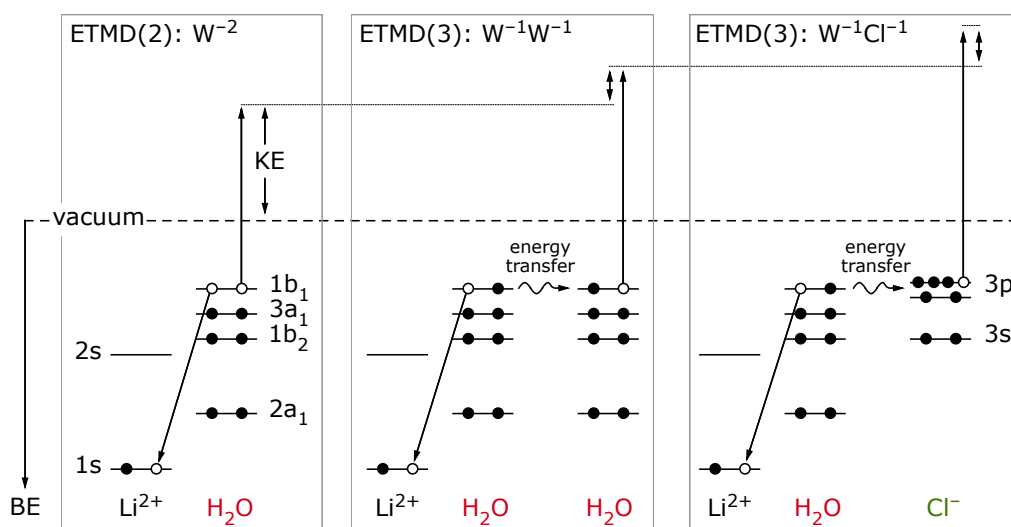


**Figure 6.1:** Energy-level diagram of the three most relevant ETMD channels in Li 1s ionized LiCl (aq): ETMD(2):  $W^{-2}$ , ETMD(3):  $W^{-1}W^{-1}$ , ETMD(3):  $W^{-1}Cl^{-1}$ . The number in brackets refers to the number of monomers involved in the respective ETMD process, including lithium, and the letters (W and Cl) indicate the neighboring species involved. Superscripts describe the electron vacancies in the final state of the respective molecule or atom (e.g.,  $W^{-1}$  indicates a water monomer with one electron missing). KE denotes the kinetic energies of electrons emitted in the ETMD processes. These are measured in the experiment.

in the respective ETMD process, including lithium, and the letters (W  $\hat{=}$  Water and Cl) indicate the neighboring species involved.<sup>123</sup> Superscripts describe the electron vacancies in the final state of the respective molecule (e.g.,  $W^{-1}$  indicates a water monomer with one electron missing). ETMD(2):  $W^{-2}$  creates a doubly ionized final state with both electron vacancies located at one water molecule. The second process shown in Figure 6.1 is ETMD(3):  $W^{-1}W^{-1}$  which involves three monomers. The lithium core-hole is again refilled by a water electron while the excess energy transfers to a third, so far uninvolved water molecule and induces electron ejection. The final 1h1h state (one hole at each water) creates ETMD electrons with higher Coulombic energy due to reduced Coulombic interaction. ETMD(3):  $W^{-1}Cl^{-1}$  is analog to the ETMD(3):  $W^{-1}W^{-1}$  process but with the excess energy transferred to a nearby chloride anion. The emitted ETMD electron originates from electron detachment of chloride and carries potentially even higher KE, because Cl<sup>-</sup> has weaker bound occupied orbitals than water.



## 6.1 ETMD AS A PROBE FOR LOCAL SOLVATION

In Figure 6.1 I have shown that the KE of the emitted ETMD electron depends fully on the molecules and orbitals involved in the decay process. Neglecting electron–electron interactions, Coulombic interactions, core-hole screening and dielectric contributions one can roughly estimate the KE of the outgoing ETMD electron according to the following relation:

$$KE_{\text{ETMD}} = 60.4 \text{ eV} - E_1 - E_2 \quad (6.1)$$

The Li 1s BE is 60.4 eV<sup>191</sup> and  $E_1/E_2$  are the BEs of the orbitals involved in the process. If taking only the highest occupied orbitals into account ( $1b_1 = 11.2$  eV BE and Cl 3p = 9.5 eV BE<sup>136</sup>), one can estimate the KEs of the three above ETMD processes to:  $KE(\text{ETMD}(2): W^{-2}) = KE(\text{ETMD}(3): W^{-1}W^{-1}) = 38.0$  eV and  $KE(\text{ETMD}(3): W^{-1}Cl^{-1}) = 39.7$  eV. When considering the  $3a_1$  (13.5 eV BE) of water the involved orbital these values change to 33.4 eV and 37.4 eV respectively. Apparently, electrons emitted in different ETMD processes have different KEs and thus are expected to show different characteristic spectral shapes depending on the specific decay mechanism. Based on this consideration, our motivation was to gain information about the local environment around lithium by exploiting the short-distance dependence of the ETMD rates. Note that the time scale of ETMD is short ( $\sim$ fs) compared to the minimum lifetime of an ion pair in solution ( $\sim$ ns).

In order to quantify the energies of the diverse ETMD processes more precise *ab initio* calculations on small cluster models with fixed geometries have been performed by the Slavíček group. As ETMD only involves the nearest neighbors, calculations have been performed for three explicit solvation configurations: Contact (CP), solvent-shared (SShP) and solvent-separated (SSP) ion pairs. All clusters consist of one  $Li^+$  cation, one  $Cl^-$  anion, and five solvent water molecules, while the  $Li^+$  cation is fully solvated in all three clusters. The  $Li^+ - Cl^-$  distance is inferred from the radial distribution functions in Figure 6.2A, being 2.4 Å in the CP model, 4.3 Å in the SShP model and 6.4 Å in the SSP model. The distances between the ions and the nearest water molecules are fixed to  $d(Li^+ - O) = 1.95$  Å and  $d(Cl^- - O) = 3.18$  Å. The radial distributions show that CP abundance rises with rising LiCl concentration. Quantitatively, CPs amount to 17% for

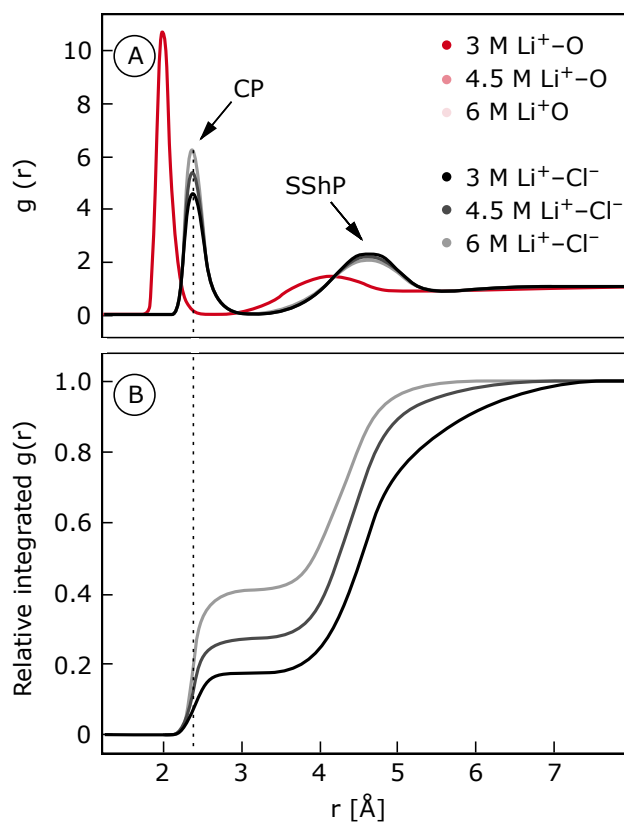


**Figure 6.2:** Panel A: Radial distribution functions for LiCl aqueous solutions. Shown are the  $\text{Li}^+-\text{Cl}^-$  and  $\text{Li}^+-\text{O}$  radial distribution functions for 3 M, 4.5 M and 6 M LiCl (aq). The first maximum of  $\text{Li}^+-\text{Cl}^-$  at  $r = 2.36$  Å corresponds to a contact ion pairing. The second peak of these curves at  $r = 4.62$  Å is attributed to a solvent-shared ion pair structure. Panel B: Integration of the (background-free) curves for  $\text{Li}^+-\text{Cl}^-$  shown in panel A up to a certain distance value. The first plateau gives the percentage of contact ion pairs: 17% for 3 M, 27% for 4.5 M and 40% for 6 M solution. Figure adapted from the supplementary information of Ref<sup>122</sup>.

the 3 M, 27% for the 4.5 M, and 40% for the 6 M solutions, as can be inferred from Figure 6.2B. The prevailing configuration is always the SShP geometry, yet the number of CPs becomes considerable with very high concentrations. This is reasonable as the number of available water molecules contributing to an intact solvation shell around  $\text{Li}^+$  diminishes at high salt concentrations.

The ETMD double-ionization energies of the clusters were calculated using the second-order algebraic diagrammatic construction method, ADC(2), which is an approximation scheme for the two-particle propagator. Further details of this method are described in Refs <sup>122,249,279</sup>. The computed ETMD spectra for all three models are shown in Figure 6.3. For each model transition probabilities of all possible ETMD channels were calculated. The ETMD channels are color-coded, indicating ETMD(3):  $\text{W}^{-1}\text{W}^{-1}$  (red), ETMD(3):  $\text{W}^{-1}\text{Cl}^{-1}$  (green), ETMD(2):  $\text{W}^{-2}$  (blue) and ETMD(2):  $\text{Cl}^{-2}$  (yellow). The theoretical spectra are shifted to higher KEs by 7.65 eV, 5.03 eV and 3.89 eV for SSP, SShP and CP models, respectively, in order to align at the ETMD(3):  $\text{W}^{-1}\text{W}^{-1}$  curve maximum. We chose this contribution since it is the most probable decay channel in the calculated concentration range, and thus contributing most to the overall ETMD spectrum.

As already mentioned the SShP model (middle panel in Figure 6.3) is the most prominent in all concentrations. It exhibits a well-defined main peak at 31 eV KE and two smaller peaks, one spreading between 20 eV and 25 eV KE and another one at 38 eV KE. The decomposition reveals that the peak maximum at 31 eV KE mainly arises from ETMD(3):  $\text{W}^{-1}\text{W}^{-1}$ . A detailed analysis reveals that most of the electrons originate from deeper-lying  $3a_1$  orbitals of water. The highest  $1b_1$  orbitals contribute only in small fractions. The favored decay of  $3a_1$  electrons results from beneficial orientations of the water monomers in the first solvation shell around  $\text{Li}^+$ . The oxygen atoms of water point towards the cation thus maximizing the overlap of the  $3a_1$  orbitals (compare top part of Figure 4.1) with the spherical  $1s$  orbital of  $\text{Li}^+$ . The low (26 eV KE) and high-KE (36 eV KE) tails of the ETMD(3):  $\text{W}^{-1}\text{W}^{-1}$  curve (red) arise from  $1b_2/3a_1$  and  $1b_1/3a_1$ -ionized states, respectively. The intensity between 15 eV and 25 eV KE is essentially attributed to ETMD(2):  $\text{W}^{-2}$ . Again, the relaxation involves predominantly  $3a_1$  orbitals. The different intensities between ETMD(3):  $\text{W}^{-1}\text{W}^{-1}$  and ETMD(2):  $\text{W}^{-2}$  can be ex-

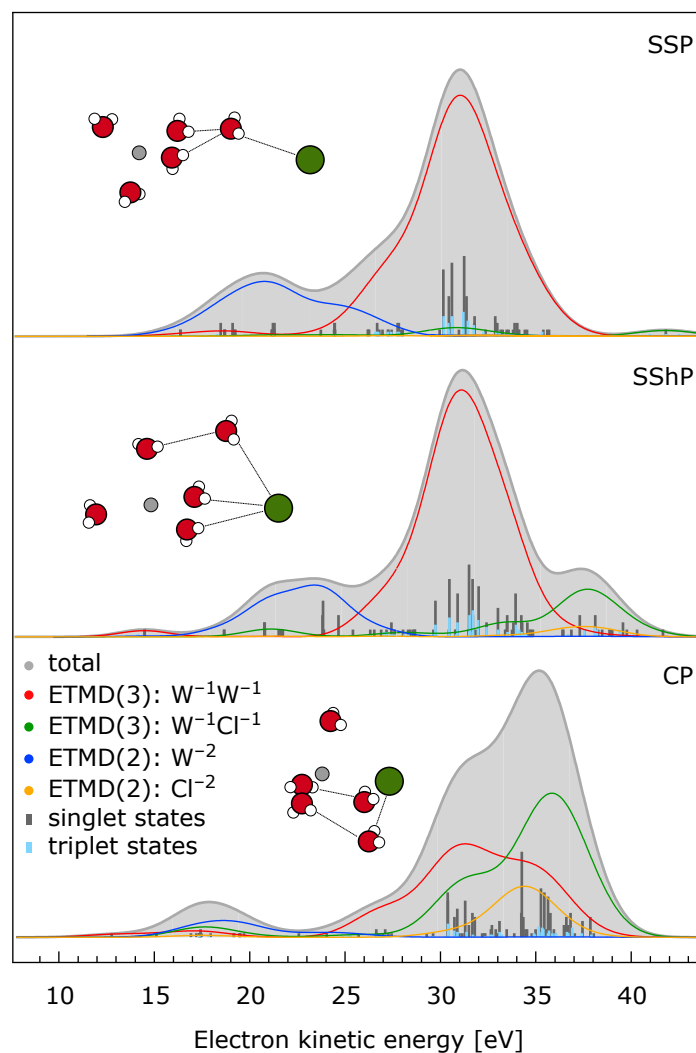


**Figure 6.3:** Theoretical ETMD spectra as calculated from the three cluster models representing (top) solvent-separated (SSP), (middle) solvent-shared (SSHP) and (bottom) contact (CP) ion pairing. The solid gray line always represents the total ETMD spectrum while the colored lines show the contribution of the different ETMD pathways, see legend. Transition intensities responsible for the spectra are visualized by bars on the bottom of each spectrum. The spectrum is created by applying a 3.6 eV broadening to the transitions. The geometries of the cluster models are depicted in the insets of each spectrum (red: oxygen; green:  $Cl^{-}$ ; grey:  $Li^{+}$ ; white: hydrogen). Figure adapted from Ref<sup>122</sup>.

plained by the fact that ETMD between  $\text{Li}^+$  and water scales approximately proportional with the number of available water monomers. However, while ETMD(2):  $\text{W}^{-2}$  only involves water molecules in the first solvation shell, ETMD(3):  $\text{W}^{-1}\text{W}^{-1}$  also reaches out to the second solvation shell. This is caused by the short-distance dependence of ETMD, yet for ETMD(3):  $\text{W}^{-1}\text{W}^{-1}$  the transfer-electron donating water monomer in the first solvation shell can very well transfer its energy to a water monomer in the next (third) shell. The high-KE side of the SShP model spectrum arises from ETMD(3):  $\text{W}^{-1}\text{Cl}^{-1}$ . The overall ETMD spectrum of the SSP model (top panel in Figure 6.3) has a similar structure except for the missing peak at 38 eV KE and a slightly more pronounced shoulder of the main peak at 26 eV KE. This is attributed to a similar structure of the first solvation shell of  $\text{Li}^+$  in both cluster models. Although the arrangement of water molecules in the first solvation shell of  $\text{Li}^+$  is very similar for SSP and SShP cluster models, structures differ significantly beyond the first solvation shell. The counter ions are much closer (only separated by one water monomer) in the SShP model, which enhances the probability for ETMD(3):  $\text{W}^{-1}\text{Cl}^{-1}$ . This is responsible for the missing feature at 38 eV KE in the SSP model. In the CP model (bottom panel in Figure 6.3), however, the ETMD(3):  $\text{W}^{-1}\text{Cl}^{-1}$  feature (green) dominates the overall shape of the spectrum and becomes the main peak, while ETMD(2):  $\text{W}^{-2}$  and ETMD(3):  $\text{W}^{-1}\text{W}^{-1}$  have still considerable contribution. However, the contribution of these two processes decreases due to the reduced number of water monomers in the first solvation shell in the CP model. The shape of ETMD(3):  $\text{W}^{-1}\text{W}^{-1}$  curve (red) changes dramatically. This is caused by different water orbitals coming into play. The CP influences the first-shell water structure such that the Li 1s orbital overlaps better with water  $1b_1$ . This promotes ETMD processes involving  $1b_1$ , which contribute to the high-energy side of the ETMD(3):  $\text{W}^{-1}\text{W}^{-1}$  spectrum (at 36 eV KE). Also, the CP model is the only configuration in which ETMD(2):  $\text{Cl}^{-2}$  exists substantially. ETMD(2):  $\text{Cl}^{-2}$  creates a  $\text{Cl}^+$  cation.

## 6.2 EXPERIMENTAL EVIDENCE OF ETMD

After I have shown that the spectral shape of an ETMD spectrum can be well related to the local molecular environment, I now discuss the experimental measurements. Our motivation is to observe experimental signatures of increased contact pairing in  $\text{LiCl}(\text{aq})$

when going from moderately high (3 M) to very high (8 M) concentrated solutions. As shown in Figure 6.2 we expect enhanced contact pairing for rising salt concentrations. Provided this is true, ETMD would be a straight indicator for the presence of CPs. The detection of ETMD electrons is experimentally challenging. ETMD signature is expected in the 30–40 eV KE range. This is a region where a large background from secondary (inelastically scattered) electrons forms the low-kinetic energy part of the photoelectron spectrum (as explained in Chapter 2). This background signal dominates the electron spectrum by far and ETMD is only observable by subtracting a reference (pure water) spectrum from the LiCl (aq) spectrum. This technique requires relatively long acquisition times and a stable liquid jet position. The top spectrum in Figure 6.4 shows data of a 120-minute measurement from water and LiCl (aq) at 171 eV photon energy (well above Li 1s at 60.4 eV BE). The difference between the top spectra (LiCl (aq) minus water) identifies ETMD electronic signal (plotted below in Figure 6.4). This is the first observation of ETMD in liquid phase. The subtracted spectra are noisy. In order to show that the data are statistically significant the as-measured individual data points have been five-point binned and the resulting error bars have been determined. The spectral shape matches qualitatively with the computed spectra. The peak maximum at 31.5 eV KE is close to the theoretical value (31 eV KE). A difference of 0.5 eV is probably due to residual repulsion energy that cannot be screened completely in aqueous media. The spectrum resembles best the theoretical spectrum for SShP cluster geometry, which is expected. Analogous measurements are also performed for 4.5 M LiCl (aq) at 175 eV photon energies, as shown in the bottom part of Figure 6.4. The first observation from this measurement is that the kinetic energy range of the difference spectrum is the same as for the 3 M solution. The insensitivity of the ETMD spectra on photon energy (171 eV *versus* 175 eV) confirms that the signal indeed arises from autoionization, rather than direct ionization. However, the effect of different ion pairing arrangements can only be barely quantified. The 4.5 M LiCl ETMD spectrum has slightly more intensity at the low-KE side (attributed to SSP) and slightly more intensity at the high-KE side (attributed to SShP). The poor signal-to-noise ratio and a too narrow range over which salt concentrations were varied hinders univocal observation of the ETMD spectral changes. Therefore, we repeated these measurements using the electron–electron coincidence method utiliz-

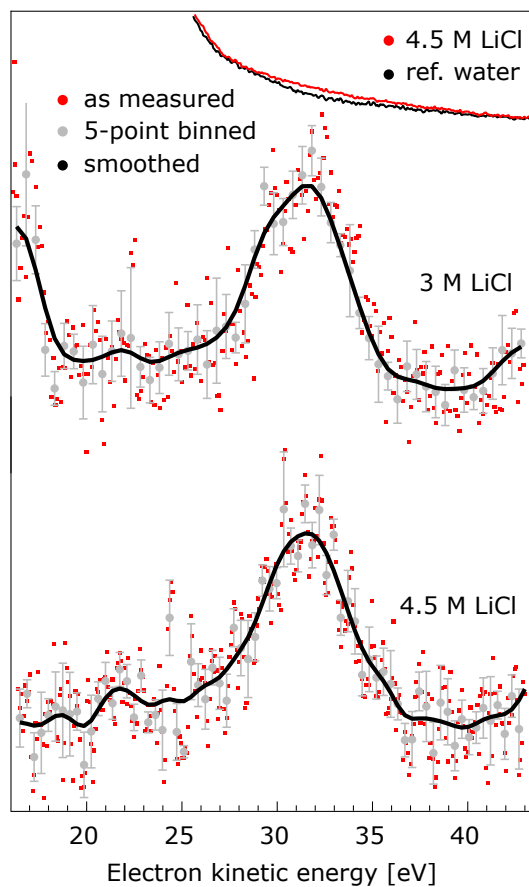


**Figure 6.4:** Top: The as-measured spectrum of 4.5 M LiCl aqueous solution (red) and the reference spectrum of neat water which only contains contributions from inelastically scattered photoelectrons (black), measured at 171 eV photon energy. Middle: Difference of the top spectra reveals ETMD signal with a maximum at 31 eV KE. Bottom: The analog data as the spectrum in the middle but for 4.5 M concentration, and a photon energy of 175 eV. Figure adapted from Ref<sup>122</sup>.

ing a magnetic-bottle TOF spectrometer, as introduced in Section 3.4. The coincidence technique aims to detect ETMD electrons with significantly reduced background signal, in order to find changes in ETMD spectral shapes as a function of salt concentration. This will be demonstrated in the next section.

### 6.3 ION-PAIRING: LiCl VERSUS LiOAc

In the last two sections I could show that ETMD can be measured in a PE experiment and that this type of spectroscopy has the potential of being a powerful tool for probing local solvation, such as ion pairing in aqueous solution. However, the measurement remains challenging due to the relatively low KE of the ETMD electrons. Standard PE spectroscopy using a conventional hemispherical electron analyzer failed to provide sufficient signal statistics to unequivocally observe ETMD spectral changes as a function of solute concentration. In order to elaborate on the sensitivity of ETMD to local atomic environment, we employ the electron–electron coincidence technique using a magnetic bottle time-of-flight spectrometer to achieve better signal statistics, with significantly less contribution of background electrons. This approach has been recently demonstrated for the inner-valence ionization of water clusters, where ICD electrons could be distinguished from the direct photoelectrons.<sup>280</sup> We follow a two-fold strategy: First, we extend the LiCl (aq) concentration range to higher concentrations: 4.5 M, 6 M and 8 M. Especially at very high concentrations (8 M) a significant amount of CPs is expected, which should be reflected in the ETMD spectra as enhanced intensity at higher KEs. Second, we explore the actual sensitivity of this spectroscopy to the counterion by performing back-to-back measurements from LiCl and LiOAc aqueous solutions. LiOAc is chosen in particular because previous studies showed a strong tendency for close contact between  $\text{Li}^+$  and the acetate anion.<sup>119</sup> The strong interaction is a result of the high electronegativity of the acetate group and a bidentate ion-pair geometry.  $\text{Cl}^-$  is less electronegative and the  $\text{Li}^+ - \text{Cl}^-$  contact pair has a monodentate geometry.

A typical coincidence map of LiCl (aq) measured at 110 eV photon energy is presented in Figure 6.5. The main window plots all coincidence events detected within 800 ns, which is the repetition rate of the BESSY II light pulses in single-bunch mode. Remember from Section 3.5, that most of the signal in the map results from random co-



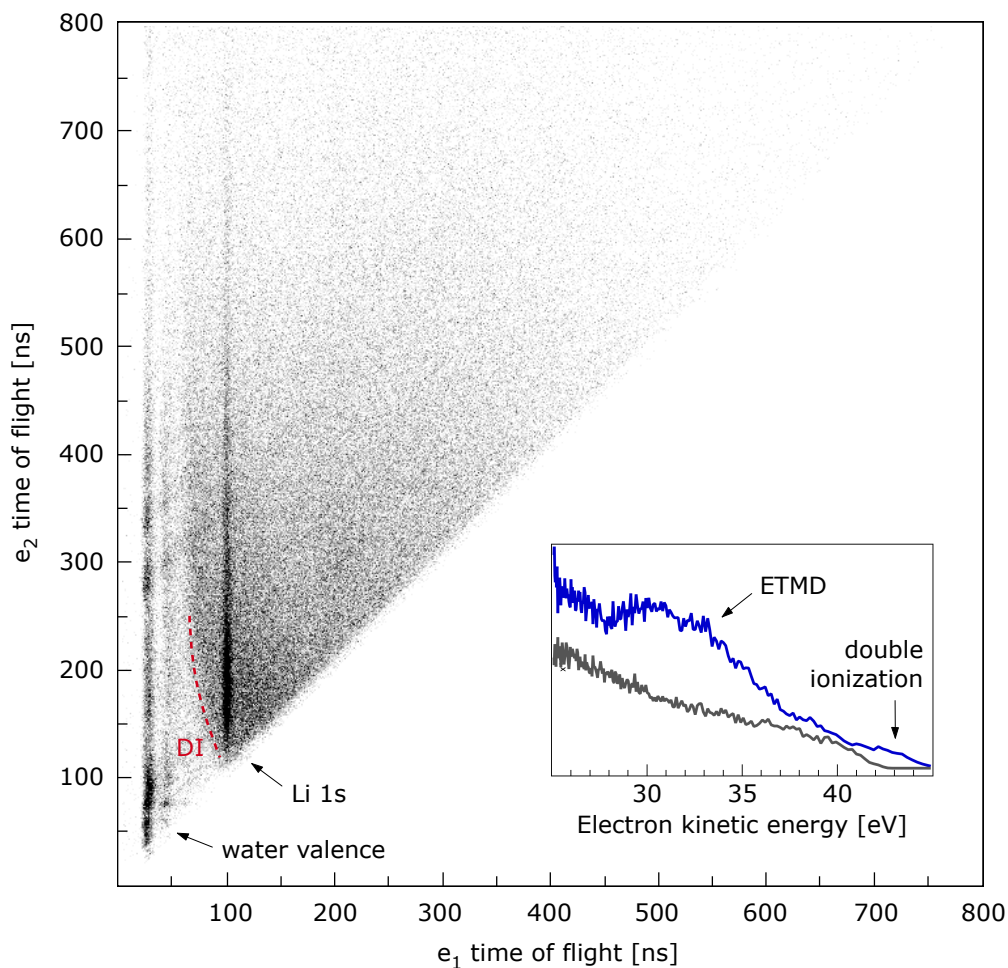


**Figure 6.5:** Main window: Coincidence map of electron pairs detected after photoionization of LiCl aqueous solution (8 M) at 110 eV photon energy. Electron pairs are plotted *versus* their time-of-flight, while the flight times of the faster electron is plotted along the horizontal axis, and the slower ones along the vertical axis. Short flight times correspond to high electron kinetic energies, and *vice versa*. Vertical features of increased point density indicate processes at which the first electron arises from photoionization. Hyperbolic lines (in one instance marked by a dashed red line), indicate double ionization (DI) events with a random energy sharing between the two electrons. Inset: Spectra created from integration along the region of enhanced line density and a region right besides, which are attributed to Li 1s ionization and random noise, respectively. The spectra are transformed into a kinetic-energy scale. The pronounced difference (27 eV to 37 eV KE) is due to ETMD upon Li 1s ionization and the small difference in the 41 eV to 45 eV KE region is caused by double-ionization. Figure adapted from the supplementary information of Ref<sup>127</sup>.

incidences, which can have multiple reasons. Signals from direct photoemission appear as vertical lines in the map since electrons resulting from these processes will coincide with ‘random’ electrons. This can be well seen at approximately 50 ns flight time ( $e_1$ -axis) where vertical lines represent signal from water valence ionization. The hyperbolic line (red dashed line) is caused by double ionization events. This can be the result of inelastic scattering of a valence photoelectron, which kicks out another valence electron from a second water molecule (usually in the gas phase surrounding the jet). Those electron pairs can have any KE combination, as long as the sum of the two energies equals the initial photon energy minus the respective two-hole final state energy. Note that  $W^{-1}W^{-1}$  is the most likely final state for double-ionization as water molecules are the most abundant species. Faint diagonal striations starting, e.g., at 280 ns and 350 ns on the  $e_2$  axis are an artifact from the detector electronics. Enhanced signal density due to Li 1s photoionization is found at  $e_1 \approx 100$  ns in the map of Figure 6.5. Integration over a narrow range around 100 ns along the  $e_2$ -axis reveals a well resolved feature between 28 eV and 37 eV KE. The so-created spectrum is plotted as a function of KE of the second electrons in the inset of Figure 6.5. Oxygen 1s photoelectron spectra of liquid water were used as calibration points. Note that the hyperbolic line from double-ionization events intersects with the blue dashed line giving rise to the enhanced signal between approximately 41 eV and 45 eV KE in the blue spectrum in the inset of Figure 6.5. We observe this feature to diminish with rising salt concentrations which matches with our explanation of electron scattering ionization off a water molecule. The observed main feature is a strong evidence that Li 1s ionization triggers second-order electron emission. A background-free spectrum is created by subtracting a region directly adjacent to the ROI (dark gray line in the inset of Figure 6.5).

The ETMD spectra from electron–electron coincidence measurements at 110 eV photon energy are presented in Figure 6.6. The shown spectra in Figure 6.6A represent data from 4.5 M LiCl (black line) and LiOAc (red line) aqueous solutions. The 4.5 M LiCl spectrum from Figure 6.4 (bottom spectrum), which was measured in a non-coincident fashion using a hemispherical electron spectrometer is shown for comparison (black dashed line). The most conspicuous observation is that qualitatively, no differences between the two spectra are seen. They are similar in shape and energy, which unequivocally

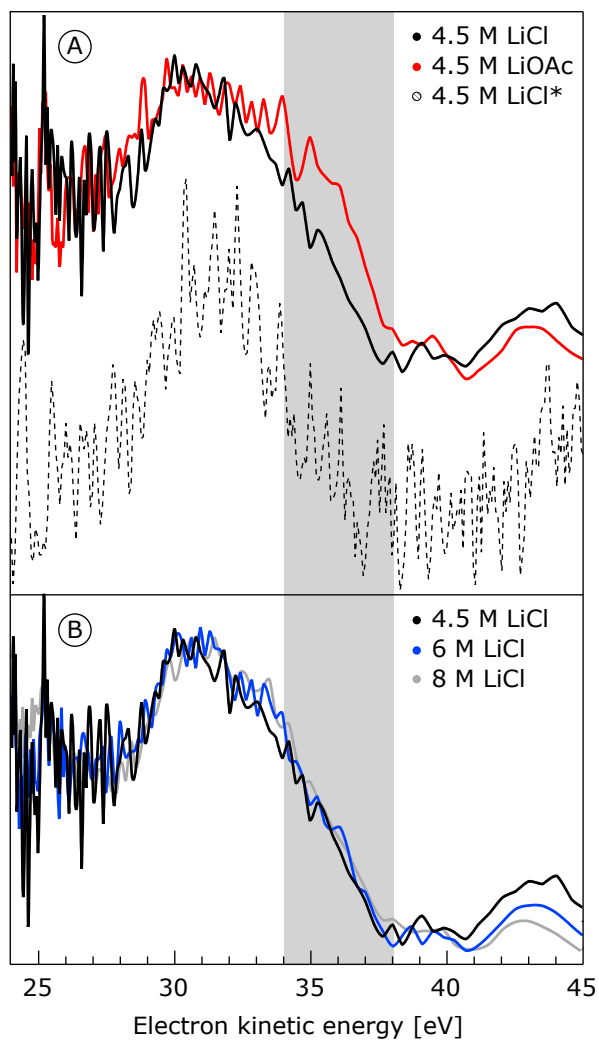


**Figure 6.6:** Panel A: Li 1s ETMD spectra from 4.5 M aqueous LiCl (black) and 4.5 M aqueous LiOAc (red), measured by electron–electron coincidence at 110 eV photon energy. The bottom spectrum (black dashed) is reprinted from Figure 6.4, representing 4.5 M LiCl (aq) measured with a conventional hemispherical electron analyzer. Panel B: ETMD spectra from LiCl (aq) of 4.5 M (black), 6 M (blue), and 8 M (gray) salt concentration. The gray rectangle spanning over panels A and B indicates the energy region between 34 eV and 38 eV KE in which enhanced ETMD signal intensity from contact ion pairing is predicted. Figure reprinted from Ref<sup>127</sup>.

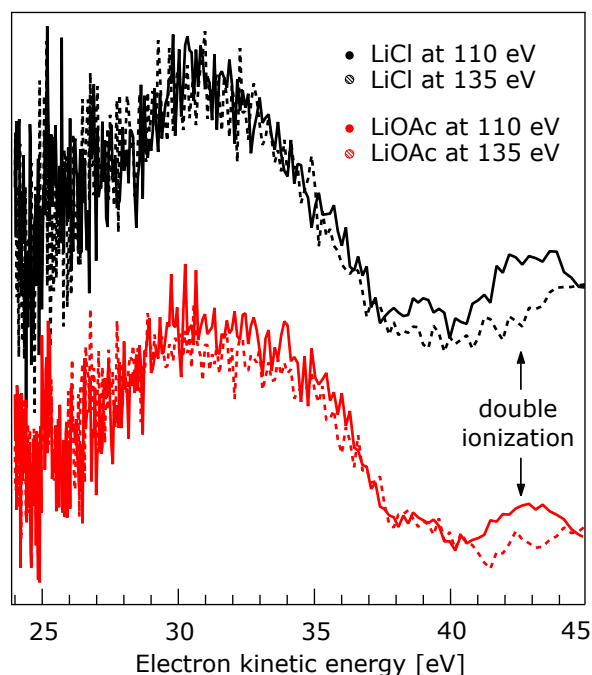


**Figure 6.7:** Li 1s ETMD electron spectra from 4.5 M aqueous LiCl (black) and 4.5 M aqueous LiOAc (red), measured by electron–electron coincidence. For both solutions, spectra measured at 110 eV photon energy are compared to 135 eV photon energy. The spectra are qualitatively and quantitatively equal, except for the region between 41 eV and 45 eV KE. This feature is due to double-ionization brought by electron impact from valence photoelectrons with other water valence electrons. The kinetic energy of electron pairs produced by double ionization scales with photon energy and is therefore not apparent in the 135 eV spectra. Figure adapted from the supplementary information of Ref<sup>127</sup>.

cally confirms that both, the spectra measured in Figure 6.4 and here indeed arise from Li 1s ETMD. This interpretation is further supported by the fact that no photon energy dependencies are seen in Figure 6.7, as expected for an autoionization process. Yet, it is noteworthy that the signal-to-background ratio in the coincidence experiment is roughly 1:2, compared to 1:50 in the former measurements. When comparing the LiCl (aq) and LiOAc (aq) spectra we observe a distinct difference in the 34 eV to 38 eV KE range (see gray rectangle in Figure 6.6A). The spectrum of lithium acetate exhibits a pronounced shoulder at the high-KE side, showing considerably higher intensity than LiCl. This difference is the first experimental proof of ETMD being indeed sensitive to the local atomic environment. Assuming that for both, LiCl (aq) and LiOAc (aq), the counterions do not participate in the decay process, identical ETMD spectra would be expected, since ETMD(2):  $W^{-2}$  and ETMD(3):  $W^{-1}W^{-1}$  are the only possible mechanisms. The

highest occupied orbital of acetate in aqueous solution is at 9.24 eV BE (compare Figure 6.8) which is only 0.26 eV apart from Cl 3p and considerably lower than the water 1b<sub>1</sub> BE. Thus, we expect the signature of a Li<sup>+</sup>–CH<sub>3</sub>COO<sup>−</sup> pair at the high-KE side of the ETMD spectrum (similar to LiCl). The observation that LiOAc has higher signal intensity than LiCl at that particular region is also expected, due to closer ion pairing for LiOAc (aq) than for LiCl (aq).<sup>119</sup> Based on the spectral differences observed it is safe to conclude that ETMD spectroscopy is indeed sensitive to contact ion pairing and to the nature of the counterion.

#### 6.4 THE STRONG HYDRATION SHELL OF AQUEOUS LITHIUM

The absence of any detectable difference in the ETMD spectra from 4.5 M, 6 M and 8 M LiCl concentrations in Figure 6.6B is surprising. Considering that at 8 M LiCl concentration the water-to-lithium ratio is around six\* (neat water has 55.345 M concentration at 25° C),<sup>39</sup> one Li<sup>+</sup>–Cl<sup>−</sup> pair shares on average approximately six water molecules. The complete hydration shell of Li<sup>+</sup> consists of four water molecules, and six water molecules for Cl<sup>−</sup>.<sup>281</sup> This implies a shortage of available water molecules and thus a considerable fraction of Li<sup>+</sup> cations should at least share its solvation shell with Cl<sup>−</sup> (SShP). A more dilute solution of 4.5 M has on average enough water molecules to provide an intact hydration shell for every ion. This consideration aligns with MD simulations that show an increase of CPs over the concentration range we have probed.<sup>122,282–286</sup> An absence of CPs for concentrations lower than 1 M has been measured.<sup>287</sup> However, the ETMD spectrum remains unchanged when probing increasing salt concentrations which is in contrast to these studies; see in particular the region within the gray rectangle in Figure 6.6B.

The lack of sensitivity can have several reasons. Reviewing the literature offers an unclear picture of lithium hydration. Studies using dielectric relaxation spectroscopy and neutron diffraction with isotopic substitution conclude with this statement.<sup>288</sup> For example, molecular simulations revealed a fraction of paired Li<sup>+</sup> ions from approximately 0.35 to 0.44 when the concentration is increased from 4.5 M to 8 M, which is smaller than in our simple estimate but surely high enough to be observed spectroscopically.<sup>281</sup> An understanding of the influence of orbital type and orientation on ETMD probabilities is

---

\*The ratio calculates:  $([\text{H}_2\text{O}] - [\text{LiCl}])/[\text{LiCl}] = (55.345 \text{ M} - 8 \text{ M})/8 \text{ M} \approx 5.92$

**Table 6.1:** Normalized areas of Li 1s and Cl 2p core level photoelectron peaks (arbitrary units) under conditions that are preferentially surface sensitive (100 eV KE) *versus* preferentially bulk sensitive (600 eV KE). Figure reprinted from Ref<sup>127</sup>.

Species, KE	4.5 M	6 M	8 M	Comment
Li 1s, 100 eV	$2.16 \cdot 10^{-8}$	$2.36 \cdot 10^{-8}$	$6.57 \cdot 10^{-8}$	
Cl 2p, 100 eV	$1.88 \cdot 10^{-8}$	$2.70 \cdot 10^{-8}$	$6.75 \cdot 10^{-8}$	
Li 1s, 600 eV	$4.85 \cdot 10^{-6}$	$1.56 \cdot 10^{-5}$	$1.24 \cdot 10^{-5}$	
Cl 2p, 600 eV	$5.65 \cdot 10^{-6}$	$1.42 \cdot 10^{-5}$	$1.28 \cdot 10^{-5}$	
Li 1s/Cl 2p, 100 eV	1.15	0.87	0.97	Surface sensitive
Li 1s/Cl 2p, 600 eV	0.86	1.10	0.97	Bulk sensitive

still unclear. We know that ETMD decay probabilities depend on the orbital type and orientation, e.g., for water the  $3a_1$  orbital is the dominant electron donating orbital.<sup>289</sup> However, one explanation might also be that decay pathways involving water are highly favored over those involving chloride. A third possible explanation for the lack of sensitivity to different solute concentration is the surface sensitivity of electron spectroscopy. For 30–40 eV KE electrons the electron escape depth is only 0.6–2 nm.<sup>129</sup> All ETMD electrons thus originate from the first few monolayers of the solution. We believe, based on literature, that LiCl (aq) exhibits a structure distinctly different from that in bulk solution.<sup>136,138,210,290</sup> Two recent studies using MD simulation<sup>291</sup> and PE spectroscopy<sup>292</sup> suggest a quite unique behavior of  $\text{Li}^+$  compared to other (bigger) halides due to its small size. Unlike the larger cations,  $\text{Li}^+$  keeps an intact solvation shell at the solution interface which can explain the lack of observed CPs in our experiments. The referred MD simulations, however, neglect contributions from a polarizable force field, which were found to be important in other MD simulations.<sup>286,290</sup> A profound understanding of the LiCl (aq)–vacuum interface is still lacking. To trust the surface explanation, we can check the solutions for changing depth-dependent  $\text{Li}^+/\text{Cl}^-$  ratios. This is possible by comparing direct photoelectron spectra of Li 1s and Cl 2p at two different fixed kinetic energies: 100 eV to be surface sensitive and 600 eV to probe deeper into the solution. The resulting  $\text{Li}^+/\text{Cl}^-$  signal ratios at any concentration are given in Table 6.1. These measurements were performed using a hemispherical electron analyzer. The spectra were separately normalized to acquisition time, beamline flux for the respective photon energy (measured with a calibrated photodiode) and the atomic photoionization cross sections taken from

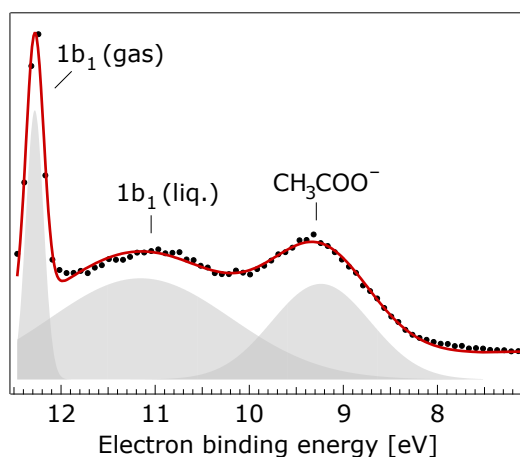


**Figure 6.8:** Direct valence PE spectrum of 4.5 M LiOAc in aqueous solution. Gaussian peaks in gray correspond to fits of the water  $1b_1$  orbitals and to the  $\text{CH}_3\text{COO}^-$  highest occupied orbital.

calculations.<sup>293</sup> The intensity ratio of Li to Cl peaks can be used to assess whether one of the two species has a propensity for populating bulk or surface sites. If there was an ion-specific density profile that changes with LiCl concentration, the ratio would deviate from unity for bulk or surface sensitive conditions, respectively. However, no trend arises from this analysis. We do not believe that the very small deviations indicate a layering, especially considering alternating trends of the ratios in Table 6.1, i.e., the big-to-small-to-unity behavior for 100 eV KE and *vice versa* for 600 eV KE. Note that this analysis does not conclude that there is no layering in LiCl solution, it only shows that a layering, if present, does not depend on the concentration. On the other side, the PE measurement of aqueous acetate suggests a considerable surface propensity of the acetate ion, as can be seen by the large signal intensity of the  $\text{CH}_3\text{COO}^-$  highest occupied orbital in Figure 6.8. This observation is in line with theory<sup>294</sup> and would explain the strong CP ETMD signal for the lithium chloride solution.

Nonetheless, the principle sensitivity of ETMD spectroscopy to local solvation could be demonstrated by using a magnetic-bottle TOF spectrometer, yet an effect of solvation structure as a function of salt concentration could not be observed. ETMD may occur not only here but also in a variety of other solvated metal cations, both after photoionization<sup>295</sup> and as a part of various cascades.<sup>64</sup> Aqueous LiCl solution has been extensively studied, both experimentally and by means of molecular dynamics simulations, yet its structure, in particular ion pairing, is not yet fully understood. The high sensitivity of

ETMD to local structure may be a powerful spectroscopic tool for studying various properties of not only aqueous solutions but also systems with organic or hybrid solvents, for example in Li-ion batteries where the knowledge of ion pairing and local solvation structure is essential for optimization of the ionic conductivity and the energy transfer rate.<sup>296</sup> In the future, ETMD spectroscopy on further systems are promising for detailed understanding of non-local decay processes in general. As such,  $\text{Mg}_2\text{Cl}(\text{aq})$  is a interesting candidate; according to a recent study a non-local autoionization cascade arises upon Mg 1s core ionization creating on average 2.4 slow electrons and 4.3 radicals per 1s vacancy.<sup>64</sup> As these species are known to effectively cause biochemical damage, a detailed understanding of the processes in magnesium are of great importance.



# 7

## Summary

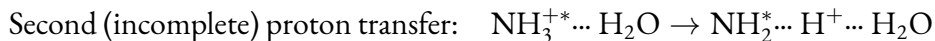
I have presented a compilation of my findings on core-level X-ray photoelectron spectroscopy from aqueous solutions. The systems under investigation and detection schemes were the following:

- Direct photoionization spectroscopy from NaI (aq)
- Intermolecular Coulombic decay (ICD) spectroscopy from  $\text{NH}_4^+\text{Cl}$  (aq) and  $\text{ND}_4^+\text{Cl}$  (aq)
- Electron-transfer mediated decay (ETMD) spectroscopy from LiCl (aq) and LiOAc (aq)

Exemplified for NaI (aq), I could show that despite drastic changes of the chemical environment (when going from dilute to highly concentrated NaI aqueous solution) the PE spectrum of water stays remarkably constant. The combined experimental and theoretical study revealed a largely unchanged PE spectrum with only minor energy shifts of the water  $1b_2$  peak ( $370 \pm 60$  meV) and a reduced spacing between the two  $3a_1$  peaks ( $450 \pm 90$  meV) when going from 0.05 M to 8 M NaI (aq). This work justifies the common procedure for energy-aligning liquid-water PE spectra at the lowest ionization energy (water  $1b_1$ ), which was shown to be stable compared to most other water valence

and solute PE peaks throughout all salt concentrations. The apparent insensitivity of the water PE spectrum to the molecular environment is surprising, especially when compared with the large sensitivity of core-level PE spectroscopy to the chemical environment (chemical shifts of several eV).<sup>297,298</sup> I conclude that the insensitivity observed in our PE experiments is a result of the large screening ability of polar liquids.

I have demonstrated ICD to be a general phenomenon in weakly-interacting systems not only for neutral molecules, but also for initially charged cations. The study of  $\text{NH}_4^+$  (aq) and  $\text{ND}_4^+$  (aq) has shown that ICD scales strongly with hydrogen-bond strength. Another remarkable observation was a double-proton transfer which could be shown to proceed ultrafast, on a sub-10 fs timescale. Such a fast complete chemical reaction has never been observed in liquid phase to date to the best of my knowledge. The proton-transfer dynamics have been identified by spectral analysis of ICD in  $\text{NH}_4\text{Cl}$  and  $\text{ND}_4\text{Cl}$  and *ab initio* MD simulations. Differences in the autoionization spectra when comparing aqueous ammonium and its deuterated form could be explained by different hydrogen/deuteron dynamics, which have an influence on the KE of emitted ICD electrons. In the experiment an arising new peak in the N 1s autoionization regime could be univocally assigned to core-excited  $\text{NH}_3^{+*}$  which has formed within the 6.4-fs lifetime of the nitrogen 1s vacancy. The double proton transfer is best described with the following equations:



ETMD could be shown to be a sensitive tool for ion pairing in aqueous salt solutions. This has been proven experimentally for the first time by measuring PE signal with electron–electron coincidence from LiCl and LiOAc in aqueous solution using a magnetic-bottle TOF spectrometer. Different decay routes following Li 1s core-ionization result in slightly different ETMD electron kinetic energies. Furthermore, the decay routes are determined by the local solvation of the core-ionized  $\text{Li}^+$ . As a consequence, ETMD spectroscopy can be exploited to probe local hydration. Although it was not possible to resolve different types of ion pairing in varying LiCl (aq) solutions, I have

shown the potential of using ETMD spectroscopy as a new method for local solvation by demonstrating counterion sensitivity between LiCl (aq) and LiOAc (aq). The lack of spectral evidence for changing ion-pairing situations in the different LiCl solutions has been explained by the particular special hydration of the small Li<sup>+</sup> anion which essentially keeps an intact tetragonal hydration shell even at high salt concentrations. This study reveals the need for further investigation of different salt solutions and theoretical support in order to disentangle the different ETMD decay pathways and finally quantify the amount of ion pairing. A more advanced description for orbital selectivity of ETMD would be a particular demand for future theoretical work.



# 8

## Outlook

### ON ABSOLUTE BINDING ENERGIES OF LIQUID WATER

Exemplified for NaI in aqueous solution I was able to show that the PE spectrum from liquid water is essentially insensitive to solutes. However, the presented study deals only with relative BE, i.e., spacings between selected peaks are evaluated. Whether the measured energies are correct in terms of absolute binding energies could not be clarified. In order to determine exact BE values, several aspects leading to KE shifts of measured electrons have to be considered. Sample charging, i.e., the accumulation of uncompensated charge at the jet surface, is arguably the strongest influence on electron KEs. To date three major effects leading to sample charging in our experimental setup have been identified.

First of all, a liquid flow that streams through a tubing is subject to friction between liquid surface and the inner walls of the tubings. This leads to accumulation of charge on the jet surface, which influences the KEs of outgoing electrons. Negative excess charge at the jet surface reduces the KEs of ejected electrons and *vice versa*. The amount of charge scales linearly with a change in electron KE (and thus measured BE), as is best demonstrated by our unpublished results presented in Figure 8.1A. This figure presents a series of valence PE experiments from liquid water with different bias voltages applied, from +1 V to

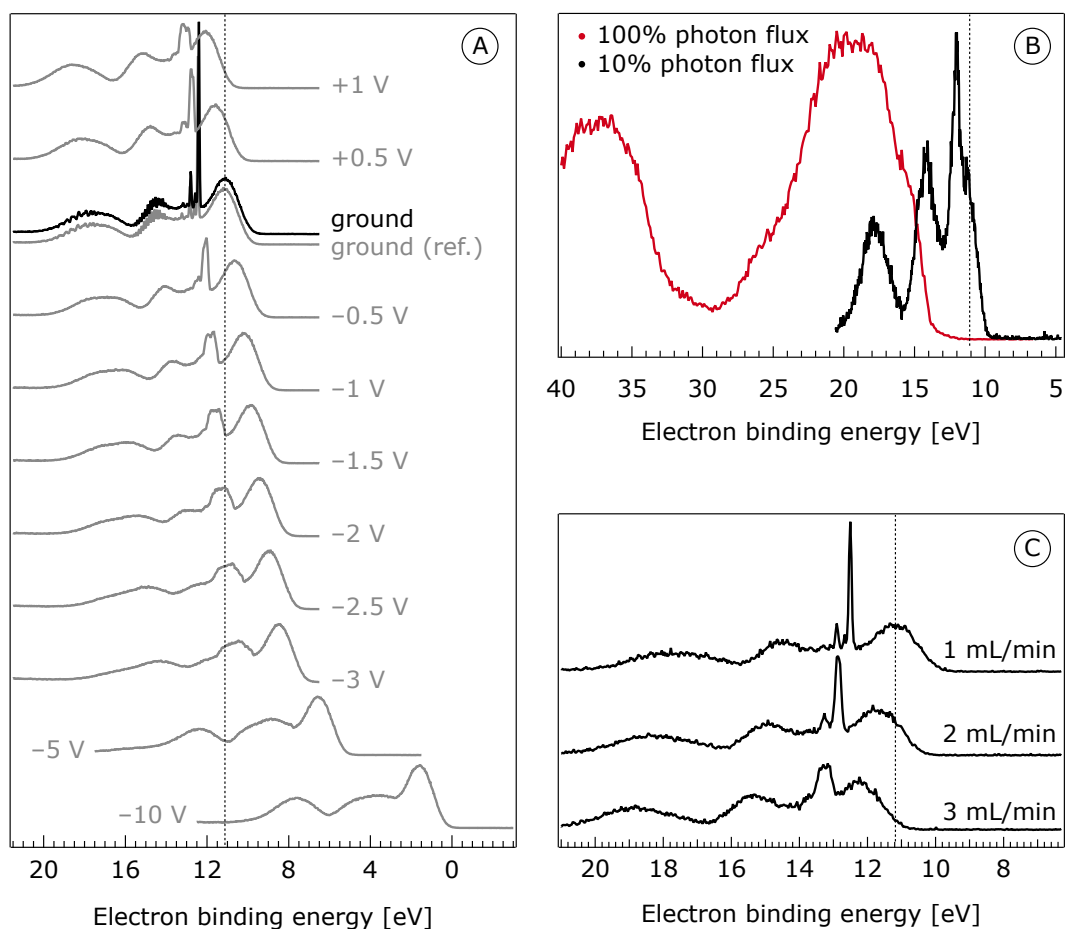


**Figure 8.1:** Valence PE spectra from a liquid-water jet at different experimental conditions. The photon energy was set to 175 eV. Panel A: 0.05 M NaCl (aq) at different applied bias voltages. Panel B: Neat water at 100% photon flux (corresponding to  $3 \cdot 10^{13}$  photons/sec) and 10% photon flux. Panel C: Neat water at 10% photon flux and different liquid-flow rates.

-10 V. This experiment mimics the above described effect caused by friction, which I refer to as electrokinetic charging. It is apparent that the liquid phase  $1b_1$  peak scales directly with bias voltage, which is because the emitted electrons experience the full potential between jet and analyzer. However, electrons emitted from the gas phase only experience a fraction of the total applied voltage, i.e., they experience more de/-acceleration when born near the jet and less when born near the analyzer. As a result, the gas phase features smear out with rising voltages, and thus rising potential gradient, while the liquid-phase peaks keep a constant peak width and intensity. Note, that the gas phase water peak energy and shape in the very first liquid-jet studies of the Winter group showed a constant  $1b_1$  gas phase energy, even if the jet was moved off-sight from the spectrometer detection axis by

about 100  $\mu\text{m}$ .<sup>28</sup> This encouraged these authors to assume the gas-phase spectrum to be a constant energy reference. However, we see from Figure 8.1A that this is not the case. This missing effect is due to the large photon beam focal size of  $250 \times 120 \mu\text{m}^2$  used at that time, which (i) still ionizes the jet when moved off-axis, thus still induces a potential between jet and analyzer, and (ii) ensures that the same number of gas phase molecules is ionized than for the on-axis position. As a result, the gas phase spectrum remains constant in that particular experiment but is still different from a gas phase experiment without a jet.

The second effect of charge accumulation results from photoionization of the jet. This is particularly important when measuring at high-intensity synchrotron light sources, which leads to local but very high charge densities. Figure 8.1B demonstrates very well how high flux can distort a whole PE spectrum. While the valence spectrum at 10% beam-line flux (corresponding to  $3 \cdot 10^{12}$  photons/sec) is well resolved, it is completely shifted and broadened for maximum photon flux (corresponding to  $3 \cdot 10^{13}$  photons/sec). First attempts in determining the exact ionization energies in a liquid-jet experiment have been made by reducing sample flow and light flux drastically while grounding the jet as close as possible to the point of injection. A preliminary result is shown in Figure 8.1C, which shows that for sufficient reduction of light flux and sample flow the liquid water PE spectrum becomes well resolvable. A linear shift to higher BEs is clearly seen in this measurement, which is a strong indication for the accumulation of positive charge at the jet surface. Reducing the flow rate considerably does not guarantee that the so acquired spectra show correct absolute BEs but demonstrates possible strategies in order to avoid sample charging in a liquid-jet PE experiment. A common procedure to compensate for charge accumulation is by adding millimolar salt concentrations to the measured solution (e.g., 50 mM NaCl to neat water), as has been done for all neat water experiments described in this thesis.

Another issue is the question on Fermi-level *versus* vacuum-level reference in liquid-phase PE spectroscopy. A recent study raises doubts against the common procedure of referencing liquid samples against the vacuum level rather than the Fermi level as it is justified for solid state.<sup>299</sup> This aspect is still under debate but will certainly be important for the determination of absolute binding energies.

## ON ETMD AS A PROBE FOR ION-PAIRING

ETMD has been shown to be a general phenomenon for aqueous phase systems. Furthermore, the predicted sensitivity to contact ion pairing could be demonstrated for different counterions of aqueous  $\text{Li}^+$  solution. What remains to be demonstrated is that ETMD spectroscopy can be adapted to further aqueous systems. We have chosen  $\text{MgCl}_2$  as a next promising candidate. When ionized at the 2p level we observe clear ETMD signature, as can be seen in Figure 8.2. The spectra are normalized to experimental acquisition time. Small ETMD spectral changes can be observed with rising salt concentration (2 M, 3 M and 5 M  $\text{MgCl}_2$ ). I attribute this spectral change to altering ion-pair configurations, since ETMD is sensitive to the closest neighboring chemical environment (see Chapter 6). The low-KE side of the spectrum appears to have enhanced intensity for higher concentrations. A conclusive interpretation of the observed change is only possible with theoretical support, nonetheless it is already promising that concentration-dependent changes are apparent. Note, that the spiky structure of the spectra is an artifact of the instrument electronics, which we will eliminate in the future.

## ON ICD AND PROTON DYNAMICS

Several systems have been proven to enhance ICD rates (compared to local Auger) when accompanied with a proton transfer between the decay partners. I have presented this behavior for different hydrogen-bonded systems, such as  $\text{H}_2\text{O}$ ,  $\text{H}_2\text{O}_2$  (aq),  $\text{NH}_3$  (aq), and  $\text{NH}_4^+$  (aq). However, recent unpublished results from the Hergenbahn group indicate the opposite behavior for valence-excited (rather than core-excited) water clusters. The authors observe a suppression of ICD efficiency for  $2a_1$  inner-valence excited states. This behavior can be rationalized by proton transfer, which according to calculated potential-energy surfaces closes the ICD channel. This is contrary to the core-level ICD channel, which is open at each geometry and is even enhanced by proton movement. This aspect will be the topic of the thesis of one of my coworkers and I therefore refrain from going deeper into detail.



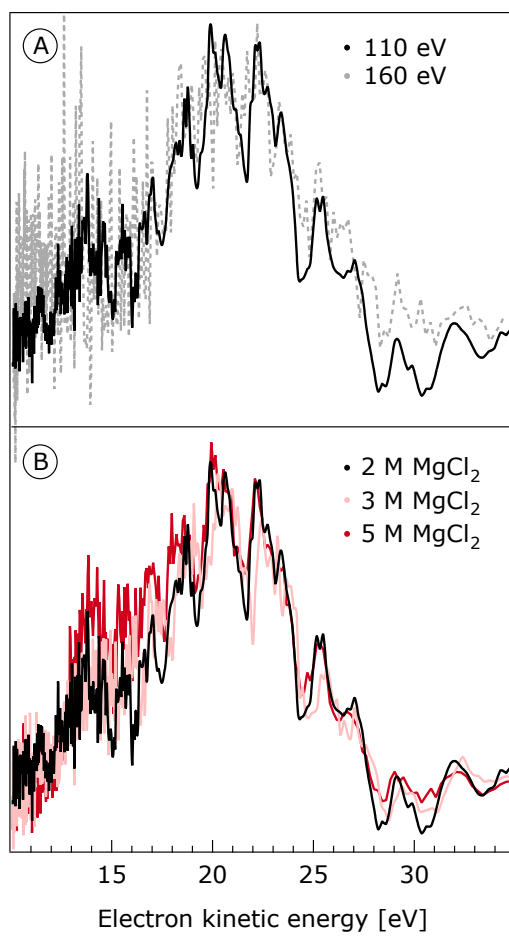


**Figure 8.2:** Mg 2p ETMD spectra from aqueous MgCl<sub>2</sub>, measured by electron–electron coincidence. Panel A: Spectra from 2 M MgCl<sub>2</sub> (aq) measured at 110 eV and 160 eV photon energies. Panel B: Spectra from 2 M, 3 M and 5 M MgCl<sub>2</sub> (aq) measured at 110 eV.



# Bibliography

- [1] R. D. Holt, “Why science? Why AAAS?,” *Science*, vol. 347, no. 6224, p. 807, 2015.
- [2] S. Milgram, “Behavioral study of obedience,” *The Journal of Abnormal and Social Psychology*, vol. 67, no. 4, pp. 371–378, 1963.
- [3] National Academy of Sciences, National Academy of Engineering, and Institute of Medicine, *On Being a Scientist: A Guide to Responsible Conduct in Research*. Washington, DC: The National Academies Press, 3 ed., 2009.
- [4] D. Edwards, “Why science?,” *Science*, vol. 328, no. 5976, pp. 311–311, 2010.
- [5] A. Rohlfs Wright, “Witchcraft and science in the renaissance: the witch of edmonton, the late lancashire witches and renaissance,” *Endoxa*, vol. 1, no. 7, 1996.
- [6] D. C. Lindberg, *The Medieval Church Encounters the Classical Tradition: Saint Augustine, Roger Bacon, and the Handmaiden Metaphor*, pp. 7–32. University of Chicago Press, 2003.
- [7] *Dark Ages*, vol. 30 of *Oxford english dictionary*. Oxford University Press, 2008.
- [8] W. Naphy and A. Spicer, *Plague: Black Death and Pestilence in Europe*. Tempus, 2004.
- [9] S. Clark, *Thinking with Demons: The Idea of Witchcraft in Early Modern Europe*. Oxford University Press, 1999.
- [10] T. Berners-Lee and R. Cailliau, *WorldWideWeb: Proposal for a HyperText Project*. <https://www.w3.org/Proposal.html>, 1990, Online accessed: November 22, 2018.

- [11] S. McPherson, *Tim Berners-Lee: Inventor of the World Wide Web*. Twenty-First Century Books, 2009.
- [12] *The Official Website of the Nobel Prize*. <https://www.nobelprize.org>,  
Online accessed: November 22, 2018.
- [13] A. Fölsing, *Wilhelm Conrad Röntgen: Aufbruch ins Innere der Materie*. Dt. Taschenbuch-Verlag, 2002.
- [14] W. C. Röntgen, “On a new kind of rays,” *Science*, vol. 3, no. 59, pp. 227–231, 1896.
- [15] W. R. Hendee and E. R. Ritenour, *Medical Imaging Physics*. Wiley-Liss, 2002.
- [16] F. Arfelli, M. Assante, V. Bonvicini, A. Bravin, G. Cantatore, E. Castelli, L. Dalla Palma, M. Di Michiel, R. Longo, A. Olivo, S. Pani, D. Pontoni, P. Poropat, M. Prest, A. Rashevsky, G. Tromba, A. Vacchi, E. Vallazza, and F. Zanconati, “Low-dose phase contrast x-ray medical imaging,” *Physics in Medicine and Biology*, vol. 43, no. 10, pp. 2845–2852, 1998.
- [17] F. Pfeiffer, T. Weitkamp, O. Bunk, and C. David, “Phase retrieval and differential phase-contrast imaging with low-brilliance x-ray sources,” *Nature Physics*, vol. 2, no. 4, pp. 258–261, 2006.
- [18] I. James, T. Dobbins and J. G. Devon, “Digital x-ray tomosynthesis: Current state of the art and clinical potential,” *Physics in Medicine and Biology*, vol. 48, no. 19, p. R65, 2003.
- [19] J. D. Frierman, H. R. Bowman, I. Perlman, and C. M. York, “X-ray fluorescence spectrography: Use in field archeology,” *Science*, vol. 164, no. 3879, pp. 588–588, 1969.
- [20] D. Papadopoulou, A. Sakalis, N. Merousis, and N. C. Tsirliganis, “Study of decorated archeological ceramics by micro x-ray fluorescence spectroscopy,” *Nuclear Instruments and Methods in Physics Research Section A: Accelerators*,

- Spectrometers, Detectors and Associated Equipment*, vol. 580, no. 1, pp. 743–746, 2007.
- [21] H. Bronk, S. Röhrs, A. Bjeoumikhov, N. Langhoff, J. Schmalz, R. Wedell, H. E. Gorny, A. Herold, and U. Waldschläger, “Arttax – a new mobile spectrometer for energy-dispersive micro x-ray fluorescence spectrometry on art and archaeological objects,” *Fresenius’ Journal of Analytical Chemistry*, vol. 371, no. 3, pp. 307–316, 2014.
- [22] J. Dik, K. Janssens, G. Van der Snickt, L. van der Loeff, K. Rickers, and M. Cotte, “Visualization of a lost painting by vincent van gogh using synchrotron radiation based x-ray fluorescence elemental mapping,” *Analytical Chemistry*, vol. 80, no. 16, pp. 6436–6442, 2008.
- [23] B. K. Agarwal, *X-Ray Spectroscopy*. Springer Series in Optical Sciences, Heidelberg: Springer-Verlag Berlin, 1991.
- [24] J. D. Brock and M. Sutton, “Materials science and x-ray techniques,” *Materials Today*, vol. 11, no. 11, pp. 52–55, 2008.
- [25] R. C. Wolcott, *How Automation Will Change Work, Purpose, and Meaning*. <https://hbr.org/2018/01/how-automation-will-change-work-purpose-and-meaning>, 2018, Online accessed: November 22, 2018.
- [26] W. B. Arthur, *Where is technology taking the economy?* <https://www.mckinsey.com/business-functions/mckinsey-analytics/our-insights/where-is-technology-taking-the-economy>, 2017, Online accessed: November 22, 2018.
- [27] S. Hüfner, *Photoelectron Spectroscopy*. Advanced Texts in Physics, Heidelberg: Springer-Verlag Berlin, 3 ed., 2003.
- [28] B. Winter, R. Weber, W. Widdra, M. Dittmar, M. Faubel, and I. V. Hertel, “Full valence band photoemission from liquid water using EUV synchrotron radiation,” *The Journal of Physical Chemistry A*, vol. 108, no. 14, pp. 2625–2632, 2004.

- [29] B. Winter and M. Faubel, "Photoemission from liquid aqueous solutions," *Chemical Reviews*, vol. 106, no. 4, pp. 1176–1211, 2006.
- [30] A. Kolmakov, D. A. Dikin, L. J. Cote, J. Huang, M. K. Abyaneh, M. Amati, L. Gregoratti, S. Gunther, and M. Kiskinova, "Graphene oxide windows for in situ environmental cell photoelectron spectroscopy," *Nature Nanotechnology*, vol. 6, no. 10, pp. 651–657, 2011.
- [31] S. Axnanda, E. J. Crumlin, B. Mao, S. Rani, R. Chang, P. G. Karlsson, M. O. Edwards, M. Lundqvist, R. Moberg, P. Ross, Z. Hussain, and Z. Liu, "Using tender-x-ray ambient pressure x-ray photoelectron spectroscopy as a direct probe of solid-liquid interface," *Scientific Reports*, vol. 5, p. 9788, 2015.
- [32] R. Seidel, M. N. Pohl, H. Ali, B. Winter, and E. F. Aziz, "Advances in liquid phase soft-x-ray photoemission spectroscopy: A new experimental setup at BESSY II," *Review of Scientific Instruments*, vol. 88, no. 7, p. 073107, 2017.
- [33] M. Salmeron and R. Schlogl, "Ambient pressure photoelectron spectroscopy: A new tool for surface science and nanotechnology," *Surface Science Reports*, vol. 63, no. 4, pp. 169–199, 2008.
- [34] D. E. Starr, Z. Liu, M. Havecker, A. Knop-Gericke, and H. Bluhm, "Investigation of solid/vapor interfaces using ambient pressure x-ray photoelectron spectroscopy," *Chemical Society Reviews*, vol. 42, no. 13, pp. 5833–5857, 2013.
- [35] C. H. Wu, R. S. Weatherup, and M. B. Salmeron, "Probing electrode/electrolyte interfaces in situ by x-ray spectroscopies: Old methods, new tricks," *Physical Chemistry Chemical Physics*, vol. 17, no. 45, pp. 30229–30239, 2015.
- [36] S. Thürmer, M. Ončák, N. Ottosson, R. Seidel, U. Hergenbahn, S. E. Bradforth, P. Slaviček, and B. Winter, "On the nature and origin of dicationic, charge-separated species formed in liquid water on x-ray irradiation," *Nature Chemistry*, vol. 5, no. 7, pp. 590–596, 2013.

- [37] I. Unger, *Relaxation Processes in Aqueous Solutions upon X-ray Exposure: Entanglement of Electronic and Nuclear Dynamics*. Doctoral thesis, 2015.
- [38] P. Ball, *H<sub>2</sub>O: A Biography of Water*. Orion Publishing Group, 2015.
- [39] M. Chaplin, *Water Structure and Science*. <http://www1.lsbu.ac.uk/water/>, 2018, Online accessed: November 22, 2018.
- [40] J. Russo and H. Tanaka, "Understanding water's anomalies with locally favoured structures," *Nature Communication*, vol. 5, p. 3556, 2014.
- [41] P. Ball, "Water: water—an enduring mystery," *Nature*, vol. 452, no. 7185, pp. 291–292, 2008.
- [42] A. Brack, "Liquid water and the origin of life," *Origins of Life and Evolution of the Biosphere*, vol. 23, no. 1, pp. 3–10, 1993.
- [43] C. J. Fecko, J. D. Eaves, J. J. Loparo, A. Tokmakoff, and P. L. Geissler, "Ultrafast hydrogen-bond dynamics in the infrared spectroscopy of water," *Science*, vol. 301, no. 5640, pp. 1698–1702, 2003.
- [44] R. Kjellander and E. Florin, "Water structure and changes in thermal stability of the system poly(ethylene oxide)–water," *Journal of the Chemical Society, Faraday Transactions 1: Physical Chemistry in Condensed Phases*, vol. 77, no. 9, 1981.
- [45] C. J. Li and L. Chen, "Organic chemistry in water," *Chemical Society Reviews*, vol. 35, no. 1, pp. 68–82, 2006.
- [46] E. Jequier and F. Constant, "Water as an essential nutrient: the physiological basis of hydration," *European Journal of Clinical Nutrition*, vol. 64, no. 2, pp. 115–123, 2010.
- [47] A. V. Gubskaya and P. G. Kusalik, "The total molecular dipole moment for liquid water," *The Journal of Chemical Physics*, vol. 117, no. 11, pp. 5290–5302, 2002.

- [48] P. L. Silvestrelli and M. Parrinello, "Water molecule dipole in the gas and in the liquid phase," *Physical Review Letters*, vol. 82, no. 16, pp. 3308–3311, 1999.
- [49] A. Mozumder, Y. Hatano, and Y. Katsumura, *Charged Particle and Photon Interactions with Matter: Chemical, Physicochemical, and Biological Consequences with Applications*. CRC Press, 2010.
- [50] A. Eschenbrenner, M. A. Herve Du Penhoat, A. Boissiere, G. Eot-Houllier, F. Abel, M. F. Politis, A. Touati, E. Sage, and A. Chetioui, "Strand breaks induced in plasmid DNA by ultrasoft x-rays: influence of hydration and packing," *International Journal of Radiation Biology*, vol. 83, no. 10, pp. 687–697, 2007.
- [51] C. R. Wang, J. Nguyen, and Q. B. Lu, "Bond breaks of nucleotides by dissociative electron transfer of nonequilibrium prehydrated electrons: A new molecular mechanism for reductive DNA damage," *Journal of the American Chemical Society*, vol. 131, no. 32, pp. 11320–11322, 2009.
- [52] D. Becker and M. D. Sevilla, *The Chemical Consequences of Radiation Damage to DNA*, vol. 17 of *Advances in Radiation Biology*, pp. 121–180. Elsevier, 1993.
- [53] P. J. Black and W. A. Bernhard, "Excess electron trapping in duplex DNA: Long range transfer via stacked adenines," *Journal of Physical Chemistry B*, vol. 116, no. 44, pp. 13211–13218, 2012.
- [54] C. E. Crespo-Hernández, R. Arce, Y. Ishikawa, L. Gorb, J. Leszczynski, and D. M. Close, "Ab initio ionization energy thresholds of DNA and rna bases in gas phase and in aqueous solution," *The Journal of Physical Chemistry A*, vol. 108, no. 30, pp. 6373–6377, 2004.
- [55] M. Weik, R. B. G. Ravelli, G. Kryger, S. McSweeney, M. L. Raves, M. Harel, P. Gros, I. Silman, J. Kroon, and J. L. Sussman, "Specific chemical and structural damage to proteins produced by synchrotron radiation," *Proceedings of the National Academy of Sciences*, vol. 97, no. 2, pp. 623–628, 2000.



- [56] E. Alizadeh and L. Sanche, "Precursors of solvated electrons in radiobiological physics and chemistry," *Chemical Reviews*, vol. 112, no. 11, pp. 5578–5602, 2012.
- [57] B. C. Garrett, D. A. Dixon, D. M. Camaioni, D. M. Chipman, M. A. Johnson, C. D. Jonah, G. A. Kimmel, J. H. Miller, T. N. Rescigno, P. J. Rossky, S. S. Xantheas, S. D. Colson, A. H. Laufer, D. Ray, P. F. Barbara, D. M. Bartels, K. H. Becker, J. Bowen, K. H., S. E. Bradforth, I. Carmichael, J. V. Coe, L. R. Corrales, J. P. Cowin, M. Dupuis, K. B. Eisenthal, J. A. Franz, M. S. Gutowski, K. D. Jordan, B. D. Kay, J. A. Laverne, S. V. Lyman, T. E. Madey, C. W. McCurdy, D. Meisel, S. Mukamel, A. R. Nilsson, T. M. Orlando, N. G. Petrik, S. M. Pimblott, J. R. Rustad, G. K. Schenter, S. J. Singer, A. Tokmakoff, L. S. Wang, C. Wettig, and T. S. Zwier, "Role of water in electron-initiated processes and radical chemistry: Issues and scientific advances," *Chemical Reviews*, vol. 105, no. 1, pp. 355–390, 2005.
- [58] B. Boudaiffa, P. Cloutier, D. Hunting, M. A. Huels, and L. Sanche, "Resonant formation of DNA strand breaks by low-energy (3 to 20 eV) electrons," *Science*, vol. 287, no. 5458, pp. 1658–1660, 2000.
- [59] S. G. Swarts, D. Becker, M. Sevilla, and K. T. Wheeler, "Radiation-induced DNA damage as a function of hydration. ii. base damage from electron-loss centers," *Radiation Research*, vol. 145, no. 3, 1996.
- [60] M. E. Lomax, L. K. Folkes, and P. O'Neill, "Biological consequences of radiation-induced DNA damage: relevance to radiotherapy," *Clinical Oncology (Royal College of Radiologists)*, vol. 25, no. 10, pp. 578–585, 2013.
- [61] H. Willers, J. Dahm-Daphi, and S. N. Powell, "Repair of radiation damage to DNA," *British Journal of Cancer*, vol. 90, no. 7, pp. 1297–1301, 2004.
- [62] J. F. Ward, *Ionizing Radiation Damage to DNA*, pp. 431–439. Boston, MA: Springer US, 1999.

- [63] X. Ren, E. Jabbour Al Maalouf, A. Dorn, and S. Denifl, "Direct evidence of two interatomic relaxation mechanisms in argon dimers ionized by electron impact," *Nature Communication*, vol. 7, p. 11093, 2016.
- [64] V. Stumpf, K. Gokhberg, and L. S. Cederbaum, "The role of metal ions in x-ray-induced photochemistry," *Nature Chemistry*, vol. 8, no. 3, pp. 237–241, 2016.
- [65] R. W. Howell, "Auger processes in the 21st century," *International Journal of Radiation Biology*, vol. 84, no. 12, pp. 959–975, 2008.
- [66] B. W. R. F. Feuerbacher, B.; Fitton, *Photoemission and the Electronic Properties of Surfaces*, vol. 83 of *Berichte der Bunsengesellschaft für physikalische Chemie*. Chichester, New York, Brisbane, Toronto: Wiley-Blackwell, 1979.
- [67] F. J. Himpsel and I. Lindau, *Photoemission and Photoelectron Spectroscopy*, p. 285–318. American Cancer Society, 2009.
- [68] D. R. Penn, "Quantitative chemical analysis by ESCA," *Journal of Electron Spectroscopy and Related Phenomena*, vol. 9, no. 1, pp. 29–40, 1976.
- [69] H. Haken and H. C. Wolf, *Atom- und Quantenphysik*. Berlin Heidelberg: Springer-Verlag, 1983.
- [70] M. O. Krause, "Atomic radiative and radiationless yields for K and L shells," *Journal of Physical and Chemical Reference Data*, vol. 8, no. 2, pp. 307–327, 1979.
- [71] A. Einstein, "Über einen die Erzeugung und Verwandlung des Lichtes betreffenden heuristischen Gesichtspunkt," *Annalen der Physik*, vol. 322, no. 6, pp. 132–148, 1905.
- [72] H. Fellner-Feldegg, H. Siegbahn, L. Asplund, P. Kelfve, and K. Siegbahn, "ESCA applied to liquids IV. A wire system for ESCA measurements on liquids," *Journal of Electron Spectroscopy and Related Phenomena*, vol. 7, no. 5, pp. 421–428, 1975.

- [73] U. Gelius, “Recent progress in ESCA studies of gases,” *Journal of Electron Spectroscopy and Related Phenomena*, vol. 5, no. 1, pp. 985–1057, 1974.
- [74] A. Fahlman, C. Nordling, and K. Siegbahn, *ESCA: Atomic, molecular and solid state structure studied by means of electron spectroscopy*. Uppsala : Almqvist and Wiksell, 1967.
- [75] H. Siegbahn and K. Siegbahn, “ESCA applied to liquids,” *Journal of Electron Spectroscopy and Related Phenomena*, vol. 2, no. 3, pp. 319–325, 1973.
- [76] I. Lindgren and J. Morrison, *The Independent-Particle Model*, book section Chapter 5, pp. 103–115. Berlin, Heidelberg: Springer Berlin Heidelberg, 1986.
- [77] L. Hedin and J. D. Lee, “Sudden approximation in photoemission and beyond,” *Journal of Electron Spectroscopy and Related Phenomena*, vol. 124, no. 2-3, pp. 289–315, 2002.
- [78] K. T. Hecht, *Sudden and Adiabatic Approximations*, book section Chapter 59, pp. 561–571. Graduate Texts in Contemporary Physics, New York, NY: Springer New York, 2000.
- [79] Space Environment Technologies, *ISO 21348 Definitions of Solar Irradiance Spectral Categories*. [http://www.spacewx.com/pdf/SET\\_21348\\_2004.pdf](http://www.spacewx.com/pdf/SET_21348_2004.pdf), Online accessed: November 22, 2018.
- [80] M. Born and R. Oppenheimer, “Zur Quantentheorie der Molekeln,” *Annalen der Physik*, vol. 389, no. 20, pp. 457–484, 1927.
- [81] M. Schultze, M. Fiess, N. Karpowicz, J. Gagnon, M. Korbman, M. Hofstetter, S. Neppl, A. L. Cavalieri, Y. Komninos, T. Mercouris, C. A. Nicolaides, R. Pazourek, S. Nagele, J. Feist, J. Burgdorfer, A. M. Azzeer, R. Ernstorfer, R. Kienberger, U. Kleineberg, E. Goulielmakis, F. Krausz, and V. S. Yakovlev, “Delay in photoemission,” *Science*, vol. 328, no. 5986, pp. 1658–1662, 2010.
- [82] M. F. Kling and M. J. Vrakking, “Attosecond electron dynamics,” *Annual Review of Physical Chemistry*, vol. 59, pp. 463–492, 2008.

- [83] Y. Dou, B. R. Torralva, and R. E. Allen, "Interplay of electronic and nuclear degrees of freedom in a femtosecond-scale photochemical reaction," *Chemical Physics Letters*, vol. 392, no. 4-6, pp. 352–357, 2004.
- [84] A. H. Zewail, "Femtochemistry: Atomic-scale dynamics of the chemical bond," *The Journal of Physical Chemistry A*, vol. 104, no. 24, pp. 5660–5694, 2000.
- [85] A. L. Ankudinov, W. T. Elam, J. R. Sieber, and J. J. Rehr, "Chemical speciation via x-ray emission spectra," *X-Ray Spectrometry*, vol. 35, no. 5, pp. 312–318, 2006.
- [86] P. L. Geissler, C. Dellago, D. Chandler, J. Hutter, and M. Parrinello, "Autoionization in liquid water," *Science*, vol. 291, no. 5511, pp. 2121–2124, 2001.
- [87] P. Natalis, P. Pennetreau, L. Longton, and J. E. Collin, "Autoionization in HCl and DCl by photoelectron spectroscopy," *Chemical Physics*, vol. 73, no. 1-2, pp. 191–201, 1982.
- [88] M. Eigen and L. Demaeyer, "Untersuchungen über die Kinetik der Neutralisation," *Zeitschrift für Elektrochemie*, vol. 59, no. 10, pp. 986–993, 1955.
- [89] L. Meitner, "Über die  $\beta$ -Strahl-Spektren und ihren Zusammenhang mit der  $\gamma$ -Strahlung," *Zeitschrift für Physik*, vol. 11, no. 1, pp. 35–54, 1922.
- [90] P. Auger, "Sur l'effet photoélectrique composé," *Journal de Physique et le Radium*, vol. 6, no. 6, pp. 205–208, 1925.
- [91] E. H. S. Burhop, "The Auger effect," *Proceedings of the Royal Society A: Mathematical, Physical and Engineering Sciences*, vol. 148, no. 864, pp. 272–284, 1935.
- [92] P. Palmberg and P. E. Industries, *Handbook of Auger Electron Spectroscopy: A Reference Book of Standard Data for Identification and Interpretation of Auger Electron Spectroscopy Data*. Physical Electronics Industries, 1972.

- [93] J. Stepanek, "Methods to determine the fluorescence and Auger spectra due to decay of radionuclides or due to a single atomic-subshell ionization and comparisons with experiments," *Medical Physics*, vol. 27, no. 7, pp. 1544–1554, 2000.
- [94] M. O. Krause and J. H. Oliver, "Natural widths of atomic K and L levels,  $K\alpha$  x-ray lines and several KLL Auger lines," *Journal of Physical and Chemical Reference Data*, vol. 8, no. 2, pp. 329–338, 1979.
- [95] T. X. Carroll, J. Hahne, T. D. Thomas, L. J. Sæthre, N. Berrah, J. Bozek, and E. Kukk, "Carbon 1s core-hole lifetime in  $\text{CO}_2$ ," *Physical Review A*, vol. 61, no. 4, 2000.
- [96] B. Kempgens, A. Kivimäki, M. Neeb, H. M. Köppe, A. M. Bradshaw, and J. Feldhaus, "A high-resolution n 1s photoionization study of the molecule in the near-threshold region," *Journal of Physics B: Atomic, Molecular and Optical Physics*, vol. 29, no. 22, pp. 5389–5402, 1996.
- [97] I. Hjelte, M. N. Piancastelli, R. F. Fink, O. Björneholm, M. Bäessler, R. Feifel, A. Giertz, H. Wang, K. Wiesner, A. Ausmees, C. Miron, S. L. Sorensen, and S. Svensson, "Evidence for ultra-fast dissociation of molecular water from resonant Auger spectroscopy," *Chemical Physics Letters*, vol. 334, no. 1-3, pp. 151–158, 2001.
- [98] P. A. Brühwiler, O. Karis, and N. Mårtensson, "Charge-transfer dynamics studied using resonant core spectroscopies," *Reviews of Modern Physics*, vol. 74, no. 3, pp. 703–740, 2002.
- [99] O. Björneholm, A. Nilsson, A. Sandell, B. Hernnas, and N. Mårtensson, "Determination of time scales for charge-transfer screening in physisorbed molecules," *Physical Review Letters*, vol. 68, no. 12, pp. 1892–1895, 1992.
- [100] V. Buch, "Molecular structure and oh-stretch spectra of liquid water surface," *Journal of Physical Chemistry B*, vol. 109, no. 38, pp. 17771–17774, 2005.

- [101] R. Santra, J. Zobeley, and L. Cederbaum, "Electronic decay of valence holes in clusters and condensed matter," *Physical Review B*, vol. 64, no. 24, 2001.
- [102] U. Hergenhahn, "Interatomic and intermolecular Coulombic decay: The early years," *Journal of Electron Spectroscopy and Related Phenomena*, vol. 184, no. 3-6, pp. 78–90, 2011.
- [103] R. Golnak, S. I. Bokarev, R. Seidel, J. Xiao, G. Grell, K. Atak, I. Unger, S. Thürmer, S. G. Aziz, O. Kuhn, B. Winter, and E. F. Aziz, "Joint analysis of radiative and non-radiative electronic relaxation upon x-ray irradiation of transition metal aqueous solutions," *Scientific Reports*, vol. 6, p. 24659, 2016.
- [104] J.-E. Rubensson, "RIXS dynamics for beginners," *Journal of Electron Spectroscopy and Related Phenomena*, vol. 110-111, pp. 135–151, 2000.
- [105] G. B. Armen, H. Aksela, T. Åberg, and S. Aksela, "The resonant Auger effect," *Journal of Physics B: Atomic, Molecular and Optical Physics*, vol. 33, no. 2, pp. R49–R92, 2000.
- [106] C. Guillot, Y. Ballu, J. Paigné, J. Lecante, K. P. Jain, P. Thiry, R. Pinchaux, Y. Pétrouff, and L. M. Falicov, "Resonant photoemission in nickel metal," *Physical Review Letters*, vol. 39, no. 25, pp. 1632–1635, 1977.
- [107] S. Thürmer, R. Seidel, W. Eberhardt, S. E. Bradforth, and B. Winter, "Ultrafast hybridization screening in  $\text{Fe}^{3+}$  aqueous solution," *Journal of the American Chemical Society*, vol. 133, no. 32, pp. 12528–12535, 2011.
- [108] U. Fano, "Effects of configuration interaction on intensities and phase shifts," *Physical Review*, vol. 124, no. 6, pp. 1866–1878, 1961.
- [109] H. Ali, R. Seidel, M. N. Pohl, and B. Winter, "Molecular species forming at the  $\alpha\text{-Fe}_2\text{O}_3$  nanoparticle–aqueous solution interface," *Chemical Science*, 2018.
- [110] T. Jahnke, "Interatomic and intermolecular Coulombic decay: the coming of age story," *Journal of Physics B: Atomic, Molecular and Optical Physics*, vol. 48, no. 8, 2015.

- [111] S. De Liberato, “Virtual photons in the ground state of a dissipative system,” *Nature Communication*, vol. 8, no. 1, p. 1465, 2017.
- [112] D. L. Andrews and D. S. Bradshaw, “Virtual photons, dipole fields and energy transfer: A quantum electrodynamical approach,” *European Journal of Physics*, vol. 25, no. 6, pp. 845–858, 2004.
- [113] R. Santra and L. S. Cederbaum, “Non-hermitian electronic theory and applications to clusters,” *Physics Reports*, vol. 368, no. 1, pp. 1–117, 2002.
- [114] T. Förster, “Zwischenmolekulare Energiewanderung und Fluoreszenz,” *Annalen der Physik*, vol. 437, no. 1-2, pp. 55–75, 1948.
- [115] S. Marburger, O. Kugeler, U. Hergenhahn, and T. Moller, “Experimental evidence for interatomic Coulombic decay in Ne clusters,” *Physical Review Letters*, vol. 90, no. 20, p. 203401, 2003.
- [116] T. Havermeier, T. Jahnke, K. Kreidi, R. Wallauer, S. Voss, M. Schoffler, S. Schossler, L. Foucar, N. Neumann, J. Titze, H. Sann, M. Kuhnel, J. Voigtsberger, J. H. Morilla, W. Schollkopf, H. Schmidt-Bocking, R. E. Grisenti, and R. Dörner, “Interatomic Coulombic decay following photoionization of the helium dimer: Observation of vibrational structure,” *Physical Review Letters*, vol. 104, no. 13, p. 133401, 2010.
- [117] T. Jahnke, H. Sann, T. Havermeier, K. Kreidi, C. Stuck, M. Meckel, M. Schöffler, N. Neumann, R. Wallauer, S. Voss, A. Czasch, O. Jagutzki, A. Malakzadeh, F. Afaneh, T. Weber, H. Schmidt-Böcking, and R. Dörner, “Ultrafast energy transfer between water molecules,” *Nature Physics*, vol. 6, no. 2, pp. 139–142, 2010.
- [118] L. S. Cederbaum, J. Zobeley, and F. Tarantelli, “Giant intermolecular decay and fragmentation of clusters,” *Physical Review Letters*, vol. 79, no. 24, pp. 4778–4781, 1997.

- [119] E. F. Aziz, N. Ottosson, M. Faubel, I. V. Hertel, and B. Winter, "Interaction between liquid water and hydroxide revealed by core-hole de-excitation," *Nature*, vol. 455, no. 7209, pp. 89–91, 2008.
- [120] W. Pokapanich, N. V. Kryzhevoi, N. Ottosson, S. Svensson, L. S. Cederbaum, G. Öhrwall, and O. Björneholm, "Ionic-charge dependence of the intermolecular Coulombic decay time scale for aqueous ions probed by the core-hole clock," *Journal of the American Chemical Society*, vol. 133, no. 34, pp. 13430–13436, 2011.
- [121] W. Pokapanich, N. Ottosson, S. Svensson, G. Öhrwall, B. Winter, and O. Björneholm, "Bond breaking, electron pushing, and proton pulling: Active and passive roles in the interaction between aqueous ions and water as manifested in the o 1s Auger decay," *Journal of Physical Chemistry B*, vol. 116, no. 1, pp. 3–8, 2012.
- [122] I. Unger, R. Seidel, S. Thürmer, M. N. Pohl, E. F. Aziz, L. S. Cederbaum, E. Muchova, P. Slavíček, B. Winter, and N. V. Kryzhevoi, "Observation of electron-transfer-mediated decay in aqueous solution," *Nature Chemistry*, vol. 9, no. 7, pp. 708–714, 2017.
- [123] C. Buth, R. Santra, and L. S. Cederbaum, "Impact of interatomic electronic decay processes on Xe 4d hole decay in the xenon fluorides," *The Journal of Chemical Physics*, vol. 119, no. 20, pp. 10575–10584, 2003.
- [124] J. Zobeley, R. Santra, and L. S. Cederbaum, "Electronic decay in weakly bound heteroclusters: Energy transfer versus electron transfer," *The Journal of Chemical Physics*, vol. 115, no. 11, pp. 5076–5088, 2001.
- [125] M. Pernpointner, N. V. Kryzhevoi, and S. Urbaczek, "Possible electronic decay channels in the ionization spectra of small clusters composed of Ar and Kr: A four-component relativistic treatment," *Journal of Chemical Physics*, vol. 129, no. 2, p. 024304, 2008.



- [126] I. B. Müller and L. S. Cederbaum, “Electronic decay following ionization of aqueous  $\text{Li}^+$  microsolvation clusters,” *Journal of Chemical Physics*, vol. 122, no. 9, p. 094305, 2005.
- [127] M. N. Pohl, C. Richter, E. Lugovoy, R. Seidel, P. Slavíček, E. F. Aziz, B. Abel, B. Winter, and U. Hergenhan, “Sensitivity of electron transfer mediated decay to ion pairing,” *Journal of Physical Chemistry B*, vol. 121, no. 32, pp. 7709–7714, 2017.
- [128] E. Fermi, “High energy nuclear events,” *Progress of Theoretical Physics*, vol. 5, no. 4, pp. 570–583, 1950.
- [129] N. Ottosson, M. Faubel, S. E. Bradforth, P. Jungwirth, and B. Winter, “Photoelectron spectroscopy of liquid water and aqueous solution: Electron effective attenuation lengths and emission-angle anisotropy,” *Journal of Electron Spectroscopy and Related Phenomena*, vol. 177, no. 2-3, pp. 60–70, 2010.
- [130] M. S. Lubell and W. Raith, “Polarization effect in photoionization of cesium,” *Physical Review Letters*, vol. 23, no. 5, pp. 211–214, 1969.
- [131] R. A. Fox, R. M. Kogan, and E. J. Robinson, “Laser triple-quantum photoionization of cesium,” *Physical Review Letters*, vol. 26, no. 23, pp. 1416–1417, 1971.
- [132] C. H. Li and D. Budker, “Polarization-dependent photoionization cross sections and radiative lifetimes of atomic states in BaI,” *Physical Review A*, vol. 74, no. 1, 2006.
- [133] M. P. Seah and W. A. Dench, “Quantitative electron spectroscopy of surfaces: A standard data base for electron inelastic mean free paths in solids,” *Surface and Interface Analysis*, vol. 1, no. 1, pp. 2–11, 1979.
- [134] A. Beer, “Bestimmung der Absorption des rothen Lichts in farbigen Flüssigkeiten,” *Annalen der Physik*, vol. 162, pp. 78–88, 1852.

- [135] A. Jablonski and C. J. Powell, “Relationships between electron inelastic mean free paths, effective attenuation lengths, and mean escape depths,” *Journal of Electron Spectroscopy and Related Phenomena*, vol. 100, no. 1-3, pp. 137–160, 1999.
- [136] R. Seidel, B. Winter, and S. E. Bradforth, “Valence electronic structure of aqueous solutions: Insights from photoelectron spectroscopy,” *Annual Review of Physical Chemistry*, vol. 67, pp. 283–305, 2016.
- [137] S. Thürmer, R. Seidel, M. Faubel, W. Eberhardt, J. C. Hemminger, S. E. Bradforth, and B. Winter, “Photoelectron angular distributions from liquid water: Effects of electron scattering,” *Physical Review Letters*, vol. 111, no. 17, p. 173005, 2013.
- [138] Y. Suzuki, K. Nishizawa, N. Kurahashi, and T. Suzuki, “Effective attenuation length of an electron in liquid water between 10 and 600 eV,” *Physical review E, Statistical, nonlinear, and soft matter physics*, vol. 90, no. 1, p. 010302, 2014.
- [139] J. Stöhr, *NEXAFS Spectroscopy*, vol. 25 of *Springer Series in Surface Sciences*. Berlin Heidelberg: Springer-Verlag, 1 ed., 1992.
- [140] J. V. G. R. Tsuji, Kouichi; Injuk, ed., *X-Ray Spectrometry: Recent Technological Advances*. John Wiley and Sons, Ltd, 2004.
- [141] A. Muñoz, J. C. Oiler, F. Blanco, J. D. Gorfinkiel, P. Limão-Vieira, A. Maira-Vidal, M. J. G. Borge, O. Tengblad, C. Hueriga, M. Téllez, and G. García, “Energy deposition model based on electron scattering cross section data from water molecules,” *Journal of Physics: Conference Series*, vol. 133, 2008.
- [142] Y. Itikawa and N. Mason, “Cross sections for electron collisions with water molecules,” *Journal of Physical and Chemical Reference Data*, vol. 34, no. 1, pp. 1–22, 2005.
- [143] I. Plante and F. A. Cucinotta, “Cross sections for the interactions of 1 eV–100 MeV electrons in liquid water and application to monte-carlo simulation of hze radiation tracks,” *New Journal of Physics*, vol. 11, no. 6, 2009.

- [144] B. Winter, “Interfaces: Scientists strike wet gold,” *Nature Chemistry*, vol. 7, no. 3, pp. 192–194, 2015.
- [145] M. Faubel, S. Schlemmer, and J. P. Toennies, “A molecular beam study of the evaporation of water from a liquid jet,” *Zeitschrift für Physik D Atoms, Molecules and Clusters*, vol. 10, no. 2-3, pp. 269–277, 1988.
- [146] M. Faubel, B. Steiner, and J. P. Toennies, “Photoelectron spectroscopy of liquid water, some alcohols, and pure nonane in free micro jets,” *The Journal of Chemical Physics*, vol. 106, no. 22, pp. 9013–9031, 1997.
- [147] K. R. Wilson, B. S. Rude, T. Catalano, R. D. Schaller, J. G. Tobin, D. T. Co, and R. J. Saykally, “X-ray spectroscopy of liquid water microjets,” *The Journal of Physical Chemistry B*, vol. 105, no. 17, pp. 3346–3349, 2001.
- [148] K. R. Wilson, B. S. Rude, J. Smith, C. Cappa, D. T. Co, R. D. Schaller, M. Larsson, T. Catalano, and R. J. Saykally, “Investigation of volatile liquid surfaces by synchrotron x-ray spectroscopy of liquid microjets,” *Review of Scientific Instruments*, vol. 75, no. 3, pp. 725–736, 2004.
- [149] R. Al-Obaidi, M. Wilke, M. Borgwardt, J. Metje, A. Moguelevski, N. Engel, D. Tolksdorf, A. Raheem, T. Kampen, S. Mähl, I. Y. Kiyan, and E. F. Aziz, “Ultrafast photoelectron spectroscopy of solutions: Space-charge effect,” *New Journal of Physics*, vol. 17, no. 9, 2015.
- [150] J. Metje, M. Borgwardt, A. Moguelevski, A. Kothe, N. Engel, M. Wilke, R. Al-Obaidi, D. Tolksdorf, A. Firsov, M. Brzhezinskaya, A. Erko, I. Y. Kiyan, and E. F. Aziz, “Monochromatization of femtosecond XUV light pulses with the use of reflection zone plates,” *Optics Express*, vol. 22, no. 9, pp. 10747–10760, 2014.
- [151] O. Kornilov, C. Wang, O. Bünermann, A. Healy, M. Leonard, C. Peng, S. Leone, D. M. Neumark, and O. Gessner, “Ultrafast dynamics in helium nanodroplets probed by femtosecond time-resolved EUV photoelectron imaging,” *Journal of Physical Chemistry A*, vol. 114, 2010.

- [152] T. Popmintchev, M. C. Chen, D. Popmintchev, P. Arpin, S. Brown, S. Alisauskas, G. Andriukaitis, T. Balciunas, O. D. Mucke, A. Pugzlys, A. Baltuska, B. Shim, S. E. Schrauth, A. Gaeta, C. Hernandez-Garcia, L. Plaja, A. Becker, A. Jaron-Becker, M. M. Murnane, and H. C. Kapteyn, “Bright coherent ultrahigh harmonics in the keV x-ray regime from mid-infrared femtosecond lasers,” *Science*, vol. 336, no. 6086, pp. 1287–1291, 2012.
- [153] D. E. Grider, A. Wright, and P. K. Ausburn, “Electron beam melting in microfocus x-ray tubes,” *Journal of Physics D: Applied Physics*, vol. 19, no. 12, pp. 2281–2292, 1986.
- [154] J. Als-Nielsen and D. McMorrow, *Elements of Modern X-ray Physics*. Wiley, 2011.
- [155] G. Rosenbaum, K. C. Holmes, and J. Witz, “Synchrotron radiation as a source for x-ray diffraction,” *Nature*, vol. 230, no. 5294, pp. 434–437, 1971.
- [156] J. Schwinger, “On the classical radiation of accelerated electrons,” *Physical Review*, vol. 75, no. 12, pp. 1912–1925, 1949.
- [157] B. J. Eastlund, “Low mode coherent synchrotron radiation and pulsar phenomena,” *Nature*, vol. 225, no. 5231, pp. 430–434, 1970.
- [158] T. Kachel, “The plane grating monochromator beamline U49-2 PGM-1 at BESSY II,” *Journal of Large-Scale Research Facilities*, vol. 2, 2016.
- [159] M. R. Weiss, R. Follath, F. Senf, and W. Gudat, “Comparative monochromator studies for a soft x-ray microfocus beamline for BESSY II,” *Journal of Electron Spectroscopy and Related Phenomena*, vol. 101-103, pp. 1003–1012, 1999.
- [160] H. Wiedemann, *Synchrotron Radiation*. Springer, 2003.
- [161] H. Kamitsubo, “8 GeV synchrotron radiation facility project in japan: JAERI-RIKEN SPring-8 project,” *Nuclear Instruments and Methods in Physics Research Section A: Accelerators, Spectrometers, Detectors and Associated Equipment*, vol. 303, no. 3, pp. 421–434, 1991.

- [162] A. C. Thompson, D. T. Attwood, E. M. Gullikson, M. R. Howells, J. B. Kortright, A. L. Robinson, J. H. Underwood, K.-J. Kim, J. Kirz, P. P. Ingolf Lindau, H. Winick, G. P. Williams, and J. H. Scofield, *X-ray Data Booklet*. 2001.
- [163] M. N. Pohl, *Study of the electronic structure of transition metal porphyrin: X-ray absorption and emission*. Master thesis, 2014.
- [164] P. Schmüser, M. Dohlus, J. Rossbach, and C. Behrens, *Free-Electron Lasers in the Ultraviolet and X-Ray Regime: Physical Principles, Experimental Results, Technical Realization*. Springer International Publishing, 2014.
- [165] N. Preissler, F. Buchner, T. Schultz, and A. Lubcke, “Electrokinetic charging and evidence for charge evaporation in liquid microjets of aqueous salt solution,” *Journal of Physical Chemistry B*, vol. 117, no. 8, pp. 2422–2428, 2013.
- [166] N. Kurahashi, S. Karashima, Y. Tang, T. Horio, B. Abulimiti, Y. Suzuki, Y. Ogi, M. Oura, and T. Suzuki, “Photoelectron spectroscopy of aqueous solutions: Streaming potentials of NaX (X = Cl, Br, and I) solutions and electron binding energies of liquid water and X,” *Journal of Chemical Physics*, vol. 140, no. 17, p. 174506, 2014.
- [167] D. N. Kelly, R. K. Lam, A. M. Duffin, and R. J. Saykally, “Exploring solid/aqueous interfaces with ultradilute electrokinetic analysis of liquid microjets,” *The Journal of Physical Chemistry C*, vol. 117, no. 24, pp. 12702–12706, 2013.
- [168] S. Chen, T. W. Goh, D. Sabba, J. Chua, N. Mathews, C. H. A. Huan, and T. C. Sum, “Energy level alignment at the methylammonium lead iodide/copper phthalocyanine interface,” *APL Materials*, vol. 2, no. 8, 2014.
- [169] P. Kruit and F. H. Read, “Magnetic field paralleliser for  $2\pi$  electron-spectrometer and electron-image magnifier,” *Journal of Physics E: Scientific Instruments*, vol. 16, no. 4, p. 313, 1983.

- [170] M. Mucke, M. Forstel, T. Lischke, T. Arion, A. M. Bradshaw, and U. Hergenbahn, "Performance of a short 'magnetic bottle' electron spectrometer," *Review of Scientific Instruments*, vol. 83, no. 6, p. 063106, 2012.
- [171] M. Förstel, *Investigation of non-local autoionization processes in rare gas clusters*. Doctoral thesis, 2012.
- [172] P. Hunt, *Molecular Orbitals and Population Analysis*.  
[http://www.huntresearchgroup.org.uk/teaching/teaching\\_comp\\_chem\\_year4/L7\\_bonding.pdf](http://www.huntresearchgroup.org.uk/teaching/teaching_comp_chem_year4/L7_bonding.pdf), 2008, Online accessed: November 22, 2018.
- [173] M. S. Banna, B. H. McQuaide, R. Malutzki, and V. Schmidt, "The photoelectron spectrum of water in the 30 to 140 eV photon energy range," *The Journal of Chemical Physics*, vol. 84, no. 9, pp. 4739–4744, 1986.
- [174] R. Sankari, M. Ehara, H. Nakatsuji, Y. Senba, K. Hosokawa, H. Yoshida, A. De Fanis, Y. Tamenori, S. Aksela, and K. Ueda, "Vibrationally resolved O 1s photoelectron spectrum of water," *Chemical Physics Letters*, vol. 380, no. 5-6, pp. 647–653, 2003.
- [175] S. Y. Truong, A. J. Yench, A. M. Juarez, S. J. Cavanagh, P. Bolognesi, and G. C. King, "Threshold photoelectron spectroscopy of H<sub>2</sub>O and D<sub>2</sub>O over the photon energy range 12–40 eV," *Chemical Physics*, vol. 355, no. 2-3, pp. 183–193, 2009.
- [176] S. Barth, M. Ončák, V. Ulrich, M. Mucke, T. Lischke, P. Slavíček, and U. Hergenbahn, "Valence ionization of water clusters: From isolated molecules to bulk," *The Journal of Physical Chemistry A*, vol. 113, no. 48, pp. 13519–13527, 2009.
- [177] D. Hollas, E. Muchova, and P. Slavíček, "Modeling liquid photoemission spectra: Path-integral molecular dynamics combined with tuned range-separated hybrid functionals," *Journal of Chemical Theory and Computation*, 2016.
- [178] A. P. Gaiduk, M. Govoni, R. Seidel, J. H. Skone, B. Winter, and G. Galli, "Photoelectron spectra of aqueous solutions from first principles," *Journal of the American Chemical Society*, vol. 138, no. 22, pp. 6912–6915, 2016.

- [179] D. Nordlund, M. Odelius, H. Bluhm, H. Ogasawara, L. G. M. Pettersson, and A. Nilsson, "Electronic structure effects in liquid water studied by photoelectron spectroscopy and density functional theory," *Chemical Physics Letters*, vol. 460, no. 1-3, pp. 86–92, 2008.
- [180] K. Nishizawa, N. Kurahashi, K. Sekiguchi, T. Mizuno, Y. Ogi, T. Horio, M. Oura, N. Kosugi, and T. Suzuki, "High-resolution soft x-ray photoelectron spectroscopy of liquid water," *Physical Chemistry Chemical Physics*, vol. 13, no. 2, pp. 413–417, 2011.
- [181] J. Guo and Y. Luo, "Molecular structure in water and solutions studied by photon-in/photon-out soft x-ray spectroscopy," *Journal of Electron Spectroscopy and Related Phenomena*, vol. 177, no. 2-3, pp. 181–191, 2010.
- [182] M. Pohl, E. Muchova, R. Seidel, H. Ali, S. Sršen, I. Wilkinson, B. Winter, and P. Slavíček, "Do water's electrons care of electrolytes?," *Submitted to Chemical Science*, 2018.
- [183] J. Kovac, "Cathedrals of science: The personalities and rivalries that made modern chemistry (patrick coffey)," *Journal of Chemical Education*, vol. 86, no. 3, 2009.
- [184] L. G. Pettersson, R. H. Henchman, and A. Nilsson, "Water-the most anomalous liquid," *Chemical Reviews*, vol. 116, no. 13, pp. 7459–7462, 2016.
- [185] P. Wernet, D. Nordlund, U. Bergmann, M. Cavalleri, M. Odelius, H. Ogasawara, L. A. Naslund, T. K. Hirsch, L. Ojamae, P. Glatzel, L. G. Pettersson, and A. Nilsson, "The structure of the first coordination shell in liquid water," *Science*, vol. 304, no. 5673, pp. 995–999, 2004.
- [186] J. D. Smith, C. D. Cappa, K. R. Wilson, B. M. Messer, R. C. Cohen, and R. J. Saykally, "Energetics of hydrogen bond network rearrangements in liquid water," *Science*, vol. 306, no. 5697, pp. 851–853, 2004.
- [187] C. Huang, K. T. Wikfeldt, T. Tokushima, D. Nordlund, Y. Harada, U. Bergmann, M. Niebuhr, T. M. Weiss, Y. Horikawa, M. Leetmaa, M. P.

- Ljungberg, O. Takahashi, A. Lenz, L. Ojamae, A. P. Lyubartsev, S. Shin, L. G. Pettersson, and A. Nilsson, "The inhomogeneous structure of water at ambient conditions," *Proceedings of the National Academy of Sciences of the United States of America*, vol. 106, no. 36, pp. 15214–15218, 2009.
- [188] T. D. Kühne and R. Z. Khaliullin, "Electronic signature of the instantaneous asymmetry in the first coordination shell of liquid water," *Nature Communication*, vol. 4, p. 1450, 2013.
- [189] Y. Harada, J. Miyawaki, H. Niwa, K. Yamazoe, L. G. M. Pettersson, and A. Nilsson, "Probing the OH stretch in different local environments in liquid water," *The Journal of Physical Chemistry Letters*, vol. 8, no. 22, pp. 5487–5491, 2017.
- [190] H. J. Bakker, "Structural dynamics of aqueous salt solutions," *Chemical Reviews*, vol. 108, no. 4, pp. 1456–1473, 2008.
- [191] R. Weber, B. Winter, P. M. Schmidt, W. Widdra, I. V. Hertel, M. Dittmar, and M. Faubel, "Photoemission from aqueous alkali-metal–iodide salt solutions using EUV synchrotron radiation," *The Journal of Physical Chemistry B*, vol. 108, no. 15, pp. 4729–4736, 2004.
- [192] E. Pluharova, P. Slavíček, and P. Jungwirth, "Modeling photoionization of aqueous DNA and its components," *Accounts of Chemical Research*, vol. 48, no. 5, pp. 1209–1217, 2015.
- [193] P. Slavíček, B. Winter, M. Faubel, S. E. Bradforth, and P. Jungwirth, "Ionization energies of aqueous nucleic acids: Photoelectron spectroscopy of pyrimidine nucleosides and ab initio calculations," *Journal of the American Chemical Society*, vol. 131, no. 18, pp. 6460–6467, 2009.
- [194] C. A. Schroeder, E. Pluhařová, R. Seidel, W. P. Schroeder, M. Faubel, P. Slavíček, B. Winter, P. Jungwirth, and S. E. Bradforth, "Oxidation half-reaction of aqueous nucleosides and nucleotides via photoelectron spectroscopy augmented



- by ab initio calculations,” *Journal of the American Chemical Society*, vol. 137, no. 1, pp. 201–209, 2014.
- [195] E. Pluhařová, C. Schroeder, R. Seidel, S. E. Bradforth, B. Winter, M. Faubel, P. Slavíček, and P. Jungwirth, “Unexpectedly small effect of the DNA environment on vertical ionization energies of aqueous nucleobases,” *The Journal of Physical Chemistry Letters*, vol. 4, no. 21, pp. 3766–3769, 2013.
- [196] E. Pluharova, P. Jungwirth, S. E. Bradforth, and P. Slavíček, “Ionization of purine tautomers in nucleobases, nucleosides, and nucleotides: From the gas phase to the aqueous environment,” *Journal of Physical Chemistry B*, vol. 115, no. 5, pp. 1294–1305, 2011.
- [197] P. Debye and E. Hückel, “De la theorie des electrolytes. I. abaissement du point de congelation et phenomenes associes,” *Physikalische Zeitschrift*, vol. 24, no. 9, pp. 185–206, 1923.
- [198] I. Waluyo, D. Nordlund, U. Bergmann, D. Schlesinger, L. G. Pettersson, and A. Nilsson, “A different view of structure-making and structure-breaking in alkali halide aqueous solutions through x-ray absorption spectroscopy,” *Journal of Chemical Physics*, vol. 140, no. 24, p. 244506, 2014.
- [199] Y. L. Jeyachandran, F. Meyer, S. Nagarajan, A. Benkert, M. Bar, M. Blum, W. Yang, F. Reinert, C. Heske, L. Weinhardt, and M. Zharnikov, “Ion-solvation-induced molecular reorganization in liquid water probed by resonant inelastic soft x-ray scattering,” *The Journal of Physical Chemistry Letters*, vol. 5, no. 23, pp. 4143–4148, 2014.
- [200] Z. Yin, L. Inhester, S. Thekku Veedu, W. Quevedo, A. Pietzsch, P. Wernet, G. Groenhof, A. Fohlisch, H. Grubmuller, and S. Techert, “Cationic and anionic impact on the electronic structure of liquid water,” *The Journal of Physical Chemistry Letters*, vol. 8, no. 16, pp. 3759–3764, 2017.

- [201] L. Suo, O. Borodin, T. Gao, M. Olguin, J. Ho, X. Fan, C. Luo, C. Wang, and K. Xu, “‘water-in-salt’ electrolyte enables high-voltage aqueous lithium-ion chemistries,” *Science*, vol. 350, no. 6263, pp. 938–943, 2015.
- [202] Y. Yamada, K. Usui, K. Sodeyama, S. Ko, Y. Tateyama, and A. Yamada, “Hydrate-melt electrolytes for high-energy-density aqueous batteries,” *Nature Energy*, vol. 1, no. 10, 2016.
- [203] R.-S. Kühnel, D. Reber, and C. Battaglia, “A high-voltage aqueous electrolyte for sodium-ion batteries,” *ACS Energy Letters*, vol. 2, no. 9, pp. 2005–2006, 2017.
- [204] A. M. Smith, A. A. Lee, and S. Perkin, “The electrostatic screening length in concentrated electrolytes increases with concentration,” *The Journal of Physical Chemistry Letters*, vol. 7, no. 12, pp. 2157–2163, 2016.
- [205] A. A. Lee, C. S. Perez-Martinez, A. M. Smith, and S. Perkin, “Underscreening in concentrated electrolytes,” *Faraday Discussions*, vol. 199, pp. 239–259, 2017.
- [206] K. A. Perrine, M. H. C. Van Spyk, A. M. Margarella, B. Winter, M. Faubel, H. Bluhm, and J. C. Hemminger, “Characterization of the acetonitrile aqueous solution/vapor interface by liquid-jet x-ray photoelectron spectroscopy,” *The Journal of Physical Chemistry C*, vol. 118, no. 50, pp. 29378–29388, 2014.
- [207] T. Lewis, M. Faubel, B. Winter, and J. C. Hemminger, “CO<sub>2</sub> capture in amine-based aqueous solution: Role of the gas-solution interface,” *Angewandte Chemie International Edition*, vol. 50, no. 43, pp. 10178–10181, 2011.
- [208] T. Lewis, B. Winter, A. C. Stern, M. D. Baer, C. J. Mundy, D. J. Tobias, and J. C. Hemminger, “Does nitric acid dissociate at the aqueous solution surface?,” *The Journal of Physical Chemistry C*, vol. 115, no. 43, pp. 21183–21190, 2011.
- [209] B. Winter, R. Weber, P. M. Schmidt, I. V. Hertel, M. Faubel, L. Vrbka, and P. Jungwirth, “Molecular structure of surface-active salt solutions: Photoelectron spectroscopy and molecular dynamics simulations of aqueous tetrabutylammonium iodide,” *The Journal of Physical Chemistry B*, vol. 108, no. 38, pp. 14558–14564, 2004.

- [210] P. Jungwirth and D. J. Tobias, "Specific ion effects at the air/water interface," *Chemical Reviews*, vol. 106, no. 4, pp. 1259–1281, 2006.
- [211] N. Ottosson, J. Heyda, E. Wernersson, W. Pokapanich, S. Svensson, B. Winter, G. Öhrwall, P. Jungwirth, and O. Björneholm, "The influence of concentration on the molecular surface structure of simple and mixed aqueous electrolytes," *Physical Chemistry Chemical Physics*, vol. 12, no. 36, pp. 10693–10700, 2010.
- [212] S. P. Kowalczyk, F. R. McFeely, L. Ley, R. A. Pollak, and D. A. Shirley, "X-ray photoemission studies of the alkali halides," *Physical Review B*, vol. 9, no. 8, pp. 3573–3581, 1974.
- [213] J.-J. Yeh, *Atomic calculation of photoionization cross-sections and asymmetry parameters*. Gordon and Breach Science Publ.; AT&T Bell Laboratories, 1993.
- [214] P. Jungwirth and D. J. Tobias, "Molecular structure of salt solutions: A new view of the interface with implications for heterogeneous atmospheric chemistry," *The Journal of Physical Chemistry B*, vol. 105, no. 43, pp. 10468–10472, 2001.
- [215] P. Jungwirth and D. J. Tobias, "Ions at the air/water interface," *The Journal of Physical Chemistry B*, vol. 106, no. 25, pp. 6361–6373, 2002.
- [216] D. Liu, G. Ma, L. M. Levering, and H. C. Allen, "Vibrational spectroscopy of aqueous sodium halide solutions and air–liquid interfaces: observation of increased interfacial depth," *The Journal of Physical Chemistry B*, vol. 108, no. 7, pp. 2252–2260, 2004.
- [217] B. Hess, H. Bekker, H. J. C. Berendsen, and J. G. E. M. Fraaije, "Lincs: A linear constraint solver for molecular simulations," *Journal of Computational Chemistry*, vol. 18, no. 12, pp. 1463–1472, 1997.
- [218] H. J. C. Berendsen, J. R. Grigera, and T. P. Straatsma, "The missing term in effective pair potentials," *Journal of Physical Chemistry*, vol. 91, no. 24, pp. 6269–6271, 1987.

- [219] I. S. Joung and T. E. Cheatham, "Determination of alkali and halide monovalent ion parameters for use in explicitly solvated biomolecular simulations," *The Journal of Physical Chemistry B*, vol. 112, no. 30, pp. 9020–9041, 2008.
- [220] M. Parrinello and A. Rahman, "Polymorphic transitions in single crystals: A new molecular dynamics method," *Journal of Applied Physics*, vol. 52, no. 12, pp. 7182–7190, 1981.
- [221] S. Nosé, "A molecular dynamics method for simulations in the canonical ensemble," *Molecular Physics*, vol. 52, no. 2, pp. 255–268, 2006.
- [222] W. G. Hoover, "Canonical dynamics: Equilibrium phase-space distributions," *Physical Review A*, vol. 31, no. 3, pp. 1695–1697, 1985.
- [223] B. Hess, C. Kutzner, D. van der Spoel, and E. Lindahl, "Gromacs 4: Algorithms for highly efficient, load-balanced, and scalable molecular simulation," *Journal of Chemical Theory and Computation*, vol. 4, no. 3, pp. 435–447, 2008.
- [224] U. Essmann, L. Perera, M. L. Berkowitz, T. Darden, H. Lee, and L. G. Pedersen, "A smooth particle mesh ewald method," *The Journal of Chemical Physics*, vol. 103, no. 19, pp. 8577–8593, 1995.
- [225] J. R. Errington and P. G. Debenedetti, "Relationship between structural order and the anomalies of liquid water," *Nature*, vol. 409, no. 6818, pp. 318–321, 2001.
- [226] P. L. Chau and A. J. Hardwick, "A new order parameter for tetrahedral configurations," *Molecular Physics*, vol. 93, no. 3, pp. 511–518, 2010.
- [227] M. Rubesova, E. Muchova, and P. Slavíček, "Optimal tuning of range-separated hybrids for solvated molecules with time-dependent density functional theory," *Journal of Chemical Theory and Computation*, vol. 13, no. 10, pp. 4972–4983, 2017.

- [228] F. E. Harris and C. T. Okonski, "Dielectric properties of aqueous ionic solutions at microwave frequencies," *Journal of Physical Chemistry*, vol. 61, no. 3, pp. 310–319, 1957.
- [229] J. B. Hasted, D. M. Ritson, and C. H. Collie, "Dielectric properties of aqueous ionic solutions. Parts I and II," *The Journal of Chemical Physics*, vol. 16, no. 1, pp. 1–21, 1948.
- [230] G. H. Haggis, J. B. Hasted, and T. J. Buchanan, "The dielectric properties of water in solutions," *The Journal of Chemical Physics*, vol. 20, no. 9, pp. 1452–1465, 1952.
- [231] R. Buchner, G. T. Hefter, and P. M. May, "Dielectric relaxation of aqueous NaCl solutions," *The Journal of Physical Chemistry A*, vol. 103, no. 1, pp. 1–9, 1999.
- [232] S. Ansell, A. C. Barnes, P. E. Mason, G. W. Neilson, and S. Ramos, "X-ray and neutron scattering studies of the hydration structure of alkali ions in concentrated aqueous solutions," *Biophysical Chemistry*, vol. 124, no. 3, pp. 171–179, 2006.
- [233] A. K. Soper and K. Weckstrom, "Ion solvation and water structure in potassium halide aqueous solutions," *Biophysical Chemistry*, vol. 124, no. 3, pp. 180–191, 2006.
- [234] M. Cossi, N. Rega, G. Scalmani, and V. Barone, "Energies, structures, and electronic properties of molecules in solution with the C-PCM solvation model," *Journal of Computational Chemistry*, vol. 24, no. 6, pp. 669–681, 2003.
- [235] V. Barone and M. Cossi, "Quantum calculation of molecular energies and energy gradients in solution by a conductor solvent model," *The Journal of Physical Chemistry A*, vol. 102, no. 11, pp. 1995–2001, 1998.
- [236] T. N. Truong and E. V. Stefanovich, "A new method for incorporating solvent effect into the classical, ab initio molecular orbital and density functional theory frameworks for arbitrary shape cavity," *Chemical Physics Letters*, vol. 240, no. 4, pp. 253–260, 1995.

- [237] J. D. Smith, R. J. Saykally, and P. L. Geissler, "The effects of dissolved halide anions on hydrogen bonding in liquid water," *Journal of the American Chemical Society*, vol. 129, no. 45, pp. 13847–13856, 2007.
- [238] Y. Wang and Y. Tominaga, "Dynamical structure of water in aqueous electrolyte solutions by low-frequency raman scattering," *The Journal of Chemical Physics*, vol. 101, no. 5, pp. 3453–3458, 1994.
- [239] K. Mizoguchi, T. Ujike, and Y. Tominaga, "Dynamical structure of water in NaCl aqueous solution," *The Journal of Chemical Physics*, vol. 109, no. 5, pp. 1867–1872, 1998.
- [240] Y. Amo and Y. Tominaga, "Dynamical structure of water in aqueous solutions of LiCl, NaCl, and KCl by low-frequency raman scattering: Comparison between the multiple random telegraph model and cole-cole relaxation," *Physical Review E*, vol. 58, no. 6, pp. 7553–7560, 1998.
- [241] T. Ujike, Y. Tominaga, and K. Mizoguchi, "Dynamical structure of water in alkali halide aqueous solutions," *The Journal of Chemical Physics*, vol. 110, no. 3, pp. 1558–1568, 1999.
- [242] P. Foggi, M. Bellini, D. P. Kien, I. Verduque, and R. Righini, "Relaxation dynamics of water and HCl aqueous solutions measured by time-resolved optical Kerr effect," *The Journal of Physical Chemistry A*, vol. 101, no. 38, pp. 7029–7035, 1997.
- [243] K. J. Tielrooij, S. T. van der Post, J. Hunger, M. Bonn, and H. J. Bakker, "Anisotropic water reorientation around ions," *Journal of Physical Chemistry B*, vol. 115, no. 43, pp. 12638–12647, 2011.
- [244] K. J. Tielrooij, N. Garcia-Araez, M. Bonn, and H. J. Bakker, "Cooperativity in ion hydration," *Science*, vol. 328, no. 5981, pp. 1006–1009, 2010.
- [245] J. T. O'Brien and E. R. Williams, "Effects of ions on hydrogen-bonding water networks in large aqueous nanodrops," *Journal of the American Chemical Society*, vol. 134, no. 24, pp. 10228–10236, 2012.

- [246] B. Winter, “Liquid microjet for photoelectron spectroscopy,” *Nuclear Instruments and Methods in Physics Research Section A: Accelerators, Spectrometers, Detectors and Associated Equipment*, vol. 601, no. 1-2, pp. 139–150, 2009.
- [247] B. Winter, E. F. Aziz, U. Hergenhahn, M. Faubel, and I. V. Hertel, “Hydrogen bonds in liquid water studied by photoelectron spectroscopy,” *Journal of Chemical Physics*, vol. 126, no. 12, p. 124504, 2007.
- [248] G. Öhrwall, R. F. Fink, M. Tchapyguine, L. Ojamäe, M. Lundwall, R. R. Marinho, A. Naves de Brito, S. L. Sorensen, M. Gisselbrecht, R. Feifel, T. Rander, A. Lindblad, J. Schulz, L. J. Sæthre, N. Mårtensson, S. Svensson, and O. Björneholm, “The electronic structure of free water clusters probed by Auger electron spectroscopy,” *Journal of Chemical Physics*, vol. 123, no. 5, p. 054310, 2005.
- [249] P. Slaviček, B. Winter, L. S. Cederbaum, and N. V. Kryzhevoi, “Proton-transfer mediated enhancement of nonlocal electronic relaxation processes in x-ray irradiated liquid water,” *Journal of the American Chemical Society*, vol. 136, no. 52, pp. 18170–18176, 2014.
- [250] G. Zundel and H. Metzger, “Energiebänder der tunnelnden Überschuß-Protonen in flüssigen Säuren. Eine IR-spektroskopische Untersuchung der Natur der Gruppierungen  $\text{H}_5\text{O}_2^+$ ,” *Zeitschrift für Physikalische Chemie*, vol. 58, no. 5–6, pp. 225–245, 1968.
- [251] M. Odelius, H. Ogasawara, D. Nordlund, O. Fuchs, L. Weinhardt, F. Maier, E. Umbach, C. Heske, Y. Zubavichus, M. Grunze, J. D. Denlinger, L. G. Pettersson, and A. Nilsson, “Ultrafast core-hole-induced dynamics in water probed by x-ray emission spectroscopy,” *Physical Review Letters*, vol. 94, no. 22, p. 227401, 2005.
- [252] M. Odelius, “Molecular dynamics simulations of fine structure in oxygen K-edge x-ray emission spectra of liquid water and ice,” *Physical Review B*, vol. 79, no. 14, 2009.

- [253] O. Fuchs, M. Zharnikov, L. Weinhardt, M. Blum, M. Weigand, Y. Zubavichus, M. Bar, F. Maier, J. D. Denlinger, C. Heske, M. Grunze, and E. Umbach, “Isotope and temperature effects in liquid water probed by x-ray absorption and resonant x-ray emission spectroscopy,” *Physical Review Letters*, vol. 100, no. 2, p. 027801, 2008.
- [254] P. Morin and I. I. Nenner, “Atomic autoionization following very fast dissociation of core-excited HBr,” *Physical Review Letters*, vol. 56, no. 18, pp. 1913–1916, 1986.
- [255] E. Pahl, L. S. Cederbaum, H. D. Meyer, and F. Tarantelli, “Controlled interplay between decay and fragmentation in resonant Auger processes,” *Physical Review Letters*, vol. 80, no. 9, pp. 1865–1868, 1998.
- [256] N. V. Kryzhevoi and L. S. Cederbaum, “Exploring protonation and deprotonation effects with Auger electron spectroscopy,” *The Journal of Physical Chemistry Letters*, vol. 3, no. 18, pp. 2733–2737, 2012.
- [257] Z. Wang, A. Pakoulev, Y. Pang, and D. D. Dlott, “Vibrational substructure in the OH stretching transition of water and HOD,” *The Journal of Physical Chemistry A*, vol. 108, no. 42, pp. 9054–9063, 2004.
- [258] I. Unger, S. Thürmer, D. Hollas, E. F. Aziz, B. Winter, and P. Slavíček, “Ultrafast proton and electron dynamics in core-ionized hydrated hydrogen peroxide: Photoemission measurements with isotopically substituted hydrogen peroxide,” *The Journal of Physical Chemistry C*, vol. 118, no. 50, pp. 29142–29150, 2014.
- [259] I. Unger, D. Hollas, R. Seidel, S. Thurmer, E. F. Aziz, P. Slavíček, and B. Winter, “Control of x-ray induced electron and nuclear dynamics in ammonia and glycine aqueous solution via hydrogen bonding,” *Journal of Physical Chemistry B*, vol. 119, no. 33, pp. 10750–10759, 2015.
- [260] A. Lindblad, H. Bergersen, W. Pokapanich, M. Tchapyguine, G. Öhrwall, and O. Björneholm, “Charge delocalization dynamics of ammonia in different



- hydrogen bonding environments: Free clusters and in liquid water solution,” *Physical Chemistry Chemical Physics*, vol. 11, no. 11, pp. 1758–1764, 2009.
- [261] P. Slavíček, N. V. Kryzhevoi, E. F. Aziz, and B. Winter, “Relaxation processes in aqueous systems upon x-ray ionization: Entanglement of electronic and nuclear dynamics,” *The Journal of Physical Chemistry Letters*, vol. 7, no. 2, pp. 234–243, 2016.
- [262] J. Hutter, M. Iannuzzi, F. Schiffmann, and J. VandeVondele, “CP2K: Atomistic simulations of condensed matter systems,” *Wiley Interdisciplinary Reviews: Computational Molecular Science*, vol. 4, no. 1, pp. 15–25, 2014.
- [263] J. VandeVondele, M. Krack, F. Mohamed, M. Parrinello, T. Chassaing, and J. Hutter, “Quickstep: Fast and accurate density functional calculations using a mixed Gaussian and plane waves approach,” *Computer Physics Communications*, vol. 167, no. 2, pp. 103–128, 2005.
- [264] G. Lippert, J. Hutter, x000Fc, rg, and M. Parrinello, “The Gaussian and augmented-plane-wave density functional method for ab initio molecular dynamics simulations,” *Theoretical Chemistry Accounts: Theory, Computation, and Modeling (Theoretica Chimica Acta)*, vol. 103, no. 2, pp. 124–140, 1999.
- [265] D. Hollas, M. N. Pohl, R. Seidel, E. F. Aziz, P. Slavíček, and B. Winter, “Aqueous solution chemistry of ammonium cation in the Auger time window,” *Scientific Reports*, vol. 7, no. 1, p. 756, 2017.
- [266] T. Steiner, “The hydrogen bond in the solid state,” *Angewandte Chemie International Edition*, vol. 41, no. 1, pp. 48–76, 2002.
- [267] I. S. Ufimtsev and T. J. Martinez, “Quantum chemistry on graphical processing units. 3. analytical energy gradients, geometry optimization, and first principles molecular dynamics,” *Journal of Chemical Theory and Computation*, vol. 5, no. 10, pp. 2619–2628, 2009.

- [268] A. V. Titov, I. S. Ufimtsev, N. Luehr, and T. J. Martinez, "Generating efficient quantum chemistry codes for novel architectures," *Journal of Chemical Theory and Computation*, vol. 9, no. 1, pp. 213–221, 2013.
- [269] A. I. Krylov and P. M. W. Gill, "Q-chem: An engine for innovation," *Wiley Interdisciplinary Reviews: Computational Molecular Science*, vol. 3, no. 3, pp. 317–326, 2013.
- [270] D. Hollas, *ABIN: Multipurpose ab initio MD program*.  
<https://github.com/PHOTOX/ABIN>, 2018, Online accessed: November 22, 2018.
- [271] H.-J. Werner, P. J. Knowles, G. Knizia, F. R. Manby, and M. Schütz, "MolPro: A general-purpose quantum chemistry program package," *Wiley Interdisciplinary Reviews: Computational Molecular Science*, vol. 2, no. 2, pp. 242–253, 2012.
- [272] A. T. Gilbert, N. A. Besley, and P. M. Gill, "Self-consistent field calculations of excited states using the maximum overlap method (MOM)," *Journal of Physical Chemistry A*, vol. 112, no. 50, pp. 13164–13171, 2008.
- [273] N. A. Besley, A. T. Gilbert, and P. M. Gill, "Self-consistent-field calculations of core excited states," *Journal of Chemical Physics*, vol. 130, no. 12, p. 124308, 2009.
- [274] P. C. do Couto, D. Hollas, and P. Slaviček, "On the performance of optimally tuned range-separated hybrid functionals for x-ray absorption modeling," *Journal of Chemical Theory and Computation*, vol. 11, no. 7, pp. 3234–3244, 2015.
- [275] A. W. Lange and J. M. Herbert, "A smooth, nonsingular, and faithful discretization scheme for polarizable continuum models: The switching/Gaussian approach," *Journal of Chemical Physics*, vol. 133, no. 24, p. 244111, 2010.
- [276] J. Heyda, M. Lund, M. Oncak, P. Slaviček, and P. Jungwirth, "Reversal of hofmeister ordering for pairing of  $\text{NH}_4^+$  vs alkylated ammonium cations with

- halide anions in water,” *Journal of Physical Chemistry B*, vol. 114, no. 33, pp. 10843–10852, 2010.
- [277] M. Mucke, T. Arion, M. Förstel, T. Lischke, and U. Hergenbahn, “Competition of inelastic electron scattering and interatomic Coulombic decay in Ne clusters,” *Journal of Electron Spectroscopy and Related Phenomena*, vol. 200, pp. 232–238, 2015.
- [278] W. Pokapanich, H. Bergersen, I. L. Bradeanu, R. R. Marinho, A. Lindblad, S. Legendre, A. Rosso, S. Svensson, O. Björneholm, M. Tchapyguine, G. Öhrwall, N. V. Kryzhevoi, and L. S. Cederbaum, “Auger electron spectroscopy as a probe of the solution of aqueous ions,” *Journal of the American Chemical Society*, vol. 131, no. 21, pp. 7264–7271, 2009.
- [279] Y. Velkov, T. Miteva, N. Sisourat, and J. Schirmer, “Intermediate state representation approach to physical properties of dicationic states,” *Journal of Chemical Physics*, vol. 135, no. 15, p. 154113, 2011.
- [280] M. Mucke, M. Braune, S. Barth, M. Förstel, T. Lischke, V. Ulrich, T. Arion, U. Becker, A. Bradshaw, and U. Hergenbahn, “A hitherto unrecognized source of low-energy electrons in water,” *Nature Physics*, vol. 6, no. 2, pp. 143–146, 2010.
- [281] A. A. Chialvo and L. Vlcek, “Toward the understanding of hydration phenomena in aqueous electrolytes from the interplay of theory, molecular simulation, and experiment,” *Fluid Phase Equilibria*, vol. 407, pp. 84–104, 2016.
- [282] L. Petit, R. Vuilleumier, P. Maldivi, and C. Adamo, “Ab initio molecular dynamics study of a highly concentrated LiCl aqueous solution,” *Journal of Chemical Theory and Computation*, vol. 4, no. 7, pp. 1040–1048, 2008.
- [283] I. Harsanyi and L. Pusztai, “Hydration structure in concentrated aqueous lithium chloride solutions: A reverse monte carlo based combination of molecular dynamics simulations and diffraction data,” *Journal of Chemical Physics*, vol. 137, no. 20, p. 204503, 2012.

- [284] E. Pluharova, P. E. Mason, and P. Jungwirth, "Ion pairing in aqueous lithium salt solutions with monovalent and divalent counter-anions," *Journal of Physical Chemistry A*, vol. 117, no. 46, pp. 11766–11773, 2013.
- [285] J.-J. Xu, H.-B. Yi, H.-J. Li, and Y. Chen, "Ionic solvation and association in LiCl aqueous solution: a density functional theory, polarised continuum model and molecular dynamics investigation," *Molecular Physics*, vol. 112, no. 12, pp. 1710–1723, 2013.
- [286] E. Pluhařová, H. E. Fischer, P. E. Mason, and P. Jungwirth, "Hydration of the chloride ion in concentrated aqueous solutions using neutron scattering and molecular dynamics," *Molecular Physics*, vol. 112, no. 9-10, pp. 1230–1240, 2014.
- [287] W. Wachter, S. Fernandez, R. Buchner, and G. Hefter, "Ion association and hydration in aqueous solutions of LiCl and Li<sub>2</sub>SO<sub>4</sub> by dielectric spectroscopy," *Journal of Physical Chemistry B*, vol. 111, no. 30, pp. 9010–9017, 2007.
- [288] Y. Marcus and G. Hefter, "Ion pairing," *Chemical Reviews*, vol. 106, no. 11, pp. 4585–4621, 2006.
- [289] E. Fasshauer, M. Förstel, M. Mucke, T. Arion, and U. Hergenhan, "Theoretical and experimental investigation of electron transfer mediated decay in ArKr clusters," *Chemical Physics*, vol. 482, pp. 226–238, 2017.
- [290] L. Sun, X. Li, Y. Tu, and H. Agren, "Origin of ion selectivity at the air/water interface," *Physical Chemistry Chemical Physics*, vol. 17, no. 6, pp. 4311–4318, 2015.
- [291] F. Bresme, E. Chacon, P. Tarazona, and A. Wynveen, "The structure of ionic aqueous solutions at interfaces: An intrinsic structure analysis," *Journal of Chemical Physics*, vol. 137, no. 11, p. 114706, 2012.
- [292] K. A. Perrine, K. M. Parry, A. C. Stern, M. H. C. Van Spyk, M. J. Makowski, J. A. Freites, B. Winter, D. J. Tobias, and J. C. Hemminger, "Specific cation effects at

- aqueous solution-vapor interfaces: Surfactant-like behavior of  $\text{Li}^+$  revealed by experiments and simulations,” *Proceedings of the National Academy of Sciences of the United States of America*, vol. 114, no. 51, pp. 13363–13368, 2017.
- [293] J. J. Yeh and I. Lindau, “Atomic subshell photoionization cross sections and asymmetry parameters:  $1 \leq z \leq 103$ ,” *Atomic Data and Nuclear Data Tables*, vol. 32, no. 1, pp. 1–155, 1985.
- [294] B. Minofar, R. Vacha, A. Wahab, S. Mahiuddin, W. Kunz, and P. Jungwirth, “Propensity for the air/water interface and ion pairing in magnesium acetate vs magnesium nitrate solutions: Molecular dynamics simulations and surface tension measurements,” *Journal of Physical Chemistry B*, vol. 110, no. 32, pp. 15939–15944, 2006.
- [295] G. Öhrwall, N. Ottosson, W. Pokapanich, S. Legendre, S. Svensson, and O. Björneholm, “Charge dependence of solvent-mediated intermolecular Coster-Kronig decay dynamics of aqueous ions,” *Journal of Physical Chemistry B*, vol. 114, no. 51, pp. 17057–17061, 2010.
- [296] B. Jiang, V. Ponnuchamy, Y. Shen, X. Yang, K. Yuan, V. Vetere, S. Mossa, I. Skarmoutsos, Y. Zhang, and J. Zheng, “The anion effect on  $\text{Li}^+$  ion coordination structure in ethylene carbonate solutions,” *The Journal of Physical Chemistry Letters*, vol. 7, no. 18, pp. 3554–3559, 2016.
- [297] C. Nordling, E. Sokolowski, and K. Siegbahn, “Precision method for obtaining absolute values of atomic binding energies,” *Physical Review*, vol. 105, no. 5, pp. 1676–1677, 1957.
- [298] U. Gelius and K. Siegbahn, “ESCA studies of molecular core and valence levels in the gas phase,” *Faraday Discussions of the Chemical Society*, vol. 54, 1972.
- [299] G. Olivieri, A. Goel, A. Kleibert, D. Cvetko, and M. A. Brown, “Quantitative ionization energies and work functions of aqueous solutions,” *Physical Chemistry Chemical Physics*, vol. 18, no. 42, pp. 29506–29515, 2016.



# List of Publications

## PUBLICATIONS COVERED IN THIS THESIS:

- I**            **Observation of Electron-Transfer Mediated Decay in Aqueous Solution.**  
I. Unger, R. Seidel, S. Thürmer, M. N. Pohl, E. F. Aziz, L. S. Cederbaum,  
E. Muchová, P. Slavíček, B. Winter, and N. V. Kryzhevoi  
*Nature Chemistry* **9**, 708–714 (2017)
- II**            **Aqueous Solution Chemistry of Ammonium Cation in the Auger Time Window.**  
D. Hollas, M. N. Pohl, R. Seidel, E. F. Aziz, P. Slavíček, and B. Winter  
*Scientific Reports* **7**, 756 (2017)
- III**           **Sensitivity of Electron-Transfer Mediated Decay to Ion Pairing.**  
M. N. Pohl, C. Richter, E. Lugovoy, R. Seidel, P. Slavíček, E. F. Aziz,  
B. Abel, B. Winter, and U. Hergenbahn  
*The Journal Physical Chemistry B* **121**(32), 7709–7714 (2017)
- IV**           **Advances in Liquid Phase Soft-X-ray Photoemission Spectroscopy: A New Experimental Setup at BESSY II.**  
R. Seidel, M. N. Pohl, H. Ali, B. Winter, and E. F. Aziz  
*Review of Scientific Instruments* **88**, 073107 (2017)
- V**            **Do water's electrons care of electrolytes?**  
M. N. Pohl, E. Muchová, R. Seidel, H. Ali, Š. Sršeň, I. Wilkinson, B. Winter,  
and P. Slavíček  
Submitted to *Chemical Science* (2018)

PUBLICATIONS NOT COVERED IN THIS THESIS:

- VI**                    **Optical Fluorescence Detected from X-ray Irradiated Liquid Water.**  
A. Hans, C. Ozga, R. Seidel, P. Schmidt, T. Ueltzhöffer, X. Holzapfel,  
P. Wenzel, P. Reiß, M. N. Pohl, I. Unger, E. F. Aziz, A. Ehresmann, P. Slavíček,  
B. Winter, and A. Knie  
*The Journal Physical Chemistry B*, 121 (10), 2326–2330 (2017)
- VII**                    **Detection of the Electronic Structure of Iron-(III)-Oxo Oligomers  
Forming in Aqueous Solutions.**  
R. Seidel, K. Kraffert, A. Kabelitz, M. N. Pohl, R. Krähnert, F. Emmerling,  
and B. Winter  
*Physical Chemistry Chemical Physics* **19**, 32226–32234 (2017)
- VIII**                    **Molecular Species Forming at the  $\alpha$ -Fe<sub>2</sub>O<sub>3</sub> Nanoparticle – Aqueous  
Solution Interface.**  
H. Ali, R. Seidel, M. N. Pohl, and B. Winter  
*Chemical Science* **9**, 4511-4523 (2018)



# Acknowledgments

First of all I would like to thank my supervisor GERARD MEIJER. Thanks to his confidence in me I could pursue my projects with a large degree of independence. This gave me the great opportunity to work in two different impressive research facilities, the Fritz-Haber-Institut of the Max Planck Society and at the synchrotron facility BESSY II of the Helmholtz-Zentrum Berlin.

I am extraordinarily grateful to BERND WINTER, the expert of liquid-jet photoelectron spectroscopy, who was mentoring me the last three years. I got to know Bernd as both a cheerful person and a great scientist. His way of approaching science sparked my research interests every single day. His remarkable trait of challenging the prevailing opinion – even his own – taught me lessons of inestimable value for my future career. I always enjoyed working in his group and I deeply hope that we may work together again in the future.

I have been very fortunate to work with UWE HERGENHAHN. I always had the feeling that Uwe treated me not only as collaborator but as a part of his own group. He was always accessible for me, be it for scientific discussion, providing me office space and lab equipment or for a simple chat. His vast knowledge about PE spectroscopy was a rich treasure for all the questions I had throughout the past three years.

I will also never forget the long and exhausting nights working at the beamline together with ROBERT SEIDEL. His ability to stay focused and concentrated even after hours of hard work impressed me and built the basis for achieving excellent results. Robert has my special thanks for helping me throughout my whole PhD time. I always appreciated his funny and helpful personality not only at work, but also in my private live. I hope we will stay in close contact and work together to enhance on our ‘last-hit’ skills.

IAIN WILKINSON has my special acknowledgement as he provided me always with valuable advice and I am still impressed of his ability to stay patient against a backdrop of high workload. I particularly appreciate his critical way of thinking, which pointed me more than once on flaws I could not see by my own.

During the course of my PhD I met many people who made big contributions, be it with discussions, experiments, writing or simply being good company. I want to mention in particular PETR SLAVÍČEK, CLEMENS RICHTER, HEBATALLAH ALI, ARNO BERGMANN, DANIEL HOLLAS, ISAAK UNGER, ANNE STEPHANSEN, SEBASTIAN MALERZ and CLAUDIA KOLBECK. I wish each of them all the best for their future.

I cannot express how much I appreciate my family for giving me love and unwavering support from the first day of my life until now. You made it possible for me to become what I am now. I want to dedicate the last sentence to my beloved little daughter CHARLOTTE whom I send warm hugs and HEIDI for giving me the motivation and continuous support to overcome the past stressful months.



# Curriculum Vitae

For reasons of data protection,  
the curriculum vitae is not published  
in the electronic version.



# Selbstständigkeitserklärung

Hiermit versichere ich, Marvin Nicolas Pohl, geboren am [REDACTED] in [REDACTED], gemäß § 7 Absatz 4 der Promotionsordnung der Freien Universität Berlin, die vorliegende Dissertation am Fritz-Haber-Institut der Max-Planck-Gesellschaft unter der Betreuung von Prof. Gerard J. M. Meijer selbständig und nur unter Verwendung zulässiger Hilfsmittel angefertigt zu haben. Die Stellen der Arbeit, die anderen Werken entnommen sind, wurden in jedem einzelnen Fall als Zitat kenntlich gemacht. Diese Arbeit hat in gleicher oder ähnlicher Form noch keiner anderen Prüfungsbehörde vorgelegen.

Berlin, den 24.08.2018

\_\_\_\_\_